

**Self-Assembly of Nanoparticles in Dispersion
and at Fluid-Fluid Interfaces**

Kjersta L. Larson-Smith

A dissertation
submitted in partial fulfillment of the
requirements for the degree of

Doctor of Philosophy

University of Washington

2012

Reading Committee:

Danilo C. Pozzo, Chair

John C. Berg

Jill E. Seebergh

Program Authorized to Offer Degree:

Department of Chemical Engineering

University of Washington

Abstract

Self-Assembly of Nanoparticles in Dispersion and at Fluid-Fluid Interfaces

Kjersta L. Larson-Smith

Chair of the Supervisory Committee:
Assistant Professor Danilo C. Pozzo
Department of Chemical Engineering

Self-assembly is a fundamental mechanism by which structures form in materials. This mechanism has given rise to many new technological advances in applications as diverse as structural composites, medicine, alternative energy sources and information technology. Many current approaches to self-assembly have shown promise, but each has its own unique limitations. The over-arching goal of this study is to develop self-assembly processes for nanoparticles that are simple, scalable and cost effective. In this dissertation we examine the mechanism for self assembly of nanoparticles in dispersion and at fluid-fluid interfaces.

A simple method is presented for the synthesis of amphiphilic gold nanoparticle surfactants that self-assemble into clusters of controllable structure. The technique is based on the control of particle clustering through sequential functionalization of the surface with thiol terminated polyethylene glycol to sterically stabilize particles in water and short alkane-thiols that render the particles amphiphilic. These nanoparticle surfactants are surface active and form rafts at the air-water interface and stable nanoparticle clusters in dispersion. The clusters are also reminiscent of traditional micelles with an adjustable aggregation number that is controlled via modification of the grafting density of polymer on the nanoparticle surface. The nanoparticle surfactants are also shown to be highly effective emulsifying agents due to their amphiphilicity and they adsorb strongly to oil-water interfaces with controllable inter-particle separation distances. Both the clusters and colloidosomes that can be formed with these particles exhibit tunable shifts in plasmon resonance, enhancing the near-infrared optical absorption and making them useful for a wide range of applications.

TABLE OF CONTENTS

List of Figures	iii
Chapter 1: Introduction to Nanoparticle Self-Assembly	1
1.1 Background	1
1.2 Nanoparticle Synthesis	3
1.3 Nanoparticle Self-Assembly	5
1.4 Objectives and Approach	8
Chapter 2: Small Angle Scattering	12
2.1 Introduction to Technique	12
2.1.1 Contrast Matching	15
2.1.2 Basic Data Analysis Methods	18
2.2 Debye Model	23
2.3 Pickering Model	27
2.3.1 Application of Method	33
2.4 Summary	39
Chapter 3: Scalable Synthesis of Self-Assembling Nanoparticle Clusters Base on Controlled Steric Interactions	40
3.1 Background	40
3.2 Experimental Methods	43
3.3 Results and Discussion	46
3.3.1 Cluster Formation and Characterization	46
3.3.2 Mechanism and Sensitivity to Environment	61
3.3.3 Expansion of Method to Other Systems	65
3.4 Summary	67
Chapter 4: Competitive Adsorption of Thiolated Polyethylene Glycol and Alkane-thiols on Gold Nanoparticles	69
4.1 Background	69
4.2 Experimental Methods	73
4.3 Results	75
4.3.1 Thiol Surface Adsorption	75
4.3.2 PEG Conformation	79
4.3.3 Effects of PEG Concentration and Conformation on Cluster Formation	82
4.4 Discussion	87
4.5 Summary	91
Chapter 5: Charged Nanoparticle Adsorption at Oil-Water Interfaces	92
5.1 Background	92
5.2 Experimental Methods	97
5.3 Surface Charge	100
5.3.1 Surface Charge on oil droplets	100

5.3.2 Surface Charge on PS Latex	101
5.3.3 Surface Charge on Gold Nanoparticles	102
5.4 DLVO theory and calculations.....	103
5.5 Measurement of Particle Adsorption at Oil-Water Interfaces.....	108
5.5.1 Adsorption of PS Latex.....	108
5.5.2 Adsorption of Gold Nanoparticles.....	112
5.6 Discussion	114
5.7 Summary	116
Chapter 6: Pickering Emulsions Stabilized by Nanoparticle Surfactants.....	117
6.1 Background	117
6.2 Experimental Methods	122
6.3 Results and Discussion.....	124
6.3.1 Hexadecane Emulsions	124
6.3.2 Low Boiling Point Oil Emulsions.....	136
6.4 Summary	142
Chapter 7: Conclusions and Outlook	144
7.1 Key Results	144
7.2 Future Outlook	148
Bibliography	152
Appendix A: Particle Synthesis and Functionalization	163
Appendix B: Photoacoustic and Ultrasound Imaging Experimental Set-Up.....	169

List of Figures

Figure	Page
1.1 TEM Images of Monodisperse Nanoparticles	4
1.2 Schematic of Self-Assembling Systems	6
1.3 TEM Images of Gold Nanoparticle Clusters	9
1.4 SEM Image of Composite Gold Nanoshell	11
2.1 Experimental Set-Up for Small Angle Scattering.....	15
2.2 Schematic of Contrast Matching Technique.....	18
2.3 Experimental Determination of Contrast Match Point	20
2.4 Guinier Analysis	21
2.5 SANS PS Latex Form Factor.....	23
2.6 SANS PS Latex Structure Factor.....	24
2.7 Schematic and Debye Model Equations for Cluster Geometries.....	27
2.8 Debye Model Scattering Profiles	28
2.9 Debye Model Scattering of Pickering Emulsion	29
2.10 Schematic of a Pickering Emulsion Oil-Particle Complex.....	30
2.11 Comparison of Raspberry and Core-Shell Scattering Models.....	36
2.12 Comparison of Raspberry and Sphere Scattering Models	37
2.13 Raspberry Model with Different Scattering Contrasts.....	38
2.14 Raspberry Model with Different Particle Penetration Depths	39
3.1 Schematic of Cluster Formation	45
3.2 UV-Vis Data of Gold Clusters.....	49
3.3 UV-Vis Spectra of Gold Cluster Formation Over Time.....	50
3.4 DLS of Functionalized Particles.....	52

3.5 DLS of Clusters as a Function of PEG Concentration.....	53
3.6 TEM Images and Histograms of Gold Nanoparticle Clusters	55
3.7 SAXS Data for Gold Nanoparticle Clusters	57
3.8 Debye Model Scattering for Gold Nanoparticle Clusters.....	58
3.9 SAXS Data and Debye Model Comparison.....	59
3.10 Debye Model Sensitivity to Cluster Distributions	60
3.11 SAXS and DLS Data Comparison.....	61
3.12 SAXS Data for Clusters at Different Temperatures	63
3.13 SAXS Data for Clusters in Different Salt Concentrations.....	64
3.14 SAXS Data Before and After Dialysis.....	65
3.15 Silver Nanoparticle Clusters Data.....	67
3.16 TEM Images of Gold Composite Particle Cluster	68
4.1 Schematic Comparison of Cluster and Micelle Structures	74
4.2 TGA Profile of PEG and Tetradecane Functionalized Gold	78
4.3 Surface Concentrations of PEG-thiol and Alkane-thiol on Gold.....	79
4.4 Zeta Potential of Nanoparticle Surfactants	80
4.5 DLS Data for Nanoparticle Surfactants	82
4.6 Comparison of Hydrodynamic Size and Surface Concentration	83
4.7 Schematic of PEG Conformation.....	84
4.8 SAXS Data for Nanoparticle Surfactants with Different Alkane-thiols.....	86
4.9 Radius of Gyration of Nanoparticle Clusters.....	87
4.10 TEM Images of Clusters with Different Alkane-thiols.....	88
5.1 Schematic of Emulsification Methods	96
5.2 Zeta Potential of Hexadecane Emulsion Droplets	102
5.3 Zeta Potential of PS Latex	103

5.4 DLVO Curve for Hexadecane and PS Latex with Increasing Ionic Strength.....	106
5.5 DLVO Curve for Hexadecane and PS Latex at Different pH.....	107
5.6 DLVO Curve for Two PS Latex Particles	108
5.7 DLVO Curve for Hexadecane and Cationic Gold Nanoparticles.....	109
5.8 SANS and USANS Data for PS Latex and Hexadecane Pickering Emulsion.....	110
5.9 SANS Data for PS Latex and Hexadecane Emulsions	111
5.10 Particle Surface Coverage of Hexadecane Emulsion Droplets.....	113
5.11 SAXS Data for Cationic Gold Nanoparticles and Hexadecane Emulsions	115
6.1 Schematic of Composite Emulsion Nanoshell NIR-induced Vaporization.....	122
6.2 Schematic of Composite Emulsion Nanoshell Formation	125
6.3 Micrographs of Nanoparticle Surfactant Clusters and Nanoshells.....	129
6.4 UV-Vis Data of Nanoparticle Surfactant Clusters and Nanoshells	131
6.5 SAXS Data of Nanoparticle Surfactant Clusters and Nanoshells	134
6.6 UV-Vis Data of Nanoshells with Varying Nanoparticle Surfactant Type.....	136
6.7 SAXS Data of Nanoshells with Varying Nanoparticle Surfactant Type	138
6.8 UV-Vis and SAXS Data of Perfluorohexane Emulsions.....	142
6.9 Optical Micrographs of Perfluorohexane Emulsions	143
6.10 Photoacoustic and Ultrasound Signal	144
6.11 Integrated Photoacoustic and Ultrasound Data	145

Acknowledgements

I would like to thank my advisor, Danilo Pozzo, for the constant mentoring, guidance and patience. His enthusiasm and drive for excellence are infectious and have ultimately made me a better scientist. I also would like to thank members of my committee, John Berg, Jill Seebergh, Rene Overney and Guozhong Cao for providing me with invaluable advice on my research directions.

I thank all of my fellow students, especially Katie Weigandt, Monica Ospinal-Jimenez, Greg Newbloom, Jeff Richards and Pablo de la Iglesia for the countless technical conversations and brainstorming sessions. They also provided much needed comic relief on many occasions (especially at NIST), to help me retain my sanity.

Andrew Jackson was a major collaborator in the Pickering emulsion work, particularly in the development and interpretation of the small angle scattering model. I also acknowledge Tom Matula and Chen-Wei Wei for recent collaborations in evaluating the plasmonic emulsions as theranostic agents. Many undergraduate students also contributed to this research. I especially want to acknowledge Heather Milligan who worked on the self-assembling silver nanoparticles and John Willey who synthesized the raspberry composite particles.

Finally, I thank my friends and family for the constant love and support. I especially acknowledge my parents for instilling in me from a young age a genuine sense of curiosity, the immeasurable value of an education and that there is no substitute for gritting your teeth and rolling up your sleeves. I also thank my husband, Dustin, for providing me with ice cream to fuel my brain, listening to me ramble on about “nanos” and making me laugh when I needed a distraction.

Dedication

To my husband, Dustin, for selflessly supporting me to make my dream a reality.

Chapter 1. Introduction

Nanotechnology has gained extensive interest over the last several decades, both from the scientific community and from the general public. Exciting technological innovations utilizing nanotechnology will have tremendous impact on areas as diverse as structural materials, medicine, alternative energy sources and information technology.¹⁻⁵ One benefit to shrinking the size of devices and structures is the potential for increased information storage capacity and device speed in microelectronics. More importantly, nanotechnology can give rise to new material functionality because ‘nanostructures’, particles or composites structures that have at least one dimension on the nanoscale, have fundamentally different physical properties that are governed by quantum confinement effects. The quantum behavior of nanometer sized features can be exploited to engineer electronic, magnetic and optical properties.

1.1 Background

The emergence of nanotechnology has given rise to the development of many cutting edge technologies such as colloidosomes for drug-delivery, composites that are strong yet lightweight and increasingly smaller consumer electronics and computational devices. Each of these examples utilizes materials that are on the nanoscale in at least one dimension. Colloidosomes are porous microcapsules that are constructed from a composite shell of particles.^{1,2} These structures can be used to encapsulate proteins or pharmaceuticals for applications in controlled drug-delivery. Nanoparticles are used as the building blocks for these structures because they allow for the most control over the permeability of the colloidosome, making the structures useful for controlled delivery of

small molecule drugs.⁶ In another application, the strength of nanoscale materials is exploited to create lightweight composites. These bulk materials are known as ‘nanomaterials’ because they have morphological features on the nanoscale. Carbon nanotubes, for example, exhibit extraordinary tensile strength and elastic moduli, and are efficient thermal and electrical conductors.³ Recently, carbon nanotubes have been incorporated into polymer matrices to achieve composites with both high strength and electrical conductivity. Composites are used in a variety of applications such as lightweight boat hulls and sporting equipment. Finally, there has also been an increasing focus on using inorganic colloidal nanoparticles for light-emitting displays and solar cells because the optical and electrical properties of these materials are tunable and directly related to the size, shape and arrangement of the particles.⁴ Self-assembly of these nanoparticles into three-dimensional superlattices or nano-clustered colloidal molecules is an especially effective strategy for creating novel, tunable opto-electronic materials.⁷ These few examples show the varied and impactful applications that are possible with nanoscale materials.

These applications are possible because bulk materials exhibit profoundly different properties than nanoscale materials. The properties of these materials are different at the nanoscale because of the increased surface to volume ratio.⁸ The percentage of atoms at the surface of a material becomes significant and the properties of the surface atoms begin to dominate over the bulk properties of the material. Size dependent properties include quantum behavior in semi-conducting particles, surface plasmon resonance in metallic particles and superparamagnetism in magnetic particles.⁹

¹⁰ For example, surface plasmon resonance in metallic colloidal nanoparticles leads to

size-dependent, tunable electrical and optical properties. Gold nanoparticles, for instance, exhibit tunable optical absorption that spans the visible spectrum depending on the particle size and shape.¹⁰ Hence, metallic and semiconducting nanoparticles have been targeted as building blocks for materials with specific mechanical, optical and magnetic properties.¹¹ This has led to a world-wide and continually growing interest in their synthesis and processing.^{5, 12}

1.2 Nanoparticle Synthesis

In the early years of nanotechnology, much of the work focused on synthesizing particles of different size, shape and material. The most commonly used colloidal building blocks have spherical symmetry, so in the past several decades many methods have been developed for synthesizing spherical particles. A wealth of monodisperse colloids can now be synthesized from various organic polymers and inorganic materials. Figure 1.1 shows TEM images of particles that are used in this dissertation. Figure 1.1a is a TEM of polystyrene latex particles ($d = 100$ nm) that are purchased from Thermo Scientific (Waltham, MA). These commercially available particles were prepared using emulsion polymerization where monomers are polymerized inside surfactant-stabilized emulsions resulting in extremely monodisperse particles.¹³ The 15 nm silver nanoparticles in Figure 1.1b are synthesized by reducing silver nitrate with sodium citrate and quenching the reaction with ammonia to control particle polydispersity.¹⁴ The Turkevich method was used to synthesize the 12 nm gold nanoparticles in Figure 1.1c.¹⁵ These methods have been carefully refined so that they reliably produce monodisperse particles with a simple procedure.

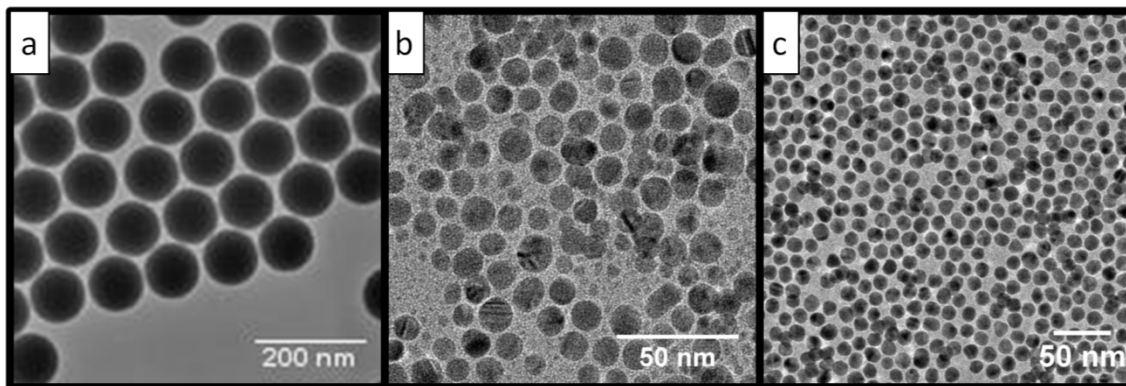


Figure 1.1. TEM images of a) 100nm polystyrene latex particles purchased from Thermo Scientific¹³, b) 15nm silver nanoparticles and c) 12nm gold particles. The gold and silver nanoparticles are synthesized and characterized at the University of Washington.

To further explore the unique properties of nanostructures, many techniques have been developed to synthesize particles of different shapes. New syntheses include the formation of polystyrene spheroids with a tunable aspect ratio that are used to expand the photonic band gap in crystalline colloid lattices.¹⁶ It was also recently demonstrated that silver and gold could be synthesized into uniform nanocubes and nanoboxes in order to gain even further control over the optical and electrical properties of the materials.¹⁷ Moreover, anisometric particles such as iron oxide particles in a peanut shape have been synthesized.^{18, 19} In addition to forming particles with unique shapes, there is also great interest in forming nanorods. Specifically, nanorods with extreme aspect ratios such as carbon nanotubes that have aspect ratios reaching as high as 132,000,000:1 are useful because of their high tensile strength and semiconducting properties.²⁰ Syntheses for carbon nanotubes typically involve chemical vapor deposition or laser ablation and are much more challenging than the solution phase processes typically used for inorganic materials.^{21, 22}

1.3. Nanoparticle self-assembly

Previously, most work in the field of nanotechnology has focused on synthesizing nanoparticles in a variety of sizes, shapes and materials. While this has been instrumental in the progression of nanoscience, it is only the first step to the synthesis of nanostructures and nanomaterials. In order to further expand the field it is necessary to arrange these particles into useful structures, which has been a main focus in recent years.

Methods to construct these new nanostructured materials typically are divided into two categories, “top-down” and “bottom-up”. In traditional “top-down” manufacturing, macroscopic features are scaled down. In contrast, structures made by “bottom-up” manufacturing are built by organizing smaller sub-units. Examples of “top-down” manufacturing processes include mechanical methods, photolithography, and scanning probe methods used to arrange particles.²³⁻²⁵ The benefit to these methods is the high level of control over the final structure. However, manufacturing structures in this manner is not scalable as it is extremely time intensive and there are size limitations based on the resolution of the equipment and manufacturing.²⁶⁻²⁸

The “bottom-up” approach utilizes the self-assembly of nanoscale building blocks for material synthesis. Many materials exhibit self-assembling behavior as a result of interactions mediated by charge, dipoles (van der Waals) and hydrophobicity that result in controllable inter-particle forces.²⁹ Figure 1.2 is a schematic highlighting different engineered and naturally occurring self-assembling systems. Some of the most intricate and efficient self-assembling systems are found in nature. Examples include the folding and coiling of polypeptides in protein structures and the double helix structure of DNA.^{30,}

³¹ While it is difficult to match the complexity of natural systems, synthetic molecules can be engineered to emulate the self-assembling properties found in nature. For example, surfactants in water self-assemble into micelles with hydrophobic tails in the center of the structure and hydrophilic head groups around the perimeter.³² Other examples of self-assembling systems include phase-separated copolymers and self-assembled monolayers on gold substrates.^{33, 34}

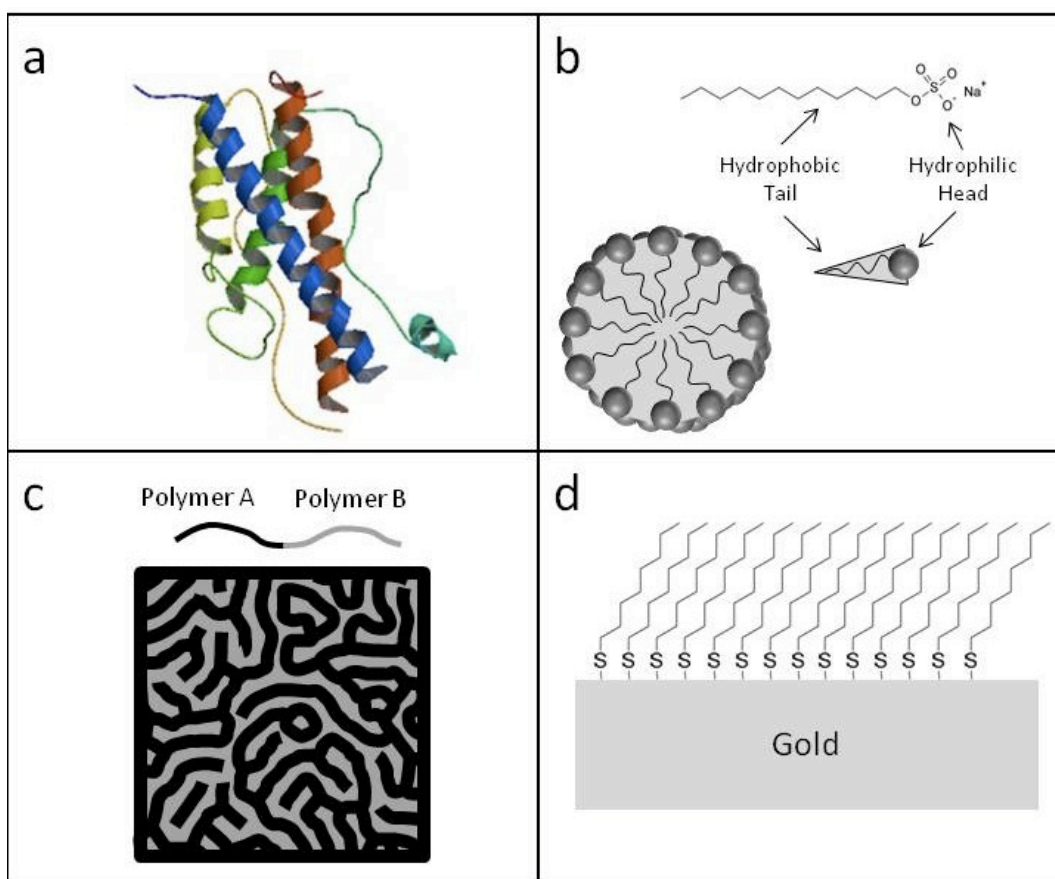


Figure 1.2. Schematic of self-assembling systems: a) human growth hormone,³¹ b) sodium dodecyl sulfate surfactant micelles, c) phase-separated copolymers, d) self-assembled monolayers on gold substrates.

Several approaches are currently used to engineer self-assembled structures from colloidal particles; however, each method has its own unique limitations.³⁵⁻⁴² Methods for

self-assembly in dispersion are often based on the use of patchy particles that can be functionalized using techniques such as glancing-angle deposition, emulsion-based templating or particle lithography.^{27, 43} In one example, Janus particles are shown to self-assemble into a variety of structured colloidal clusters by controlling attractive electrostatic interactions.⁴⁴ Unfortunately, these techniques are often limited by low particle yields or by the inability to functionalize and organize particles at the nanometer scale. Another way to self-assemble particles is with physical templates. Velev and colleagues first used emulsion droplets as templates to organize spherical latex particles of 1 μm diameter into large aggregates using excluded volume interactions.¹ Similarly, Pine et al. assembled polystyrene latexes into polyhedral objects with well-controlled sizes and shapes through the encapsulation of particles in oil droplets and subsequent formation of stable clusters by removal of the organic solvent.³⁵ They demonstrate that energetically stable cluster geometries are obtained and that the specific particle arrangement is directly determined by the original number of particles inside each droplet.³⁵ Dinsmore and coworkers used the oil-water interface of an emulsion to generate hollow spherical aggregates out of 1 μm polystyrene particles.² Bulk phase methods like this one are attractive due to the potential for obtaining large yields with scaleup, but they are often limited to the organization of relatively large particles (> 100 nm). Grafting or growing block copolymers or DNA on surfaces has also been used to assemble nanoparticles and to form stable clusters.⁴⁵⁻⁴⁹ Unfortunately, many of these polymer-based techniques require expensive materials or complex synthetic chemistry steps that can limit widespread use by researchers lacking the necessary expertise or resources. Finally, equilibrium clusters can also form by carefully balancing the attractive

and repulsive colloidal interactions (e.g. ionic or depletion) that occur in proteins and other particle systems.⁵⁰ In these cases the particles are often in a dynamic equilibrium so that clustered structures are not robust and may be strongly affected by temperature and ionic strength.

1.4. Objectives and Approach

While many self-assembly methods are successfully used to form nanostructures, each of the approaches has some limitations. An ideal self-assembly methodology would be a simple and scalable technique that could be used for both microparticles and nanoparticles. The over-arching goal of this study is to develop self-assembly processes for particles on the nano-scale that are simple, scalable and cost effective. In this dissertation we examine the self-assembly of nanoparticles for two different systems, in dispersion and at fluid-fluid interfaces.

In Chapters 3 and 4 we present the synthesis of amphiphilic gold nanoparticles that can spontaneously self-assemble into stable clusters with controllable geometry. The technique is based on the control of colloidal interactions through sequential functionalization of the surfaces with long thiol-terminated poly(ethylene glycol) methyl ether (PEG) chains followed by short alkane-thiol molecules. This process renders the gold nanoparticles amphiphilic and initiates the self-assembly of stable clusters in the dispersion. A schematic of this synthesis procedure is given in Figure 1.3. With this new approach, we show that it is possible to fabricate large numbers of amphiphilic ‘nanoparticle surfactants’ that form clusters with controllable structure. Clustering is controlled by manipulating the steric forces that are imparted by surface-bound polymers

and the attractive interactions of the hydrophobic alkane-thiols. Figure 1.4 shows examples of the resulting clusters as examined with transmission electron microscopy.

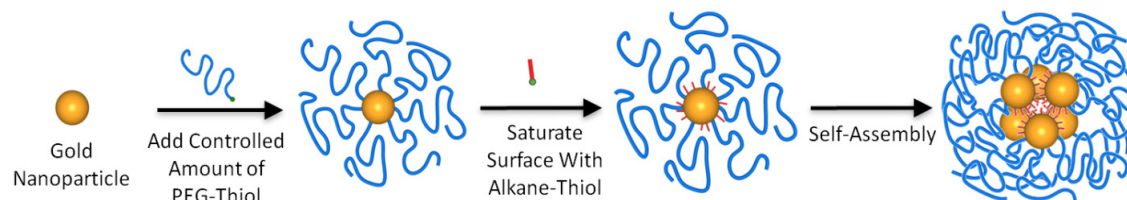


Figure 1.3. Schematic representation of the new method for surface functionalization and assembly of gold nanoparticles.

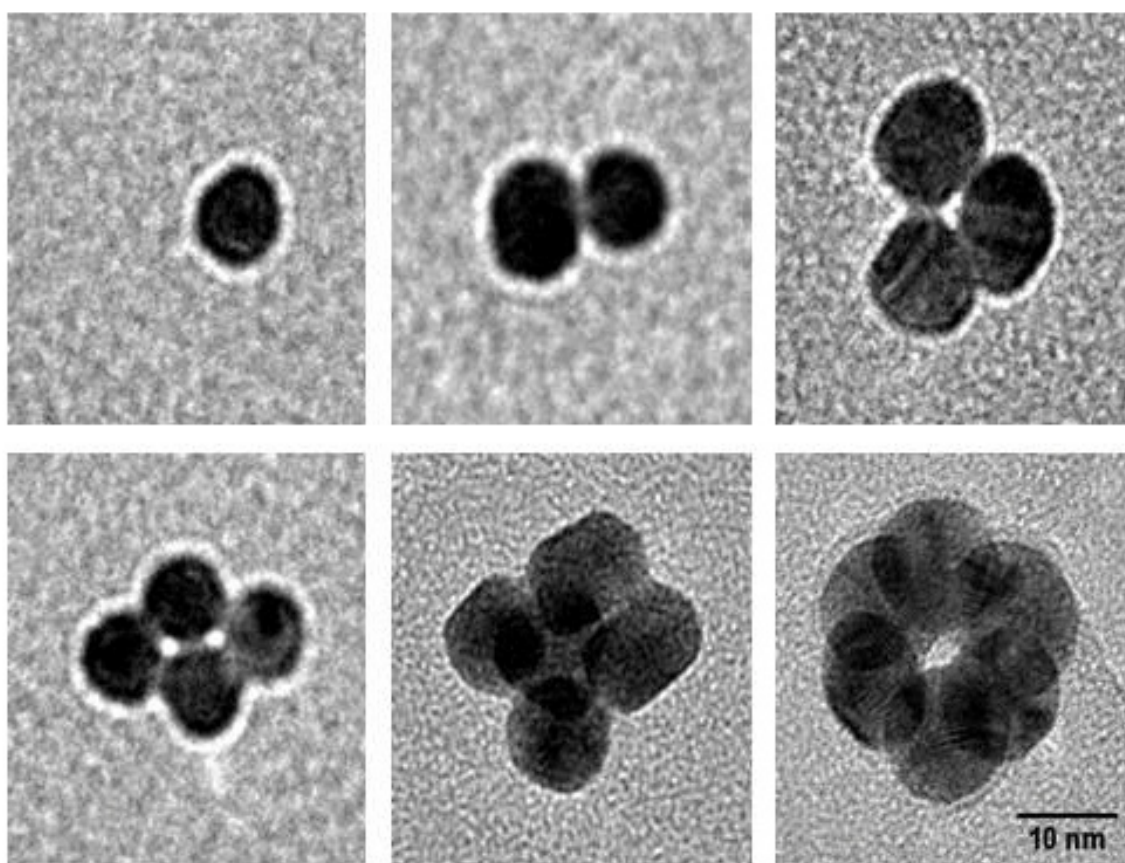


Figure 1.4. TEM images of gold nanoparticle clusters with singlet, doublet, triplet, tetrahedron, pentahedron and octahedron geometries.

In Chapter 5 we investigate the self-assembly and adsorption of charged nanoparticles at dispersed oil-in-water emulsion interfaces. The interaction potentials for negatively charged hexadecane droplets with anionic polystyrene latex particles or cationic gold particles are calculated using DLVO theory. Calculations demonstrate that increased ionic strength decreases the decay length of the electrostatic repulsion leading to enhanced particle adsorption. For the case of anionic PS latex particles, the energy barrier for particle adsorption is also reduced when the surface charge is neutralized through changes in pH. Complementary small-angle scattering experiments show that the highest particle adsorption for PS latex at the oil-water interface occurs at moderate ionic strength and low pH. For cationic gold particles, simple DLVO calculations also explain scattering results showing that the highest particle adsorption occurs at neutral pH due to the electrostatic attraction between oppositely charged surfaces. This work demonstrates that surface charges of particles and oil droplets are critical parameters to consider when engineering particle-stabilized emulsions.

The amphiphilic gold nanoparticles that we synthesize and use to prepare clusters are also effective emulsion stabilizers due to their dual functionality and surface activity. In Chapter 6 we examine the use of self-assembling gold nanoparticle surfactants to form stable Pickering emulsions, or particle-stabilized emulsions. The resulting structures are colloidosomes that have a tunable plasmon resonance in the near-infrared (NIR) wavelength region. The high NIR absorbance makes these colloidosomes potentially useful for applications in photothermal therapy and in photoacoustic imaging. When illuminated, the plasmonic nanoparticles can serve as a localized heat source, resulting in cell death for targeted cancerous tissues. For this particular application we engineer the

particles to have a specific inter-particle spacing at the oil-water interface in order to control the optical absorption in the NIR region. Figure 1.5 is a SEM image of one such nanoshell composed of 12 nm gold particles.

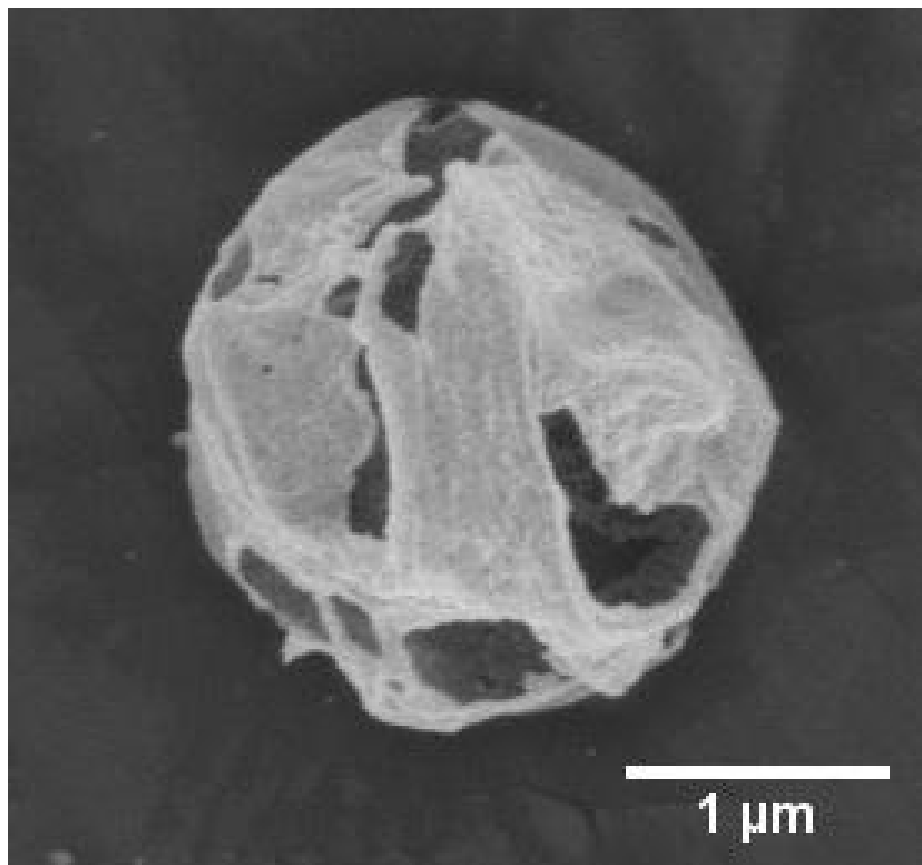


Figure 1.5. SEM image at taken 15000x magnification of a composite shell composed of 12 nm gold nanoparticles.

Chapter 2: Small Angle Scattering

Small angle scattering is a non-destructive analytical method used to determine the structure of a given sample. The primary benefit of scattering techniques is the ability to probe the sample structure in situ over a wide range of length scales (1-20,000 nm). Small angle scattering from light, x-rays and neutrons are analogous techniques that can be used to highlight different components of a sample. The research presented in this dissertation will utilize both small angle x-ray and neutron scattering (SAXS and SANS). The following chapter is meant to describe the basics of the technique, but more thorough explanations of scattering methods are available.⁵¹⁻⁵³

2.1 Introduction to technique

A schematic of a typical scattering experiment is located in Figure 2.1. Neutron or x-ray radiation is incident on a sample, and is absorbed, transmitted or scattered. A detector measures the intensity of the scattered radiation at a range of scattering angles, θ . Structural information is obtained from the radiation intensity as a function of the scattering angle. Because the scattering angle is dependent on the incident wavelength, scattering patterns are typically presented as functions of the wavevector, q . The wavevector, q , is defined as the difference between the propagation vectors of scattered, k_s , and incident, k_i , radiation and has units of reciprocal length. The magnitude of this vector is defined in Equation 2.1 where λ is the incident wavelength.

$$q = \frac{4\pi}{\lambda} \sin \theta \quad (2.1)$$

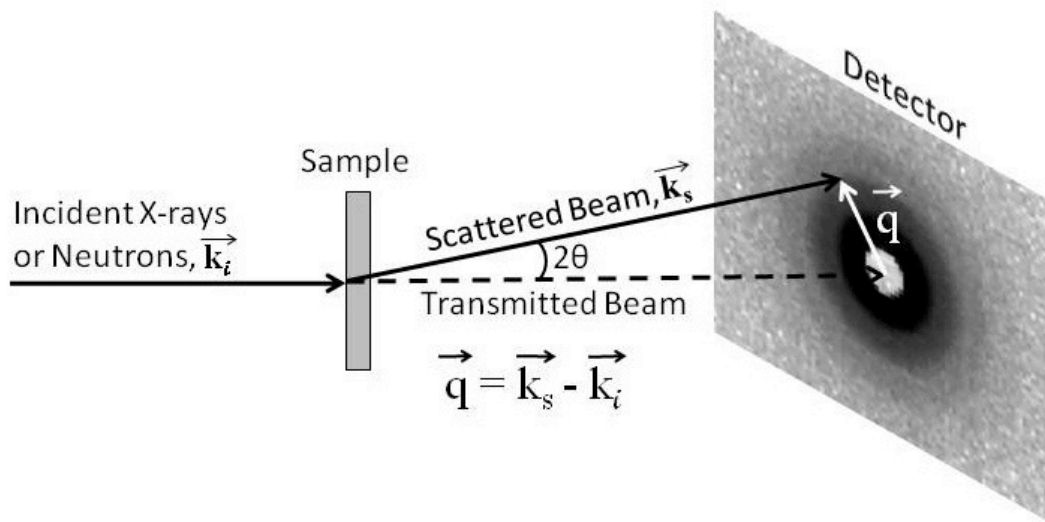


Figure 2.1. Schematic diagram of a small angle scattering experimental set-up.

Neutrons or x-rays are generated and collimated into a beam so that they are all moving in the same direction. For neutrons, this collimation occurs with a series of apertures over several meters until the neutrons are in a point beam. The x-ray fluxes used in this study are much lower, so the beam is line collimated in order to increase the incident intensity. While this makes it possible to collect data over a shorter time, it also causes smearing in the data curves. The curves can be mathematically desmeared using the Lake iterative method and then analyzed as if in point collimation.⁵⁴ Alternatively, models can be mathematically smeared to match the experimental SAXS data using the DANSE software developed at NIST.⁵⁵

Incident photons or neutrons are scattered by every atom and the scattering is therefore a function of the arrangement of atoms in the sample. Rayleigh *x-ray* scattering occurs when photons collide with electrons, and the scattering intensity of a material

depends on the number of electrons in the material.⁵¹ For this reason, materials with a high electron density will scatter the most. The intensity of elastic *neutron* scattering is dependent on the mass density and scattering length of neutrons in a given sample.⁵³ The scattering length corresponds to the amplitude of the scattered wave relative to that of the incident wave. It is possible to define the strength of scattering as the scattering length density (SLD) based on the average x-ray or neutron interactions in a material.

The scattering length density, ρ , is defined as the ratio of the scattering length per molecule and the molecular volume. Equation 2.2 gives the scattering length density for an A_mB_n molecule where b is the coherent scattering length of the atoms and v is the volume occupied by the molecule.⁵³

$$\rho_{A_mB_n} = \frac{mb_A + nb_B}{v} \quad (2.2)$$

The total scattering intensity in a sample arises from differences in SLD between sample phases. Equation 2.3 gives the general scattering intensity equation for a composite sample of i different particles in a solution with different SLD's.

$$I(q) = \sum_{i=1}^n (\rho_i - \rho_{sol})^2 I_{ii}(q) + \sum_{i \neq j} 2(\rho_i - \rho_{sol})(\rho_j - \rho_{sol}) I_{ij}(q) \quad (2.3)$$

The scattering equation for a composite sample with two different components in a solvent is simplified to Equation 2.4.

$$I(q) = (\rho_1 - \rho_{sol})^2 I_{11}(q) + (\rho_2 - \rho_{sol})^2 I_{22}(q) + 2(\rho_1 - \rho_{sol})(\rho_2 - \rho_{sol}) I_{12}(q) \quad (2.4)$$

The terms I_{11} and I_{22} are the self-correlation terms for identical particles while I_{12} is the cross-correlation of two unlike particles.

2.1.1 Contrast Matching

One added benefit to neutron scattering is the ability to highlight different components in a sample by contrast matching. Because atomic isotopes have different neutron coherent scattering lengths, it is possible to tune the effective material scattering length density without altering its chemical and physical properties. In the contrast matching technique, the solvent scattering length density is usually adjusted to match that of a sample component, thereby eliminating the scattering that would otherwise arise from that component. By matching the SLD of the solvent to one component in 3-component system, the scattering equation can be simplified so that the scattering intensity is only from the second component.

$$I(q) = (\rho_1 - \rho_{sol})^2 I_{11}(q) \text{ when } \rho_{sol} = \rho_2 \quad (2.5)$$

Deuterium atoms are most often used in place of hydrogen atoms because hydrogen is one of the most common elements. Additionally, they have extremely different scattering lengths, making it possible to adjust the contrast over a wide SLD range. For example, the neutron SLD of H₂O is $-5.6 \times 10^{-7} \text{ \AA}^{-2}$ and D₂O is $6.33 \times 10^{-6} \text{ \AA}^{-2}$. If the desired SLD is $2.9 \times 10^{-6} \text{ \AA}^{-2}$ a 50:50 volume ratio of H₂O to D₂O can be used to adjust the isotopic composition of the water and therefore alter the scattering length density.

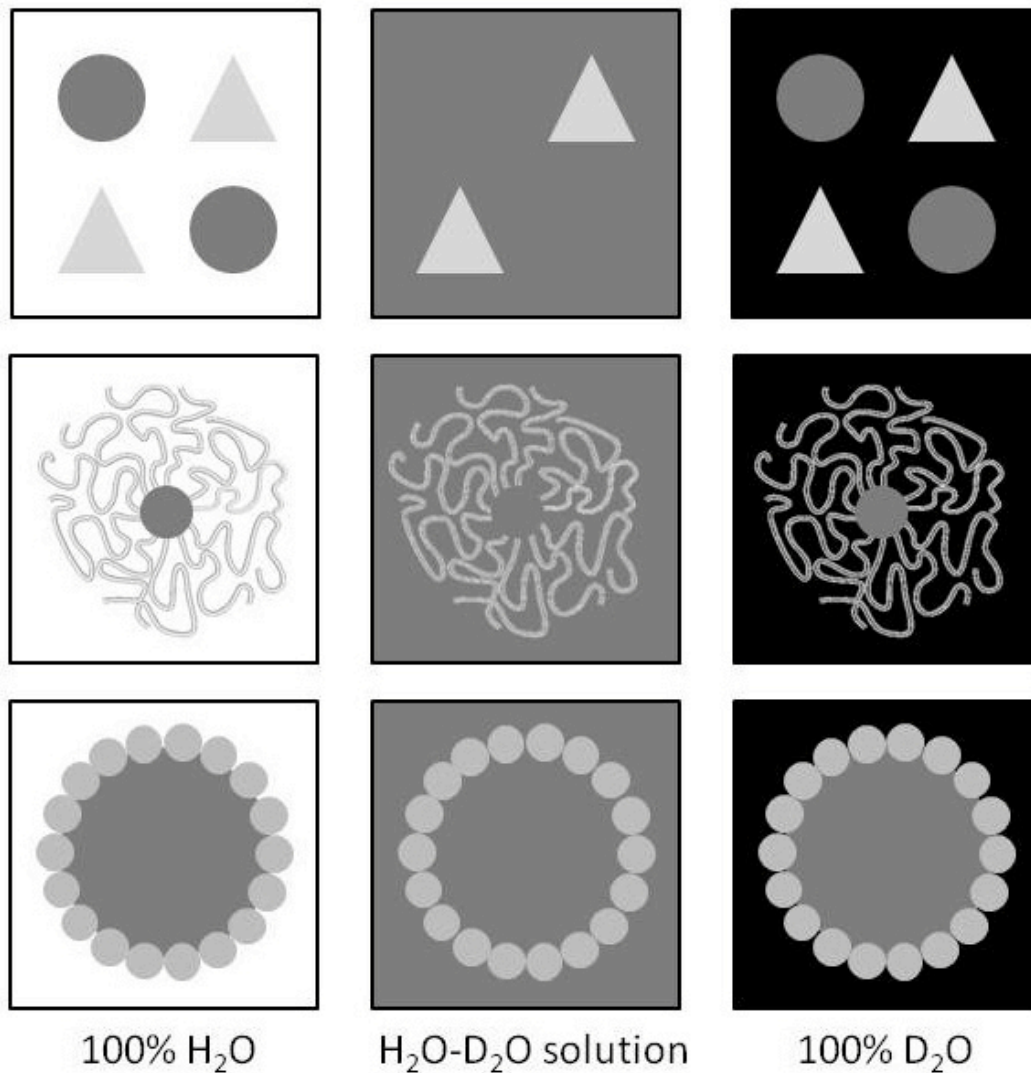


Figure 2.2. Schematic demonstration of the contrast matching technique.

This principle is further explained schematically in Figure 2.2. In the top row, the circles and triangles represent two different types of particles, and the shades of gray represent different SLDs. In the extreme cases of a solvent that is all H_2O (white background) or all D_2O (black background), both the circles and squares are still visible. By mixing isotopes to adjust the SLD of the solvent phases, it is possible to match the

SLD to one of the dispersed phases until it disappears. This is shown in the center box where the circles are no longer visible and only scattering from the triangles would occur.

The contrast matching technique is utilized in the SANS study of Pickering emulsions that is described in Chapter 5 of this dissertation. SANS is used to explore the arrangement of polystyrene latex particles in a hexadecane-in-water emulsion. In order to eliminate the scattering of the oil phase, a 6 vol% H₂O in D₂O mixture is used as the solvent and 11.2 vol% h-hexadecane in d-hexadecane is used as the oil phase so that all of the scattering intensity is from the PS latex particles. This is demonstrated schematically in the bottom row of Figure 2.2.

While the SLD of the material may be determined theoretically using Equation 2.2, it is much more accurate to find the contrast match point experimentally. This experiment is carried out at several different deuterated to hydrogenated solvent ratios with only the component that is to be matched in the dispersed phase. For the Pickering emulsion study, the contrast match point is determined by emulsifying a 11.2 vol% h-hexadecane in d-hexadecane solution in different water isotopes. The square root of the scattering intensity at a given q value ($q=0.004 \text{ \AA}^{-1}$) is plotted as a function of isotopic composition. The contrast match point is the isotope composition where the scattering intensity is zero. Figure 2.3 shows the contrast match plot for the hexadecane in water emulsions with a match point of 6 vol% H₂O in D₂O.

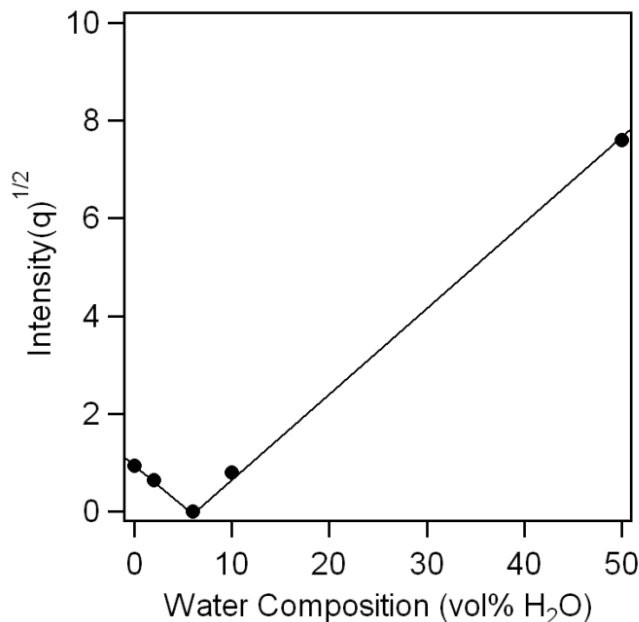


Figure 2.3. Experimental determination of the contrast match point for 11.2 vol% h-hexadecane in d-hexadecane oil-droplets in water. The scattering intensity at $q=0.004 \text{ \AA}^{-1}$ is eliminated at 6 vol% H₂O in D₂O.

In x-ray scattering, the SLD's for materials are fixed because they are based on the electron density. However, materials can be carefully chosen so that SLD of one component is much greater than both the solvent and the other component. This will cause one component to dominate the scattering intensity. The x-ray scattering length density of gold is extremely high because it is a very electron dense material ($\rho_{Au} = 1.25 \cdot 10^{-4} \text{ \AA}^{-2}$) and is much greater than water and hexadecane ($\rho_{H_2O} = 7.52 \cdot 10^{-6} \text{ \AA}^{-2}$ and $\rho_{C_{16}H_{34}} = 9.46 \cdot 10^{-6} \text{ \AA}^{-2}$). This makes SAXS especially useful for studying gold nanoparticles in both of the systems presented in this dissertation.

2.1.2 Basic Data Analysis Methods

One simple method for approximating the size of particles and clusters is a Guinier analysis.⁵⁶ The radius of gyration, R_g , is a size parameter that is calculated from

Equation 2.6 where q is the scattering vector and a_0 is the zero angle intensity. For this analysis, the scattering data are plotted as $\ln[I(q)]$ versus q^2 . The slope is determined at low q and used to calculate R_g as long as the slope is constant. If the particles are known to be monodisperse spheres, the particle radius can be determined by $R = \sqrt{\frac{5}{3}} R_g$.

$$\ln[I(q)] = \ln[a_0] - \frac{R_g^2}{3} q^2 \quad (2.6)$$

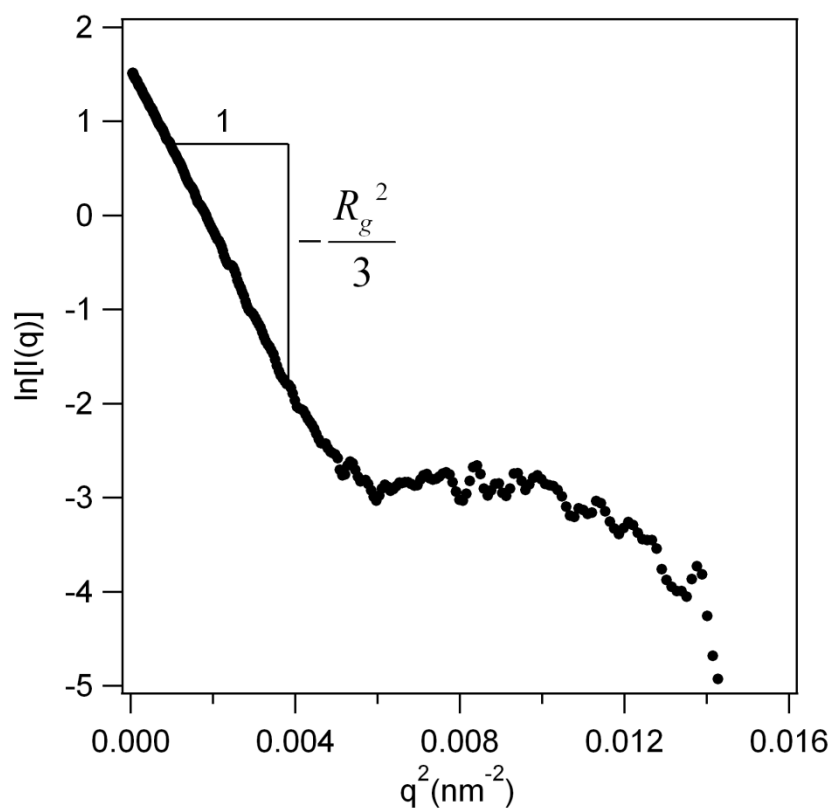


Figure 2.4. Guinier analysis for monodisperse gold nanoparticles in water where $R_g = 5.15$ nm and $R = 6.6$ nm.

While the Guinier analysis is useful for determining the approximate size of particles, the scattering can be analyzed more rigorously using direct modeling. The scattering intensity of a simple two-component system can be modeled as the self-

correlation of discrete entities (e.g. particles). This is typically divided into the contributions from the individual particle's size and shape and contributions from the arrangement of particles in the sample. Equation 2.7 is the resulting scattering model where N is the number of particles, V_p is the volume of a single particle, $\Delta\rho^2$ is the contrast factor, bkg is the incoherent background, $P(q)$ is the single particle form factor and $S(q)$ is the inter-particle structure factor.

$$I(q) = NV_p^2 \Delta\rho^2 P(q)S(q) + bkg \quad (2.7)$$

The form factor accounts for the scattering that occurs from one particle. Each atom within the particle will produce a scattering wave that is sent to the detector. All of the wave amplitudes are summed, resulting in a unique interference pattern. The pattern oscillates in a way that is characteristic for the shape of the particle. The form factor can be mathematically calculated using Equation 2.9. The form factor, $P(q)$, is defined as the density correlation function integrated over the particle volume.

$$P(q) = \left[\frac{1}{V_p} \int_{V_p} e^{iqr} dr \right]^2 \quad (2.9)$$

The simplest particle geometry is the monodisperse sphere. Assuming a uniform density, the form factor for monodisperse spheres, $P_s(q)$, is given in Equation 2.10 where R is the particle radius and $J_1(x)$ is a Bessel function of the first order.

$$P_s(q) = \left[\frac{3J_1(qR)}{qR} \right]^2 = 9 \left[\frac{\sin(qR) - qR \cos(qR)}{(qR)^3} \right]^2 \quad (2.10)$$

Polydisperse spheres will have a form factor that is a weighted sum based on the particle size distribution.

Particle form factors can also be determined experimentally at extremely dilute conditions. At these concentrations the spatial correlations between particles are negligible and the structure factor is effectively one. The SANS scattering form factor for 80 nm polystyrene latex spheres is shown in Figure 2.5. The data are fit with a sphere model using the NIST Igor macros and the exact radius is found to be 40.65 nm given the known concentration (0.228 vol% PS) and scattering length densities ($\rho_{PS}=1.518*10^{-6} \text{ \AA}^{-2}$, $\rho_{solvent}=6.02*10^{-6} \text{ \AA}^{-2}$).⁵⁷

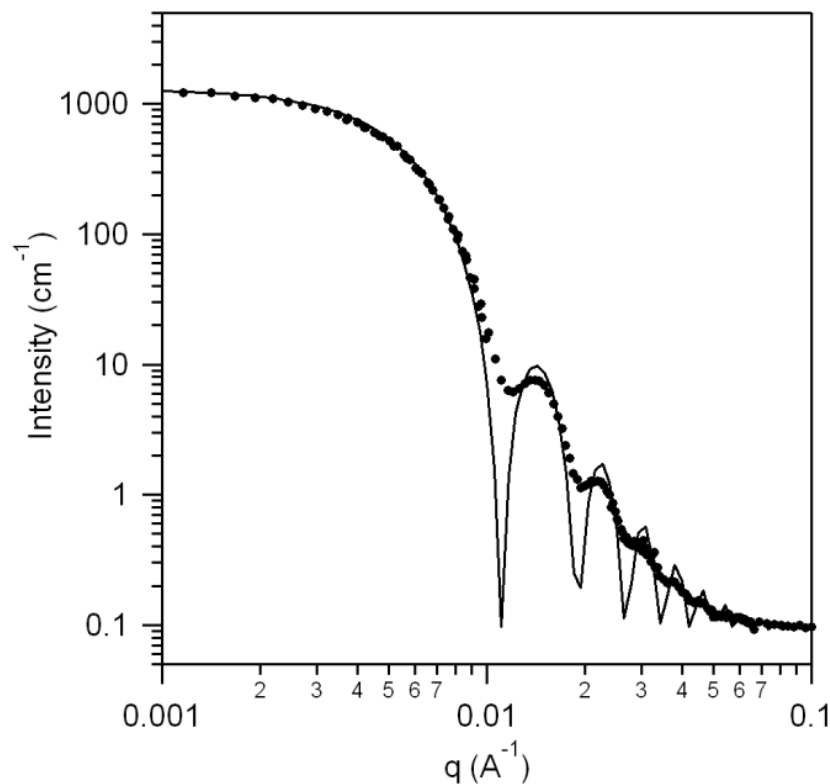


Figure 2.5. Experimental scattering curve for 80nm polystyrene latex particles in water. The spherical form factor has the following fit parameters: $\phi = 0.228$ vol% PS, $R = 406.45 \text{ \AA}$, $\rho_{PS}=1.518*10^{-6} \text{ \AA}^{-2}$, $\rho_{solvent}=6.02*10^{-6} \text{ \AA}^{-2}$ and $bkg=0.0926$.

The structure factor accounts for scattering due to cross correlations between particles. This usually occurs when the distances between particles is on the same order

of magnitude as the particle size. Therefore, a structure factor arises if the particles are concentrated or if they are assembled in close proximity. Most information about the particle arrangement is given in the low q portion of the scattering curve. At high q , the structure factor goes to 1 so that the resulting scattering intensity matches the form factor. Figure 2.6 shows an example of a form factor for 80 nm polystyrene latex particles ($P(q)$) and the structure factor for a 0.25 vol% PS latex stabilized hexadecane emulsion at a pH of 2.5 and 20 mM NaCl ($S(q)$). The overall intensity curve is a product of the form factor and structure factor.

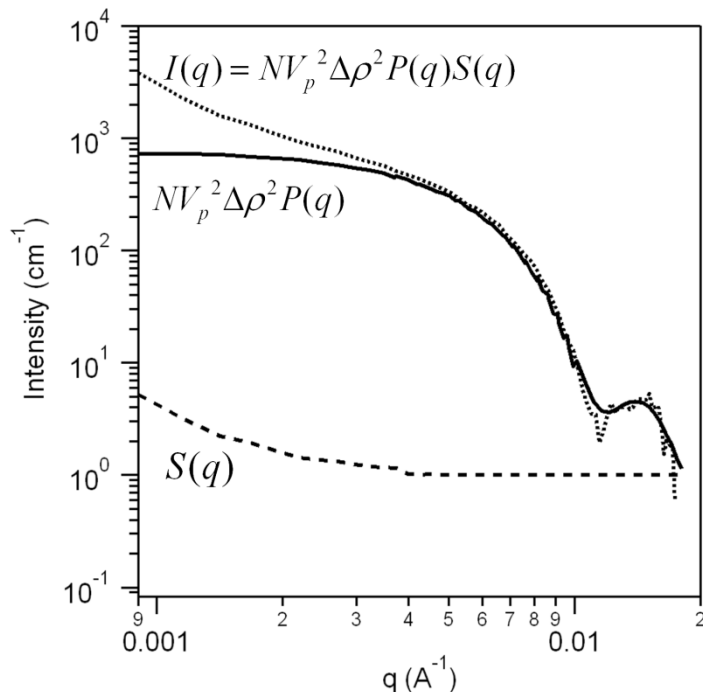


Figure 2.6. The SANS profile (dotted) of a 0.25 vol% PS latex ($R=40$ nm) stabilized hexadecane emulsion at a pH of 2.5 and 20 mM NaCl is the product of the form factor of the single PS latex particles (solid) with the structure factor of the particle positions (dashed).

If the particles are ordered in a crystalline arrangement, a correlation peak will form. The peak arises when the interference patterns from a highly ordered sample

combine constructively. The particle spacing within the crystalline arrangement, d , can be roughly approximated by the location of the correlation peak using Equation 2.11.

$$d \approx \frac{2\pi}{q_{peak}} \quad (2.11)$$

Scattering models should be used to obtain quantitative structural information from the experimental data. In this dissertation, two models will be used to analyze scattering data. The classic Debye Model is used to model the scattering of structures composed of spherical subunits. This approach is used to analyze the self-assembled gold particles described in Chapter 3. In principle, the Debye Model can also be used to study the particle-stabilized emulsions discussed in Chapter 5, however, this approach becomes quite cumbersome with the number of particles involved in each emulsion droplet. Therefore, we developed a Pickering Model that can be used to accurately determine the structure of particle-stabilized emulsions.⁵⁸

2.2 Debye Model

The Debye Model is the simplest model used for complexes made up of spherical particle subunits.⁵⁹ It accounts for correlations between particles based on the separation distances between each particle in the complex. This model is used in combination with a form factor model that describes the size and shape of the particles. In this case we use Rayleigh's equation for monodisperse spherical particles.⁶⁰ Equation 2.12 is a simplified Debye Equation for clusters consisting of identical spherical particles.⁵⁹ $F(q)$ is the scattering contribution for a sphere given by Equation 2.13, where $\Delta\rho$ is the scattering contrast, V is the volume of one subunit, q is the scattering vector and R is the radius. In

these equations, r_{ij} is the separation distance between the centers of particles i and j . We developed models for nine possible cluster geometries that are used in Chapter 3: doublet, triplet, tetrahedral, trigonal dipyramidal, octahedral, pentagonal dipyramidal, snub disphenoid, triaugmented triangular prism and gyroelongated square dipyramid. For each configuration, x is the nearest neighbor separation distance. As an example, the Debye Model equation for a doublet is given in Equation 2.14 where x is the distance between the centers of the two particles. A schematic of the particle separation distance determination for each cluster geometry and its corresponding equation is shown in Figure 2.7. Figure 2.8 shows the calculated scattering curves for each cluster geometry.

$$I(q) = \sum_{i=1}^N F_i(q)^2 + 2 \sum_{i=1}^{N-1} \sum_{j=i+1}^N F_i(q) F_j(q) \frac{\sin qr_{ij}}{qr_{ij}} \quad (2.12)$$

$$F_i(q) = (\Delta\rho)V_i \frac{3[\sin(qR_i) - qR_i \cos(qR_i)]}{(qR_i)^3} \quad (2.13)$$

$$I(q) = F(q)^2 \left[2 + 2 \frac{\sin(qx)}{qx} \right] \quad (2.14)$$

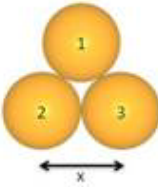
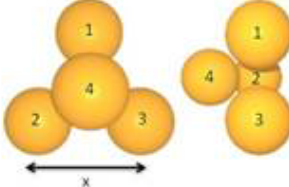
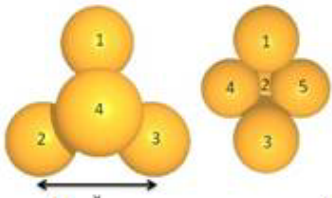
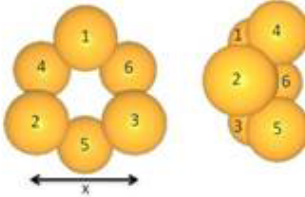
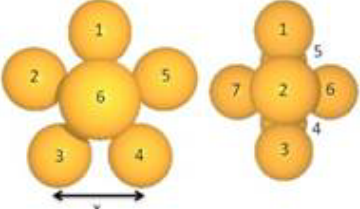
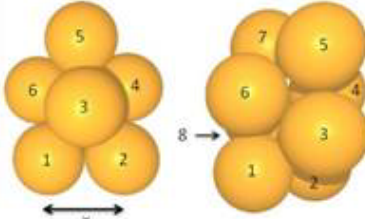
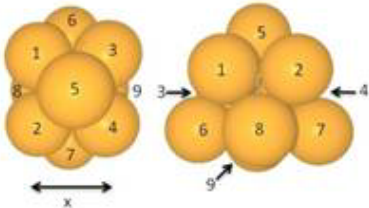
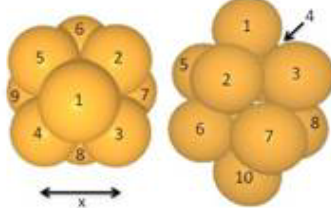
<p style="text-align: center;">Triplet</p>  $I(q) = F(q)^2 \left[3 + 6 \frac{\sin(qx)}{qx} \right]$	<p style="text-align: center;">Tetrahedron</p>  $I(q) = F(q)^2 \left[4 + 12 \frac{\sin(qx)}{qx} \right]$
<p style="text-align: center;">Trigonal Dipyramid</p>  $I(q) = F(q)^2 \left[5 + 18 \frac{\sin(qx)}{qx} + 2 \frac{\sin(\sqrt{8/3} qx)}{\sqrt{8/3} qx} \right]$	<p style="text-align: center;">Octahedron</p>  $I(q) = F(q)^2 \left[6 + 24 \frac{\sin(qx)}{qx} + 6 \frac{\sin(\sqrt{2}qx)}{\sqrt{2}qx} + \dots \right]$
<p style="text-align: center;">Pentagonal Dipyramid</p>  $I(q) = F(q)^2 \left[7 + 30 \frac{\sin(qx)}{qx} + 10 \frac{\sin(1.62qx)}{1.62qx} + 2 \frac{\sin(1.05qx)}{1.05qx} \right]$	<p style="text-align: center;">Snub Disphenoid</p>  $I(q) = F(q)^2 \left[8 + 36 \frac{\sin(qx)}{qx} + 18 \frac{\sin(1.51qx)}{1.51qx} + 2 \frac{\sin(1.29qx)}{1.29qx} \right]$
<p style="text-align: center;">Triaugmented Triangular Prism</p>  $I(q) = F(q)^2 \left[9 + 42 \frac{\sin(qx)}{qx} + 12 \frac{\sin(\sqrt{2}qx)}{\sqrt{2}qx} + 12 \frac{\sin(1.65qx)}{1.65qx} + 6 \frac{\sin(1.73qx)}{1.73qx} \right]$	<p style="text-align: center;">Gyroelongated Square Dipyramid</p>  $I(q) = F(q)^2 \left[10 + 48 \frac{\sin(qx)}{qx} + 8 \frac{\sin(\sqrt{2}qx)}{\sqrt{2}qx} + 16 \frac{\sin(1.55qx)}{1.55qx} + 16 \frac{\sin(1.7qx)}{1.7qx} + 2 \frac{\sin(2.26qx)}{2.26qx} \right]$

Figure 2.7. Schematic of cluster geometries and corresponding equations for particles of identical size and shape.

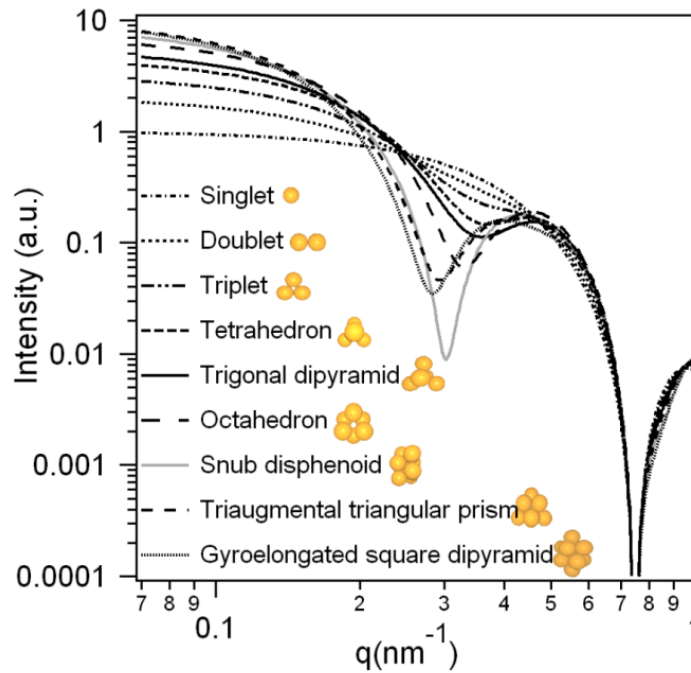


Figure 2.8. Calculated scattering profiles for expected particle geometries using the Debye Model.

For Pickering emulsions, we can model the scattering for a large oil droplet decorated with smaller particles on the surface with the Debye equation. The form factor of each spherical subunit, $F(q)$, is again given by Equation 2.13. In the Debye equation for this system (Equation 2.15), the first two terms account for the scattering contributions of the oil droplets and particles respectively. The third term is the cross-correlations between the oil droplet and individual particles and the last term is the cross-correlations of particles within the shell where N is the number of particles, r_{ij} is the inter-particle distance and δ is the particle penetration depth. As an example, Figure 2.9 shows scattering curves that are calculated for an emulsion with 1 μm contrast-matched oil droplets and several particle loadings. The particles are assumed to be equally spaced and the coordinates of each particle is determined using the GenCoords algorithm.

$$I(q) = F_o(q)^2 + NF_p(q)^2 + 2NF_o(q)F_p(q)\frac{\sin q(R_o + \delta)}{q(R_o + \delta)} + 2\sum_{i=1}^{N-1}\sum_{j=i+1}^N F_p(q)^2 \frac{\sin qr_{ij}}{qr_{ij}} \quad (2.15)$$

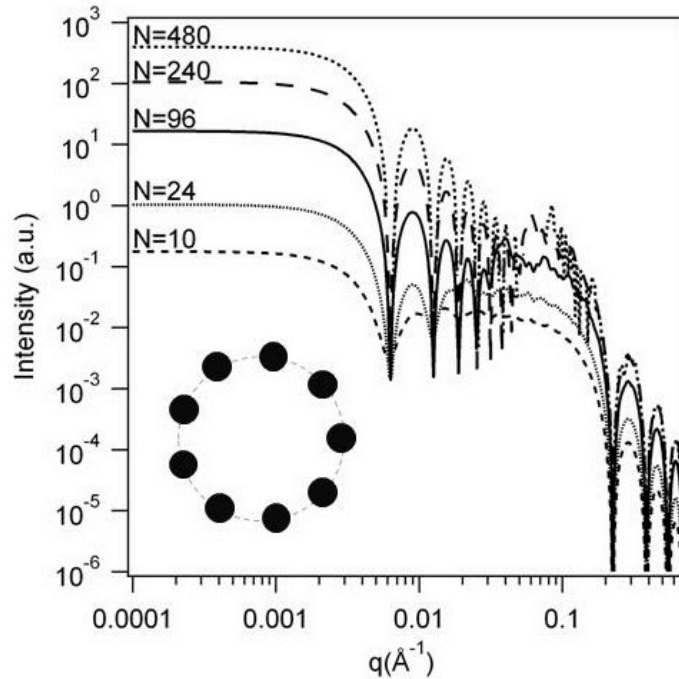


Figure 2.9 Comparison of predicted scattering based on Debye Model for an emulsion with contrast-matched oil with varying numbers of equally-spaced adsorbed particles. Parameters used for the modeling are $R_o=500 \text{ \AA}$, $R_p=20 \text{ \AA}$, $\Delta\rho_o=0$, $\Delta\rho_p=2.55E-6 \text{ \AA}^{-2}$, $\delta=0$.

2.3 Pickering Model

Small angle scattering is an ideal technique for studying particle-stabilized emulsions, however a good structural model did not previously exist for characterizing these systems. Here we develop the Pickering Model that analytically describes the small angle scattering of Pickering emulsions and raspberry particles where the central core has a different scattering length density than the spherical particles decorating the surface and than the surrounding solvent.⁵⁸ The model combines relatively simple self correlation and cross terms for spherical particles into an overall form factor for the entire complex. The

model can be used to describe the scattering signal over the complete q range and at any arbitrary contrast value. With this model, we can also evaluate the sensitivity of scattering experiments such as Small Angle X-ray Scattering (SAXS), Small Angle Neutron Scattering (SANS) and Ultra-Small Angle Neutron Scattering (USANS) to various levels of particle adsorption and to the penetration depth of the particles. Still, in its present form, the model is limited in that it cannot account for strong particle correlations in the plane of the interface such as those that occur when 2D hexagonal crystals are formed.

Figure 2.10 shows a schematic of a large oil droplet surrounded by several smaller particles forming a structure similar to that of Pickering emulsions. In order to calculate a new form factor for the entire complex, the self-correlation terms of the oil, the self-correlation terms of the particles, the correlation terms between different particles and the cross terms between oil and particles all need to be calculated.

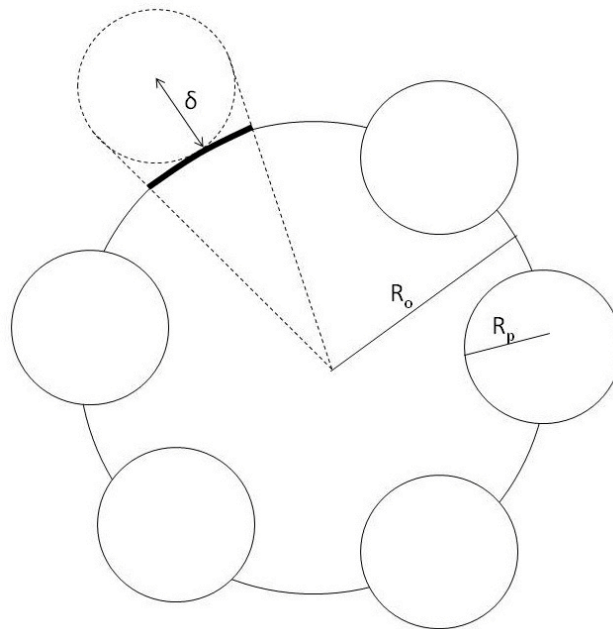


Figure 2.10. A schematic drawing of a Pickering emulsion oil-particle complex where δ is the penetration depth of the particle.

All terms are calculated based on the classic Debye equation.⁵⁹ In a way that is analogous to Pedersen's derivation of the scattering of a particle with Gaussian chains, we consider two infinitely thin shells of radii R_1 and R_2 separated by distance r .⁶¹ The general structure of the equation is then the form factor of the two shells multiplied by the phase factor that accounts for the separation of their centers.

$$S(q) = \frac{\sin(qR_1)}{qR_1} \frac{\sin(qR_2)}{qR_2} \frac{\sin(qr)}{qr} \quad (2.16)$$

In our case, the oil and the particles in the emulsion are solid spheres rather than thin shells. Therefore, the first two terms must be integrated over R_o and R_p respectively using the weighting function of a sphere ($p=4\pi R^2$). The integration and normalization yields the functions Ψ_o and Ψ_p shown in Equations 2.17 and 2.18.^{60, 62-66}

$$\Psi_o = \int_0^{R_o} (4\pi R_1^2) \frac{\sin(qR_1)}{qR_1} dR_1 = \frac{3[\sin(qR_o) - qR_o \cos(qR_o)]}{(qR_o)^2} \quad (2.17)$$

$$\Psi_p = \int_0^{R_p} (4\pi R_2^2) \frac{\sin(qR_2)}{qR_2} dR_2 = \frac{3[\sin(qR_p) - qR_p \cos(qR_p)]}{(qR_p)^2} \quad (2.18)$$

The cross term between the oil and the particles is also derived from the Debye equation. Here we initially assume that the particle is wet equally by the oil and water phases so that the particle center lies exactly at the interface. In this case the phase factor is integrated over R_o because that is the separation between the centers of the oil and the particles.

$$S_{op} = \Psi_o \Psi_p \frac{\sin(qR_o)}{qR_o} \quad (2.19)$$

The cross term between two particles is slightly more complex. The phase factor in this expression must be averaged over the pair distance distribution function of an infinitely thin shell with radius R_o . The particles are assumed to be mobile and evenly distributed around the oil droplet surface. Therefore, the thin shell probability function is used as an approximation because the particle positions in a real emulsion are time and ensemble averaged. Convolution of the expressions for the thin shell and the sphere results in the following particle-particle correlation term:

$$S_{pp} = \Psi_p^2 \left[\frac{\sin(qR_o)}{qR_o} \right]^2 \quad (2.20)$$

This treatment of the phase factor limits the ability of the model to simulate strong correlations in the plane of the interface such as those that could occur due to hexagonal close-packing organization.

The equations derived above assume that the particles sit exactly at the center of the oil-water interface. In Pickering emulsions, the penetration depth of the solid particles into the oil will likely depend on how well the particle surface is wet by both fluids (contact angle). Similarly, raspberry colloids could also have the small spherical particles sitting at different positions depending on the method of synthesis.⁶⁷ Therefore, it is necessary to adjust the position of the particles to simulate variability in penetration depth. This effect can be modeled by replacing R_o in the phase factor with an effective radius $R_o + \delta R_p$ where $-1 \leq \delta \leq 1$.⁶¹

$$S_{op} = \Psi_o \Psi_p \frac{\sin(q(R_o + \delta R_p))}{q(R_o + \delta R_p)} \quad (2.21)$$

$$S_{pp} = \Psi_p^2 \left[\frac{\sin(q(R_o + \delta R_p))}{q(R_o + \delta R_p)} \right]^2 \quad (2.22)$$

An important parameter in the characterization of Pickering emulsions is the percentage of oil surface area that is covered or shadowed by solid particles. Even when δ is non-zero, the particles will still prevent other particles from using the surface that is shadowed by their cross section as illustrated in Figure 2.10. Therefore, in this model we use the effective radius, $R_o + \delta R_p$, to calculate the fraction of interfacial area covered (χ) in order to describe the extent of particle packing. The maximum coverage possible with hexagonally close-packed monodisperse particles is approximately 0.90. The fraction of area that is covered is calculated according to Equation 2.23 where ϕ_p^T is the volume fraction of particles, ϕ_o is the volume fraction of oil in the total volume and ϕ_p^a is the fraction of the total particles that are adsorbed at the oil-water interface.

$$\chi = \frac{4\phi_p^T \phi_p^a (R_o + \delta R_p)}{\phi_o R_p} \quad (2.23)$$

The number of particles at the surface of a single oil droplet, N_p , is calculated as a function of the fraction area coverage (χ) where V_o is the volume of a single oil drop and V_p is the volume of a single solid particle.

$$N_p = \frac{\phi_p^T \phi_p^a V_o}{\phi_o V_p} = \chi \frac{4R_p}{(R_o + \delta R_p)} \frac{V_o}{V_p} \quad (2.24)$$

The form factor of the entire complex can now be calculated using $\Delta\rho_o$ and $\Delta\rho_p$ as the excess scattering length densities of the oil and the particles where $\Delta\rho_o = |\rho_o - \rho_s|$ and $\Delta\rho_p = |\rho_p - \rho_s|$. The prefactor, M , is the total scattering length of the whole complex.

$$P_{op} = \frac{1}{M^2} \left[\begin{aligned} &(\Delta\rho_o)^2 V_o^2 \Psi_o^2 + N_p (\Delta\rho_p)^2 V_p^2 \Psi_p^2 \\ &+ N_p (N_p - 1) (\Delta\rho_p)^2 V_p^2 S_{pp} + 2N_p \Delta\rho_o \Delta\rho_p V_o V_p S_{op} \end{aligned} \right] \quad (2.25)$$

$$M = \Delta\rho_o V_o + N_p \Delta\rho_p V_p \quad (2.26)$$

Equations 2.23-26 can be used directly to evaluate and model the scattering of raspberry particles. On the other hand, Pickering emulsions will usually have an excess of free particles that are not adsorbed. The final expression for the scattering of monodisperse Pickering emulsions is given in Equation 2.27 where the first term represents the scattering of the core-particle complex and the second term represents the free particles.

$$I_{Total}^{Mono}(q) = I_{op}^{Mono}(q) + I_p^{Mono}(q) \quad (2.27)$$

$$I_{Total}^{Mono}(q) = \left(\phi_o (\Delta\rho_o)^2 V_o + \phi_p^T \phi_p^a N_p (\Delta\rho_p)^2 V_p \right) P_{op} + \phi_p^T (1 - \phi_p^a) (\Delta\rho_p)^2 V_p \Psi_p^2$$

In real systems, particularly in the case of Pickering emulsions, the spherical core will have significant polydispersity. Therefore, we must define $I_{op}(q)$ for the oil-particle complex as

$$I_{op}^{Poly}(q) = \int f(R) I_{op}^{Mono}(q, R) dR \quad (2.28)$$

where $f(R)$ is a Gaussian distribution to describe radii and the remaining terms inside the integral are the scattering contribution of the core-particle complex.

$$f(R) = \frac{1}{\sigma\sqrt{2\pi}} \exp\left[-\frac{1}{2\sigma^2} (R - R_{avg})^2\right] \quad (2.29)$$

The total scattering of the core-particle complexes and free particles in solution is then given by

$$I_{Total}^{Poly}(q) = I_{op}^{Poly}(q) + I_p^{Mono}(q) \quad (2.30)$$

The average core volume, $\langle V_o \rangle$, is calculated outside of the integral, where $p = \sigma / R_{avg}$.

The average core volume is then used to determine the average number of particles at the interface, N_p , and the fraction of particles adsorbed at the interface, χ .

$$\langle V_o \rangle = \frac{4\pi}{3} \langle R_o^3 \rangle = \frac{4\pi}{3} R^3 (1 + 3p^2) \quad (2.31)$$

The Pickering model is not designed for systems where the small particles are highly polydisperse. Polydispersity of the small adsorbed particles is much more challenging to account for because the model needs to include individual particle-particle correlation terms for every type of particle pair. Additionally, it is well known that the energy of adsorption of particles at oil-water interfaces scales with R^2 .⁶⁸ Therefore, preferential adsorption of larger particles could be expected to occur for polydisperse particles. For these two reasons, the model should not be used in the case of highly polydisperse small particles.

It should be noted that these equations do not account for the smearing that occurs due to the finite resolution of real scattering instruments. Smearing effects need to be considered when the model is used to fit any real scattering data. Fortunately, curve fitting with instrumental smearing for this and any arbitrary model can be easily performed with free software routines that take into consideration the resolution function of individual instrument configurations.⁵⁷

2.3.1 Applications of Model

The need for a scattering model that can effectively describe these particle complexes is highlighted by considering the core-shell model that is frequently used to fit emulsion interfaces (Figure 2.11). An equal scattering length is used to compare the raspberry model to the uniform spherical core-shell model. As expected, the core-shell model does a good job approximating the scattering in the low q region. However the models deviate significantly in the intermediate and high q range. Note that the largest

deviations occur in the SAXS and SANS range. Therefore, the Pickering model described above is essential to accurately model the scattering curves over the full angular range.

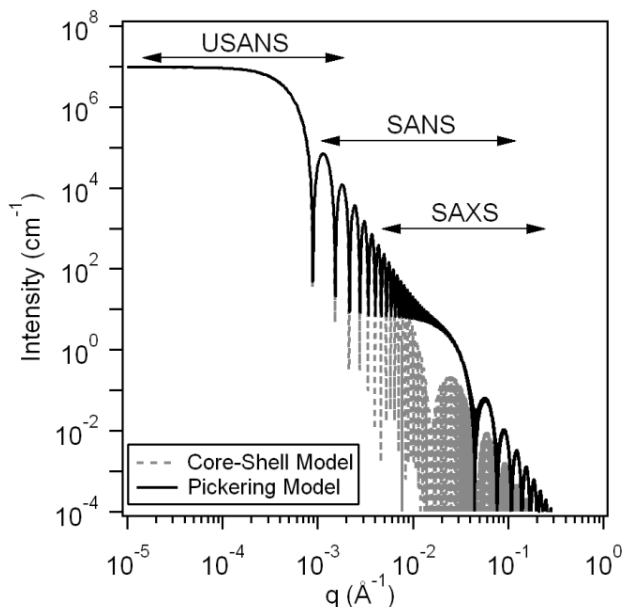


Figure 2.11. Comparison of core-shell model and Pickering model for $R_o=5000 \text{ \AA}$ core with $R_p=100 \text{ \AA}$ particles adsorbed at the surface. The calculation assumes 5% of the core surface area covered by particles. In the core-shell model an average shell thickness of 200 \AA is used with an average excess scattering length density of $8.60\text{E-}6 \text{ \AA}^{-2}$. The Pickering model assumes $\chi=0.05$, $\delta=0$, $\phi_p^T=0.0002$, $\rho_p=2.0*10^{-8} \text{ \AA}^{-2}$, $\rho_o=7.55*10^{-6} \text{ \AA}^{-2}$, and $\rho_w=9.46*10^{-6} \text{ \AA}^{-2}$. For the core-shell model the scattering length densities are $\rho_{shell}=8.6*10^{-6} \text{ \AA}^{-2}$, $\rho_{core}=7.55*10^{-6} \text{ \AA}^{-2}$, and $\rho_{solvent}=9.46*10^{-6} \text{ \AA}^{-2}$.

The predicted scattering signal for raspberry particles was also compared to that of spherical particles in order to determine the sensitivity of SANS and SAXS to these structural differences. Raspberry particles resemble a bumpy sphere when the core and particles have equal scattering length densities. Therefore, a solid sphere model might be considered a crude approximation to the real structure. Figure 2.12 illustrates the differences between the Pickering and the solid sphere models. The parameters used for the raspberry complex were $R_o=500 \text{ \AA}$, $R_p=200 \text{ \AA}$, $\chi=0.8$ and $\Delta\rho_o=\Delta\rho_p=9.44\text{E-}6 \text{ \AA}^{-2}$

(SAXS contrast). For the spherical model approximation we consider a radius (548 Å) that is equal to the volume average radius of the whole raspberry particle. Throughout most of the q range, the spherical model deviates significantly from the Pickering model. The differences between the two models are amplified when the decorating particles are larger relative to the core radius and when less of the core surface area is covered. For some samples these details may be lost due to the low resolution of some scattering instruments or due to large levels of polydispersity.

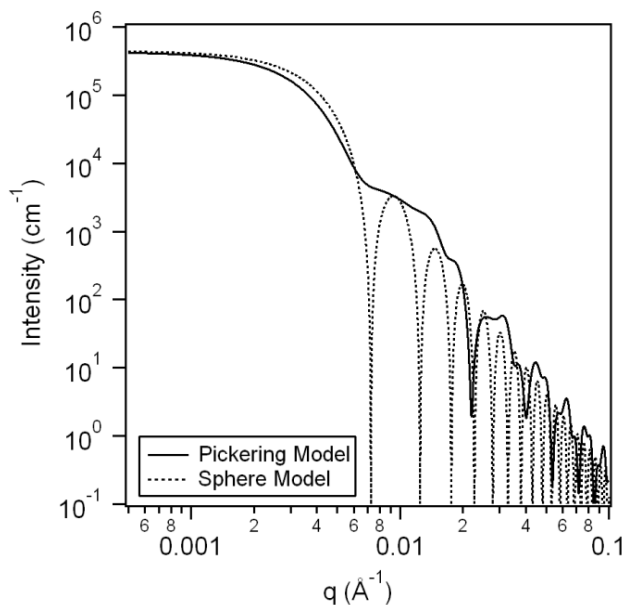


Figure 2.12. Comparison of the solid sphere model and the Pickering model for $R_o=500$ Å, $R_p=200$ Å, $\phi_o=0.05$, $\delta=1$, $\phi_p^T=0.046$, $\Delta\rho_o=\Delta\rho_p=9.44\text{E-}6$ Å⁻² and $\chi=0.8$. For the sphere model an average radius was assumed for the entire complex, $R=548$ Å.

Figure 2.13 shows the calculated form factor for a Pickering emulsion complex consisting of a spherical oil core with 50% interfacial area covered with smaller silica particles. The parameters describing the system are $R_o=1000$ Å, $R_p=100$ Å and $\phi_o=0.05$ with no free particles in solution. The particles are assumed to sit at the edge of the core surface with $\delta=1$. The form factor was calculated for the case where the core material was

contrast matched with the solvent so only the particles scatter and for the case where the core material was contrast matched with silica so the core and the adsorbed particles scatter equally. In the high q range, the scattering due to the smaller particles at the oil surface dominates the signal and the three profiles become similar.

The calculation also shows that the scattering is extremely sensitive to the scattering length density contrast of the core material in the low q region. The new model properly accounts for the excess scattering of both materials. Therefore, contrast matching is not critical when these values are known precisely. This is especially useful when performing SAXS experiments where contrast matching is challenging or not possible but the electron density of all phases may be known.

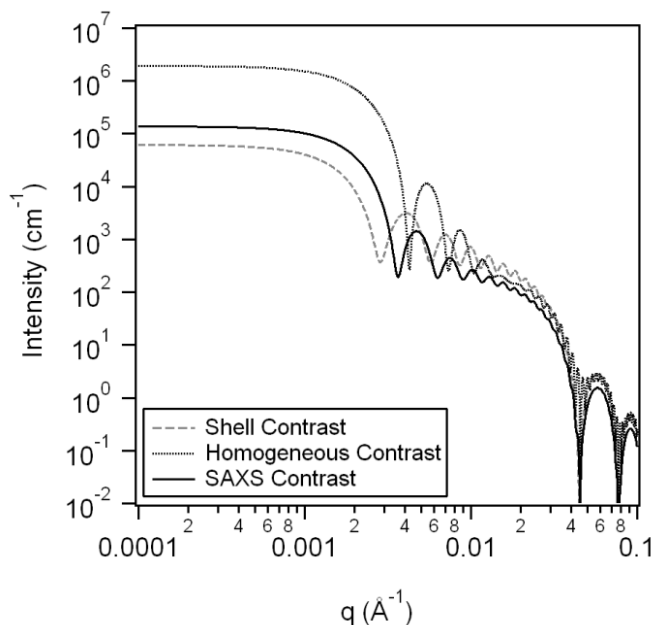


Figure 2.13. Calculated scattering of a Pickering emulsion complex with $R_o=1000 \text{ \AA}$, $R_p=100 \text{ \AA}$, $\phi_o=0.05$, $\delta=1$, $\phi_p^T=0.01$ and $\chi=0.50$. The “SAXS” contrast curve used $\Delta\rho_o=1.91\text{E-}6 \text{ \AA}^{-2}$ and $\Delta\rho_p=9.44\text{E-}6 \text{ \AA}^{-2}$. The “Shell” contrast curve used $\Delta\rho_o=0 \text{ \AA}^{-2}$ and $\Delta\rho_p=9.44\text{E-}6 \text{ \AA}^{-2}$. The “Homogeneous” contrast curve used $\Delta\rho_o=\Delta\rho_p=9.44\text{E-}6 \text{ \AA}^{-2}$.

The model was also used to explore the sensitivity of the scattering data to changes in the contrast and structural parameters. Figure 2.14 illustrates the sensitivity of

particle penetration depth at the oil-water interface of a typical Pickering emulsion. The calculated form factor for a hexadecane droplet with silica particles located at the oil-water interface is displayed. For the case of a large core ($R_o=5000 \text{ \AA}$) and small particles ($R_p=100 \text{ \AA}$), only slight changes in scattering intensity occur in the intermediate q region as the particles are moved from sitting entirely in the water phase to completely in the oil phase. As expected, it is found that the scattering of Pickering emulsions containing small particles is not highly sensitive to changes in the penetration depth (δ). These subtleties could also be difficult to distinguish due to polydispersity of the radii or due to instrumental smearing. This occurs because this change in penetration does not represent a significant alteration of the whole structure. The scattering becomes more sensitive to this parameter when the particle size approaches the core radius. A definite difference in scattering signal is observed as the particle penetration depth is changed for complexes with a smaller core ($R_o=500 \text{ \AA}$) and larger surrounding particles ($R_p=200 \text{ \AA}$).

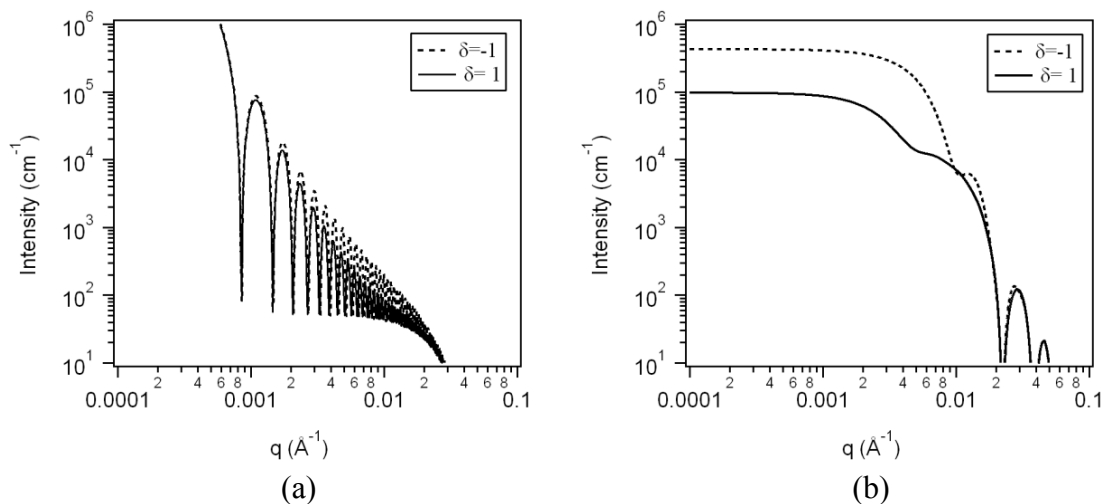


Figure 2.14. Calculated scattering of hexadecane in water emulsion with 50% SiO_2 covering the oil-water interface ($\chi=0.5$) where the excess scattering length densities used are $\Delta\rho_o=1.91\text{E-}6 \text{ \AA}^{-2}$, $\Delta\rho_p=9.44\text{E-}6 \text{ \AA}^{-2}$ and (a) $R_o=5000 \text{ \AA}$, $R_p=100 \text{ \AA}$, $\phi_o=0.05$ and $\phi_p^T=0.002$ and (b) $R_o=500 \text{ \AA}$, $R_p=200 \text{ \AA}$, $\phi_o=0.05$ and $\phi_p^T=0.066$.

From the model, it is also determined that SAXS experiments will only be useful when there is a large difference in electron density between the particles and the fluid phases. Therefore, SAXS experiments can be effectively utilized for the analysis of emulsions that are formed in the presence of metal nanoparticles. However, emulsions stabilized by oxide nanoparticles (e.g. SiO_2) may not result in sufficient x-ray scattering contrast to accurately determine all of the structural parameters.

A comparison of the Pickering Model to the calculated scattering intensity of Pickering emulsions using the Debye Model shows good agreement. Figure 2.15 shows scattering curves that are calculated for an emulsion with $1\ \mu\text{m}$ contrast-matched oil droplets and several particle loadings. The dashed lines are the Debye Model and the solid lines are the Pickering model.

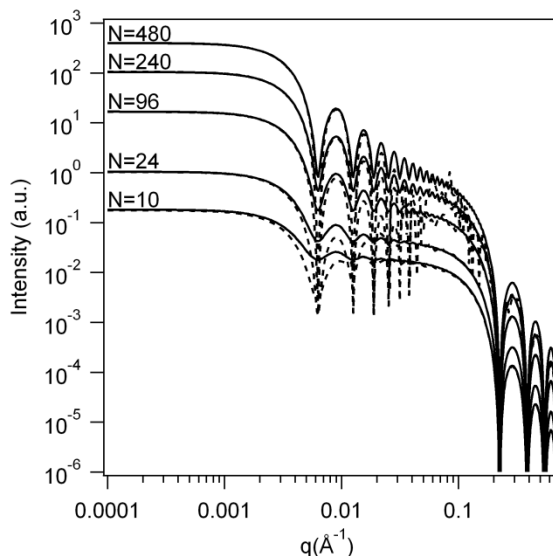


Figure 2.15 Comparison of predicted scattering from Debye Model (dashed) and Pickering Model (solid) for an emulsion with contrast-matched oil and varying numbers of equally-spaced adsorbed particles. Parameters used for the modeling are $R_o=500\ \text{\AA}$, $R_p=20\ \text{\AA}$, $\Delta\rho_o=0$, $\Delta\rho_p=2.55\text{E-}6\ \text{\AA}^{-2}$, $\delta=0$.

2.4 Summary

Small angle scattering is an extremely useful technique for analyzing particle size, shape and structure directly in the dispersed phase. Through careful material selection along with isotopic contrast matching, it is possible to highlight various components of a sample. Using this in combination with the models that are derived in this chapter, it is possible to determine quantitative structural information. Both small angle x-ray and neutron scattering will be used in this thesis to determine the arrangement of particles as stable clusters in water and organized at emulsion droplet interfaces.

Chapter 3: Scalable Synthesis of Self-Assembling Nanoparticle Clusters Based on Controlled Steric Interactions

A simple method is presented for the synthesis of amphiphilic gold nanoparticles that self-assemble into clusters of controllable size and structure. The technique is based on the control of particle clustering through sequential functionalization of the surface with thiol-terminated polyethylene glycol (PEG-thiol) to sterically stabilize particles in water and short alkane-thiols rendering the particles amphiphilic. The “nanoparticle surfactants” are surface active and form rafts at the air-water interface and stable nanoparticle clusters in dispersion. It is also shown that the average structure and size of the clusters is directly and reproducibly controlled by the concentration of PEG-thiol chains that are linked to the particle surface. Shifts in the plasmon resonance peak of the gold nanoparticles also demonstrate that this new method for self-assembly can be effectively used to tune optical properties with great precision. With this new approach, we show that it is possible to fabricate amphiphilic nanoparticles and clusters with controllable structure by taking advantage of the steric stabilization that is imparted by surface bound polymers. The work presented in this chapter has been previously published as a manuscript in *Soft Matter*.⁶⁹

Larson-Smith, K.; Pozzo, D. C., Scalable synthesis of self-assembling nanoparticle clusters based on controlled steric interactions. *Soft Matter* **2011**, 7, (11), 5339-5347. - Reproduced by permission of the Royal Society of Chemistry.

3.1 Background: Self-Assembling Particles

Self-assembling particles can form clusters with highly complex shapes and functionalities that could enable the engineering of new materials with tunable properties (e.g. optical and electrical).^{41, 44, 70-73} Several approaches are used to engineer self-

assembled structures from particles and nanoparticles.³⁵⁻⁴² However, there are limitations to each of these approaches such as high cost and low particle yield. Here we demonstrate a new, simple and inexpensive method to assemble gold (or coinage metal) nanoparticles into clusters by controlling the steric interactions that originate from surface-grafted polymers.

Steric repulsion, originating from adsorbed or grafted polymers, is a frequently used method to stabilize colloidal dispersions. For effective stabilization, the particle surface is usually saturated with the adsorbing polymer so that a 'hairy particle' is created. The repulsion between polymer chains of two approaching colloidal particles alters their interaction potential and prevents the aggregation that would usually occur due to van der Waals or other attractive forces. Here we demonstrate that steric interactions can also be used to effectively manipulate and control the self-organization of nanoparticles into stable clusters or 'colloidal molecules'. For this, we develop a novel one-pot technique for producing amphiphilic nanoparticles that are also able to form stable clusters through a spontaneous self-assembly process that is mediated by local steric interactions. Key to this method is the use of nanoparticle surfaces that are only partially coated with polymer so that the balance between colloidal attraction and steric repulsion is carefully manipulated. This synthetic method crudely emulates the local steric interactions that occur in natural proteins when they contain intrinsically unfolded peptide appendages.⁷⁴ Furthermore, the great advantage of this bulk-phase self-assembly technique lies in its simplicity, versatility, scalability, low-cost and the possibility of obtaining a high level of structural control. This technique only uses commercially available components and it is potentially applicable to a variety of particles and surface functionalities.

The new technique is based on controlling repulsive steric interactions between gold nanoparticles through sequential labeling of the surface with hydrophilic polymers and small hydrophobic thiol molecules. A schematic of the proposed process is shown in Figure 3.1. An amphiphilic surface coating is created without the use of amphiphilic molecules by taking advantage of the steric repulsion that is experienced by all surface-bound polymers.⁴⁶ In the new method, citrate-stabilized gold nanoparticles are functionalized with long poly-ethylene glycol (PEG) chains having a single thiol group at one chain end. The PEG-thiol chains maintain dispersion stability in water and also control the extent of particle clustering and self-assembly through local steric forces. After PEG-thiol conjugation, the nanoparticle surface is rendered amphiphilic by subsequently functionalizing the dispersion with an excess of small molecule alkane-thiols. Because of the smaller size, the alkane-thiol can penetrate through the PEG layer and effectively label the remaining gold surface that has not been coated by polymer chains. This creates an amphiphilic particle surface with a long hydrophilic corona (PEG) that shields a short hydrophobic core (alkane). This labeling process spontaneously induces controlled clustering of the particles in the dispersion. By altering the concentration of PEG chains on the particle surface, we demonstrate that it is possible to engineer local steric forces and to control the number of particles in the clusters and their geometry. In addition, previous work has also shown that mixed self-assembled monolayers (SAMs) on gold often separate into ‘patches’ that are enriched with one type of thiol.⁷⁵⁻⁷⁹ Research groups continue to study the physical mechanisms that can lead to segregation in nanoparticle and macroscopic surfaces using simulations and experiments.^{80, 81} Based on these findings, it is also possible that PEG and alkane-thiol

ligands will segregate and form domains or ‘patches’ on the surface of the nanoparticles to affect cluster formation. Although the physical mechanism leading to clustering is still being investigated, this report demonstrates that this new approach results in spontaneous formation of ‘colloidal molecules’ at concentrations that now make them accessible for use in a variety of applications.

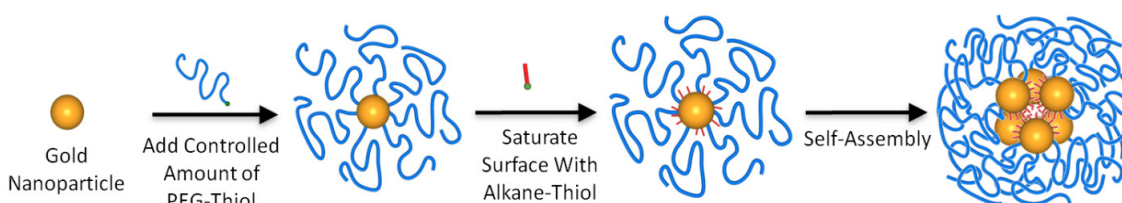


Figure 3.1. Schematic representation of the new method for surface functionalization and assembly of gold nanoparticles. PEG-thiol chains sterically control clustering while the octane-thiol induces aggregation due to hydrophobic attraction.

3.2 Experimental Methods

Gold chloride hydrate, sodium citrate, butane-thiol, octane-thiol and dodecane-thiol are purchased from Sigma Aldrich (St. Louis, MO) and used as received. Thiol-terminated Poly(ethylene glycol) methyl ether (10 kDa) is obtained from Polymer Source (Dorval, Quebec Canada). Colloidal gold with 12 nm diameter particles are prepared by the citrate reduction method with a protocol that is described by Frens.⁸² This protocol produces relatively monodisperse gold particles at a concentration of 0.05 wt% in an aqueous buffer. The nanoparticles are then functionalized directly utilizing thiol-gold covalent bonding chemistry without the need for any intermediate treatment or purification.^{34, 83-85}

Gold nanoparticles are first functionalized by addition of PEG-thiol at a polymer dose corresponding to a specific surface concentration in the range of 0.7-19.5 PEG chains/nm² Au. The actual amount of PEG-thiol that binds to the surface is expected to be significantly lower as it depends on factors such as the activity of the PEG-thiol, the kinetics of binding and the saturation of the gold surface. The polymer doses over which we observe systematic changes in the data are significantly larger than what is typically needed to saturate the surfaces using grafting approaches (~ 1 chains/nm² Au).^{83, 86} Clearly, a large fraction of the added PEG-thiol is unable to bind to the gold surface. To estimate the bound polymer fraction, a representative sampling of PEG-functionalized gold dispersions are dialyzed to remove the unbound PEG-thiol. Subsequent Thermo Gravimetric Analysis (TGA) on the dried and dialyzed samples indicates that only $12.1 \pm 1.2\%$ of the initial dose PEG-thiol is able to adsorb onto the gold particles at the conditions used in this work. All reported concentrations in this report correspond to a PEG-dose value that has been scaled according to the PEG-thiol activity determined by TGA. After addition of PEG-thiol, the dispersions are equilibrated for four days to allow the chains to fully bind to the particle surface. After labeling with PEG-thiol, the particles remain dispersed and no clustering occurs. An alkane-thiol (e.g. octane-thiol) is then added at a large excess concentration (500 octane molecules/nm² Au) that is enough to bind with all of the available gold sites and to reach surface saturation.

In our method, the PEG-thiol chains are critical components to sterically prevent the uncontrolled aggregation of the nanoparticles and subsequent sedimentation. The lateral steric interaction of the PEG-thiol is also essential to control the resulting shape and morphology of the clusters. The difference in size between the hydrophilic PEG-thiol

(large) and the hydrophobic alkane-thiols (small) effectively creates an amphiphilic surface coating that is similar to that which can be created from surface-bound amphiphilic block copolymers. However, the new method does not require any other amphiphilic molecules or specialized chemistry to generate the amphiphilic particles and stable clusters. After one day, the formation of stable clusters is evidenced by a color change in the dispersions. The clusters do not aggregate any further and are stable for more than five months. Interestingly, in addition to forming clusters, the functionalized nanoparticles are also found to adsorb and form rafts at the oil-water interface. A schematic of the process is shown in Figure 3.1. Clusters with concentrations below 0.1 PEG chains/nm² Au are not stable because the available PEG-thiol is not sufficient to fully stabilize the clusters and the particles aggregate and sediment very quickly. This critical concentration is found to shift depending on the length of the PEG-thiol chain. Similarly, the order of ligand addition, PEG-thiol followed by alkane-thiol, is critical in this procedure. When the alkane-thiol is added first, or simultaneously with the PEG-thiol, the particles aggregate and sediment because the necessary steric stabilization from the PEG has not been established.

Dynamic Light Scattering is performed using a Malvern Zetasizer Nano ZS with a 633 nm wavelength. UV-Vis spectroscopy is carried out using a Thermo Scientific Evolution 300 system in the visible range (300-800 nm). Dilute 0.005 wt% gold dispersions in water are used in both techniques in order to allow for sufficient light penetration into the samples.

Lyophilized clusters are also examined with a FEI Tecnai G2 F20 Transmission Electron Microscope (TEM) operating at 200 kV. Clusters are deposited on a copper

TEM grid with a Formvar support film by placing a drop of 0.005 wt% gold dispersion on the grid followed by freeze-drying. The freeze-drying process is used to avoid aggregation due to capillary forces experienced during drying of liquid samples.

Small Angle X-ray Scattering (SAXS) is used to examine the structure of the stable nanoparticle clusters. SAXS experiments are performed in an Anton Paar SAXSess instrument with a line-collimation system using a Cu-K α source with a wavelength of 1.54 Å. SAXS experiments are performed on 0.03 wt% gold dispersions in water. The difference in scattering length density (SLD) of gold and water ($\Delta\rho_{\text{Au-H}_2\text{O}}=1.14\text{E-}4 \text{ \AA}^{-2}$) is much greater than PEG and water ($\Delta\rho_{\text{PEG-H}_2\text{O}}=1.80\text{E-}7 \text{ \AA}^{-2}$), so the gold particles dominate the scattering.

3.3 Results and Discussion

3.3.1 Cluster Formation and Characterization

Figure 3.2 shows the results from UV-Vis absorbance measurements for bare gold particles and for stable clusters. The spectrum of the original (unlabeled) gold particles contains the characteristic broad peak at 520 nm that forms due to the surface plasmon resonance.¹⁰ For labeled particles that have high surface concentrations of PEG-thiol, the solutions show similar spectra to the bare gold but the surface plasmon peak is shifted modestly to 523 nm. This slight shift is expected from the change of the local refractive index that results from the attachment of the PEG-thiol chains to the surface. The plasmon resonance peaks of PEG-functionalized gold particles without any alkane-thiol are also presented in Figure 2b. For these samples, the peak is independent of the PEG-thiol dose at high concentrations. At lower concentrations there is a steady decrease of

the peak position to the value of the bare particles (520 nm). This is fully expected for a decreasing concentration of PEG-thiol at the surface and the corresponding changes in refractive index around the gold particles.

The situation is very different when the alkane-thiol molecules of variable length are introduced to the PEG-coated dispersions. For all samples, when the concentration of PEG-thiol is systematically reduced, the plasmon peak shifts steadily to higher wavelengths indicating the formation of gold clusters. The shift in absorbance is indicative of an increase in size that is due to the fact that more particles are able to participate in clustering because the local steric repulsion is systematically reduced. Furthermore, the absorbance peak shift is enhanced when shorter alkane-thiols, such as butane-thiol, are used to induce clustering. For larger alkane-thiols, such as dodecane-thiol, the shift in the plasmon resonance peak is less pronounced. The dependence of the peak shift for the different alkane-thiols suggests that the length of the thiol spacer accurately controls the inter-particle spacing. The controllable and reproducible changes in the optical properties in this model system demonstrate the potential of this new method for tuning the structure and properties of colloids by driving self-assembly.

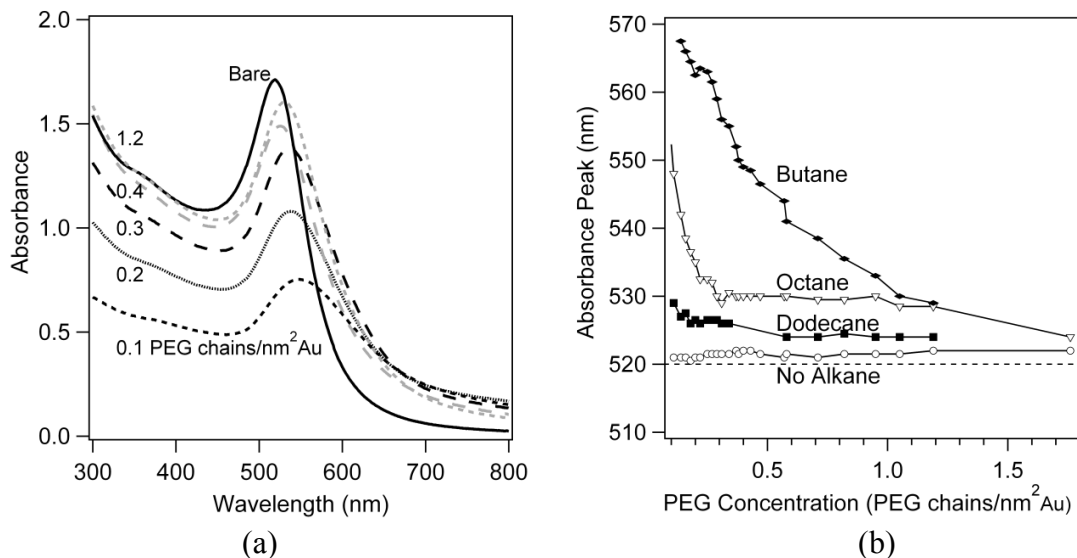


Figure 3.2. a) UV-Vis absorption spectra of octane-thiol functionalized clusters in water. b) PEG concentration dependence of absorbance peak, where the dashed line is the absorbance of bare gold particles and particles functionalized by no alkane-thiol, dodecane-thiol, octane-thiol and butane-thiol are represented by open circles, close squares, open triangles and closed diamonds respectively.

UV-Vis spectroscopy is also used to track the cluster formation over time. At the initial time of alkane-thiol addition, the spectrum looks identical to that of PEG-functionalized gold particles. The absorbance peak at 522 nm decreases as the alkane-thiol penetrates the PEG corona and bonds to the gold. The shift of the peak to higher wavelengths occurs as the particles cluster. The spectrum is fully developed after 24 hours, indicating the clusters have reached their final structure. Figure 3.3 gives the UV-Vis absorbance spectra of 0.6 PEG chain/nm² Au functionalized particles over time after the addition of octane-thiol.

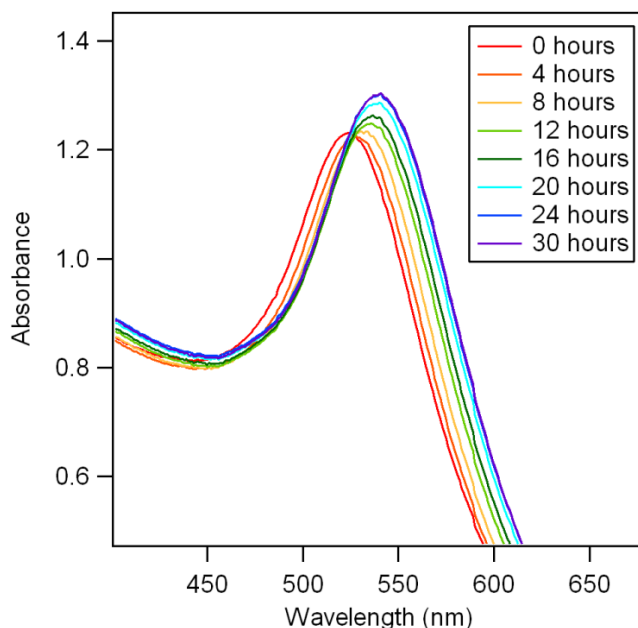


Figure 3.3. UV-Vis absorption spectra of 0.6 PEG chains/nm²Au particles functionalized with octane-thiol at time 0 hours.

Dynamic Light Scattering (DLS) is also used to characterize the distribution of hydrodynamic radii, R_h , of PEG-cluster complexes before and after octane-thiol addition (Figure 3.4). At high values of PEG-thiol surface concentration, the octane-thiol functionalized cluster size distributions are very narrow. However, they tend to significantly broaden as larger clusters begin to form (lower PEG-thiol concentration). For the lowest PEG-thiol concentration, the distribution is clearly bimodal suggesting a coexistence of small and very large clusters. Figure 3.5 shows the variation in the mean hydrodynamic size as a function of PEG-thiol concentration for samples before and after the addition of alkane-thiol. As expected, the mean hydrodynamic radius of bare gold (~6.0 nm) shifts to ~20 nm after functionalization with PEG-thiol but before alkane-thiol addition. This suggests that the extension of the PEG layers from the particle surface is

on the order of ~ 14 nm. This also implies that the polymers are extending out into the solvent and are not collapsed on the gold surface.

As expected, Figure 3.5 also shows that the hydrodynamic size of the PEG-coated particles decreases with decreasing PEG-thiol concentration. A small change is expected because even a few bound polymer chains will still significantly alter the hydrodynamic radius due to the added hydrodynamic drag.⁸¹ In sharp contrast, after the addition of octane-thiol, R_h increases steadily as the PEG concentration decreases because more particles are added to the clusters when the repulsive interactions of the PEG layers are reduced. It should be noted that the hydrodynamic radius of the clusters obtained from DLS is also strongly dependent on the conformation of the PEG-thiol chains because the polymer corona is comparable in size to the gold particles. Additionally, at low PEG-thiol concentrations there are opposite effects influencing the diffusion coefficient of the clusters and the hydrodynamic size, R_h . As the PEG-thiol concentration decreases, we find that the cluster size (i.e. the number of gold particles) increases steadily as demonstrated by TEM and SAXS experiments. Logically, adding more particles to the clusters is expected to increase the hydrodynamic radius. However, the lower PEG-thiol concentration also creates a thinner polymer corona on all particles and this will reduce the hydrodynamic drag of the solvent on the particles and clusters. Finally, particle rearrangement occurring within the clusters can further complicate this size dependence.

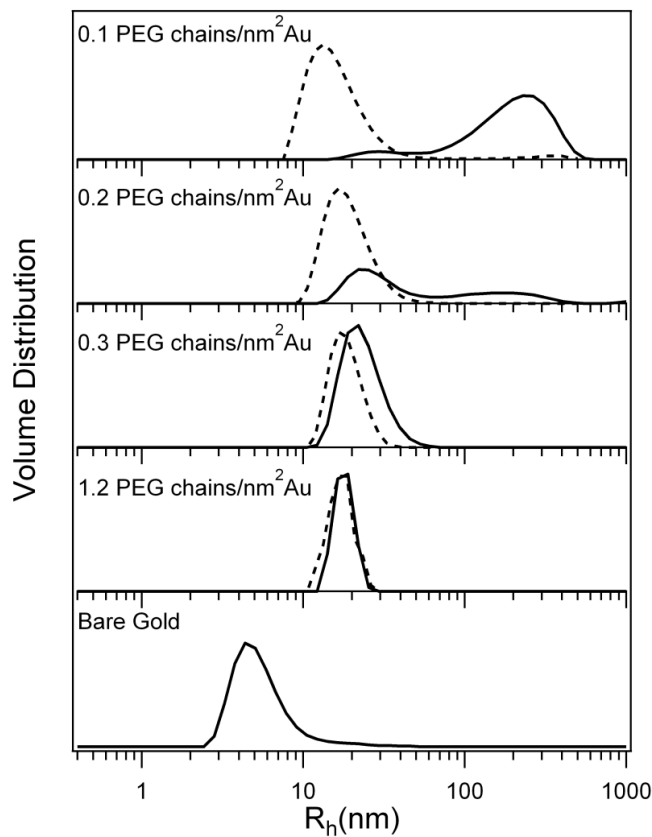


Figure 3.4. Volume distribution of hydrodynamic radii of PEG coated particles in water before (dotted) and after (solid) octane-thiol functionalization obtained from Dynamic Light Scattering.

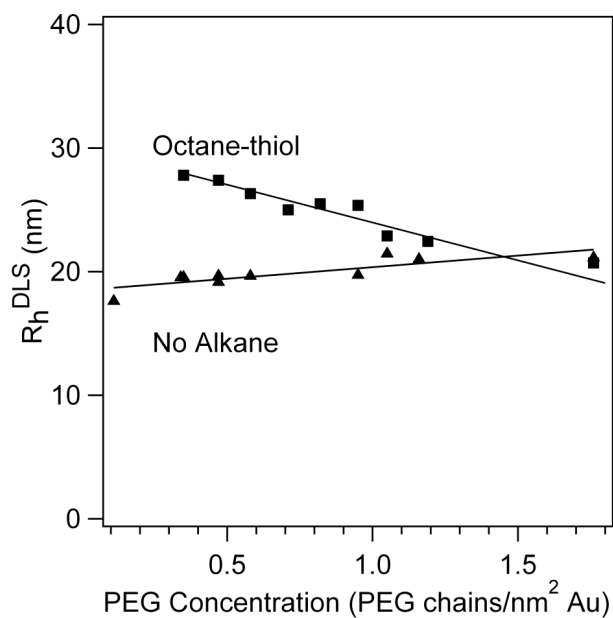


Figure 3.5. Hydrodynamic radii of PEG functionalized gold before and after octane-thiol addition. Lines are only added to guide the eye.

In order to characterize the structures of the nanoparticle clusters we also perform transmission electron microscopy (TEM) on dried dispersions. Figure 3.6 shows representative electron micrographs of lyophilized samples. The samples are freeze-dried to minimize interfacial clustering effects that can occur during drying of liquid dispersions. Unfortunately, the drying process of TEM can also cause changes to the cluster structures due to the collapse of the polymer layer. Nevertheless, TEM images are still useful to directly quantify the number of particles in each cluster and also to highlight some of the geometries that are obtained with this self-assembly method. Electron microscopy confirms that there is a mixture of conformations coexisting in the samples rather than a single cluster type. Histograms are created to quantify and compare the number of particles per cluster for each analyzed sample. As expected, the average number of particles per cluster is found to increase with decreasing PEG-thiol concentration.

Figure 3.6 shows typical examples of PEG-octane functionalized cluster structures that are observed with TEM. Only representative micrographs are shown here but tens of other TEM images are analyzed to demonstrate the formation of clusters in all samples. Depending on the PEG-thiol dose, singlets, doublets, triplets and larger clusters are observed. For clusters with larger number of particles, we observe that many of the structures have the same thermodynamically stable geometries that are observed by Manoharan and coworkers for micrometer-sized colloids.³⁵ Some of the clusters in the electron micrographs have a tetrahedral, trigonal dipyramid or octahedral geometry for four, five and six particles, respectively. However, many of the clusters collapse during the drying process due to the removal of solvent leading to shrinking of the PEG-thiol

layers and also modification of the colloidal interactions that hold the structures together in the dispersions. The TEM substrate could also cause changes to the cluster structures. This motivates the use of scattering techniques to study the particle clusters directly in the dispersed state. Finally, another important observation from the electron micrographs is that the particle spacing in the clusters is quite small, and particles appear to be touching. This further suggests that it is unlikely to have PEG-thiol chains located between particles because of the reduced volume that is available. Such a PEG layer would likely result in significantly larger separation distances between neighboring gold particles.

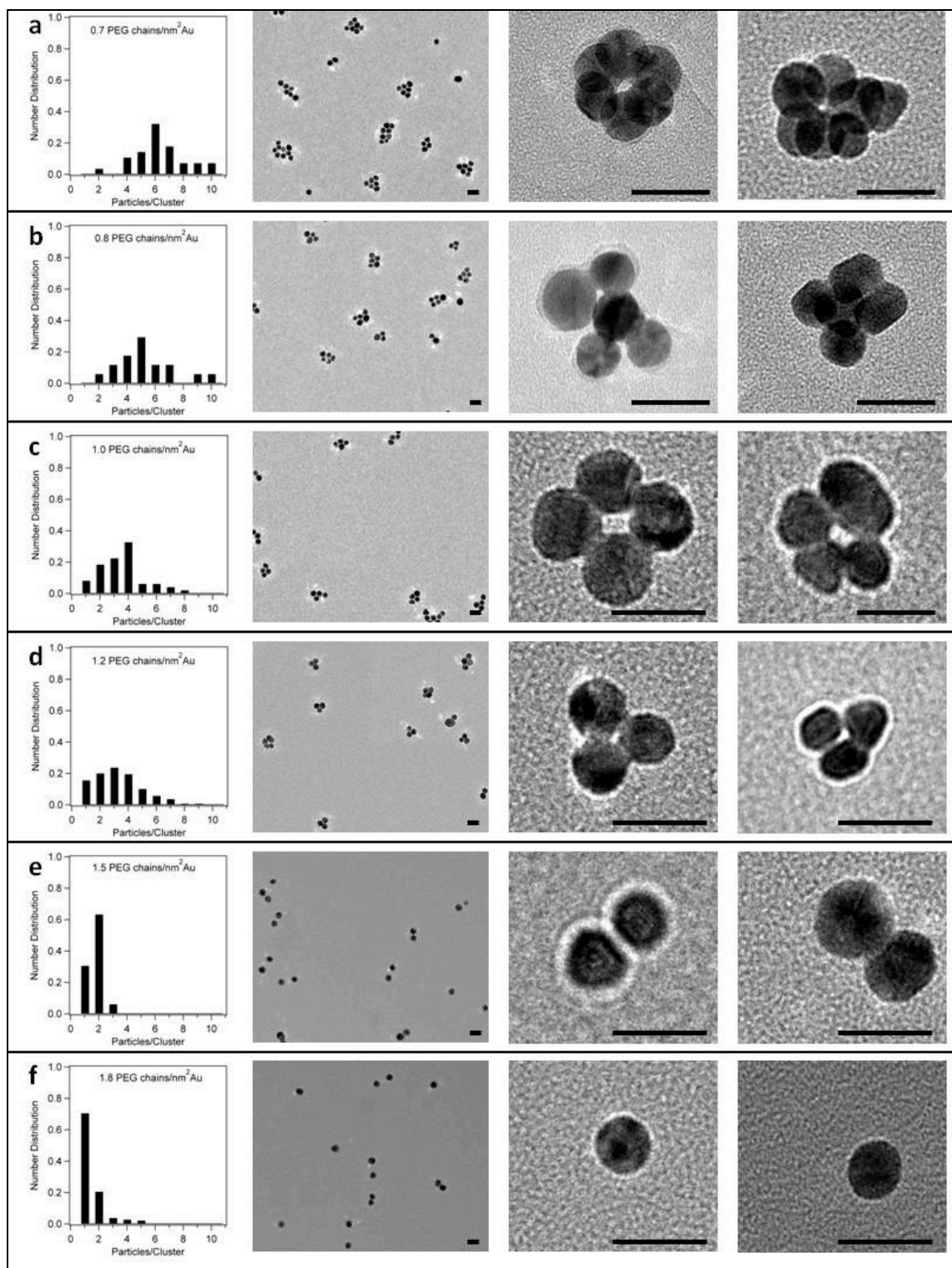


Figure 3.6. Histograms of the number of particles per cluster for (a) 0.7 PEG chains/nm² Au, (b) 0.8 PEG chains/nm² Au, (c) 1.0 PEG chains/nm² Au, (d) 1.2 PEG chains/nm² Au, (e) 1.5 PEG chains/nm² Au and (f) 1.8 PEG chains/nm² Au. Examples of clusters observed with Transmission Electron Microscopy for each sample are to the right (scale bar = 20 nm).

Small-Angle X-ray Scattering (SAXS) is used to probe the cluster structures directly in the dispersed state. Due to the large scattering contrast of gold relative to PEG, the scattering contribution in SAXS originates primarily from the shape and arrangement of the gold nanoparticles. Figure 3.7 shows the systematic changes that occur in the scattering curves as the surface PEG concentration increases. At high values of q , all of the data collapse, because the intra-particle correlations related to the spherical particle shape (form factor) dominate the scattering. In contrast, at medium and low values of q , there are large and systematic variations in the scattering profiles with small changes to the surface composition. At 1.8 PEG chains/nm² the curve is again identical to that of bare gold suggesting that no clusters are formed when the concentration of PEG-thiol is sufficiently large. When PEG-thiol fully saturates the gold surface, the polymer chains sterically prevent the gold particles from clustering. As the PEG-thiol concentration is reduced, clusters begin to form as indicated by changes in the shape of the scattering profile and by systematic increases in the scattering intensity at small angles. This indicates that clusters containing larger numbers of particles are being formed. At low PEG-thiol concentrations, the formation of clusters is evident by the development of a dip at medium q and by a shift of the Guinier plateau towards lower values of q .

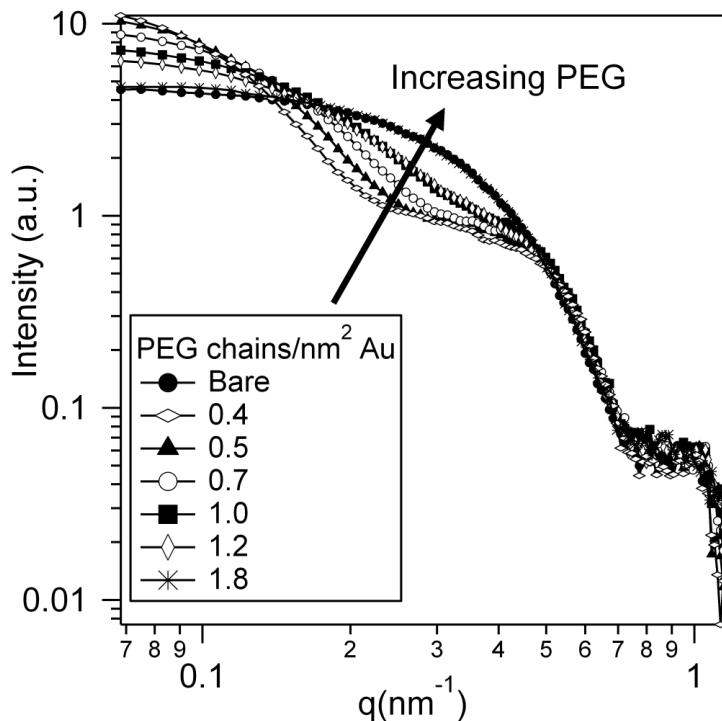


Figure 3.7. Slit-smear SAXS profiles of clusters at varying PEG concentrations. The arrow indicates increasing PEG concentration.

In order to extract quantitative information from the SAXS profiles we compare the data with simple geometrical models for particle clusters. The scattering models are derived from the fundamental Debye Equation and from the equilibrium cluster configurations that are reported by Manoharan and coworkers in their seminal work using micrometer size particles.^{35, 87} The details of the calculations and the full equations for all of the particle cluster configurations are located in Chapter 2. The resulting curve for each type of equilibrium cluster configuration (from Manoharan) is plotted in Figure 3.8 assuming a particle radius of 6 nm and a constant nearest neighbor distance of 13 nm.

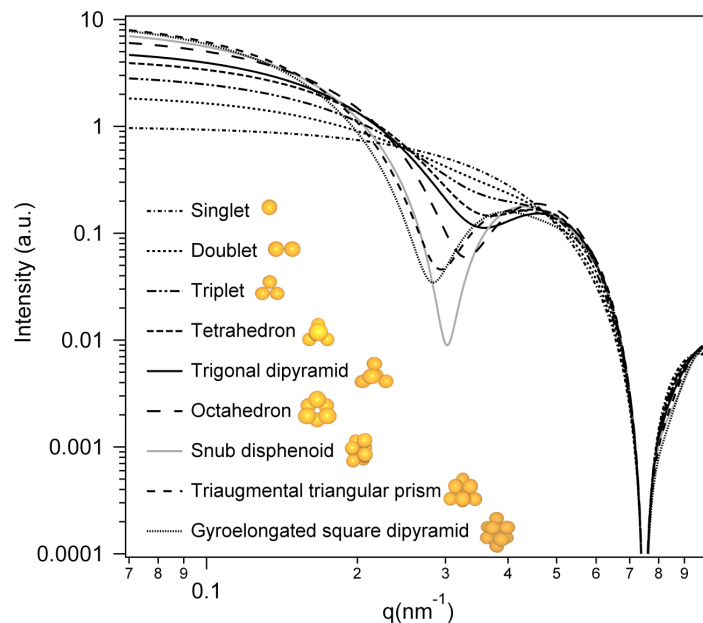


Figure 3.8. Calculated scattering profiles for expected particle geometries using the Debye Model.

Figure 3.9 contains examples of the predicted scattering curves based on the Debye model compared with the experimental SAXS curves after accounting for instrumental smearing.⁵² A predicted curve is created for each sample by weighting the scattering contribution of the equilibrium polyhedral configurations (Figure 3.8) with the corresponding abundance in the sample as obtained from histograms generated from TEM data. The agreement between the predicted and measured curves is excellent even without resorting to data fitting. At the highest concentration of PEG-thiol (1.8 PEG chains/nm² Au) the data is approximated well with the model for simple isolated spheres.⁶⁰ The only region where there is some disagreement between the data and the predictions is at high values of q . This is primarily caused by the assumption of a monodisperse particle size when it is clear in Figure 3.6 that some polydispersity in the primary gold particles is present. Also, the noise level in this region is greater due to the significant contribution of background solvent scattering.

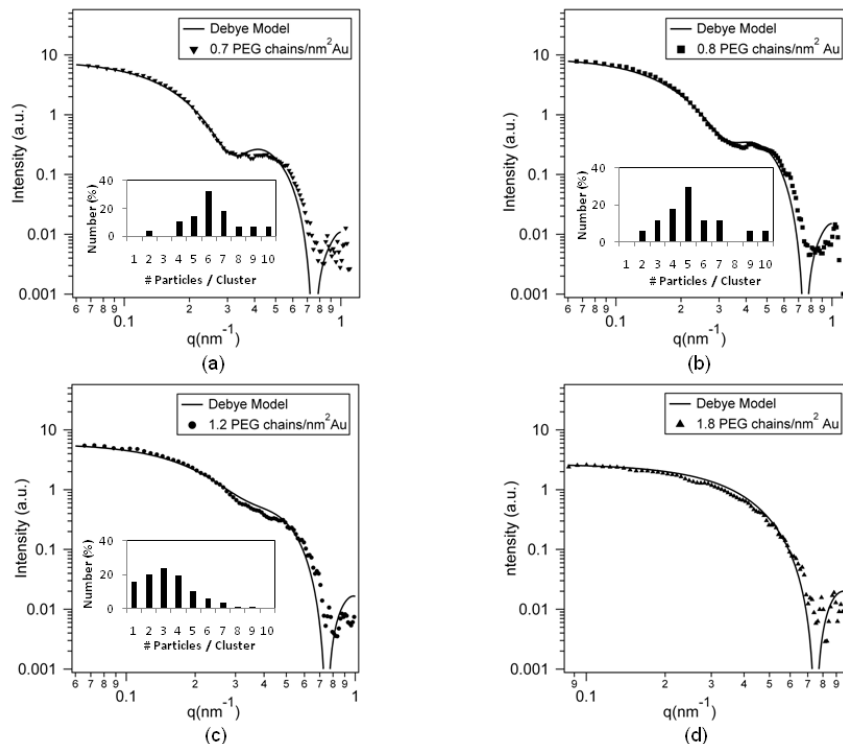


Figure 3.9. SAXS data for (a) 0.7 PEG chains/nm² Au, (b) 0.8 PEG chains/nm² Au, (c) 1.2 PEG chains/nm² Au and (d) 1.8 PEG chains/nm² Au. The straight lines represent scattering predictions (not fits) based on a weighted Debye model using the histograms obtained from TEM (inset graphs) and the cluster geometries predicted by Manorahan et al.³⁵

Supporting calculations are also performed to assess the sensitivity of the SAXS models to small changes in the distribution of the cluster sizes. Figure 3.10 shows the sensitivity of the scattering data to the weighting of the distribution. Figure 3.10a shows the calculated SAXS predictions for Gaussian distributions that are centered on various mean cluster sizes with a variance of one. This calculation shows that the SAXS data are quite sensitive to the average number of particles per cluster. However, Figure 3.10b shows that SAXS is less sensitive to the broadness of the distribution. The primary disparity in scattering of cluster distributions with similar mean but different variance are observed in the dip at $q=0.35 \text{ nm}^{-1}$, which will also be affected by instrumental smearing.

In all of these calculations, the prediction obtained from the experimental TEM histograms shows the best agreement with the data.

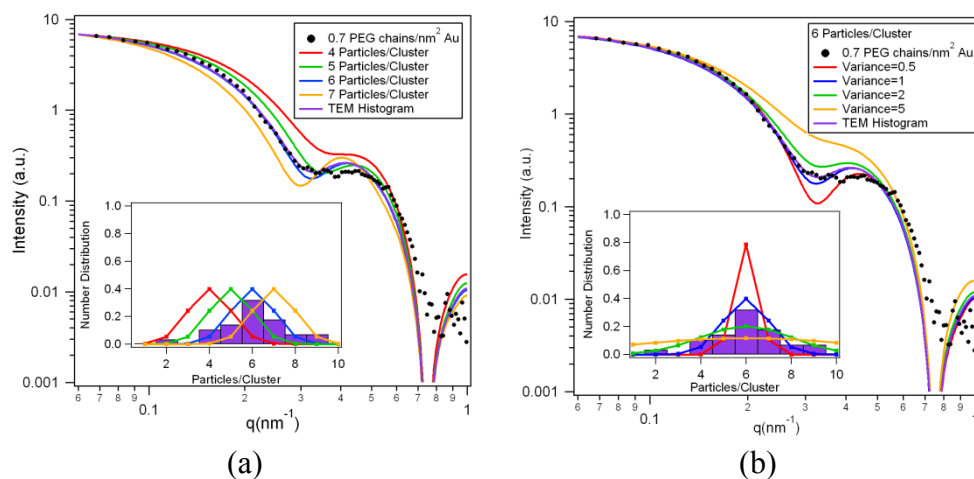


Figure 3.10. Modeled SAXS curves based on arbitrarily created Gaussian distributions to test the model sensitivity to (a) number of particles/cluster and (b) variance.

The radius of gyration, R_g , for each PEG-thiol concentration is also calculated from the Guinier regime of the scattering curves using Equation 3.1 and shown as a function of PEG concentration in Figure 3.11.⁸⁸

$$\ln[I(q)] = \ln[a_o] - \frac{R_g^2}{3} q^2 \quad (3.1)$$

This plot shows that R_g^{SAXS} of bare gold and 1.7 PEG chains/nm² Au are essentially equivalent because most of the scattering contributions originate from the gold particle core and there is no clustering at high PEG-thiol concentrations. As the PEG-thiol concentration decreases, the R_g^{SAXS} of the clusters grows systematically. R_g^{SAXS} could not be calculated for PEG-thiol concentrations below 0.5 chains/nm² because a scattering plateau is not reached at q_{min} of the instrument. This suggests that the average cluster size in this region is larger than the resolution of the instrument (~15 nm). The systematic

change in hydrodynamic radius found with DLS (R_h^{DLS}) is less pronounced because the PEG corona dominates the measurement and this is affected to a smaller extent by the number of particles in the cluster.

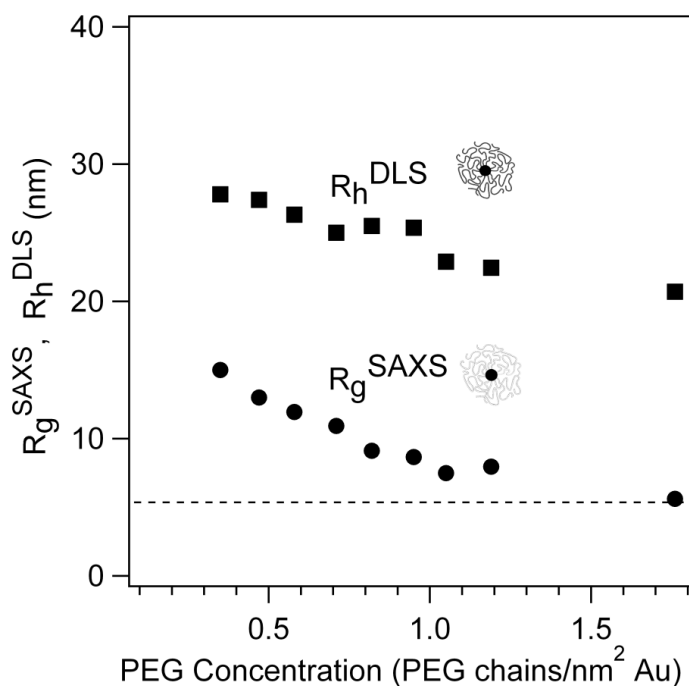


Figure 3.11. Radii of gyration and the average hydrodynamic radii of clusters measured using SAXS and DLS respectively. The dashed line indicates the R_g^{SAXS} of bare gold.

Scattering, spectroscopy and electron microscopy all suggest that PEG chains are not likely to be located in the small space between gold particles in the clusters. The models for the scattering profiles that match the SAXS data are calculated assuming a constant nearest neighbor distance of 13 nm. This corresponds to an assumed separation distance of 1 nm between particle surfaces to simulate the spacing induced by the alkane-thiol molecules between neighboring gold particles. Because of the large size of the polymer chains, the distance between particles should be significantly larger if PEG chains were also located in this region. The electron micrographs (TEM) also show nearly close-packed particles in the clusters. This further suggests that most of the PEG

chains likely reside on the out-facing sides of the particles in the clusters. UV-Vis spectroscopy provides additional evidence for this PEG conformation because the inter-particle spacing is found to be very sensitive to the alkane-thiol chain length (Figure 3.2b). The magnitude of the shifts in the plasmon resonance, to higher wavelengths, is observed to increase with decreasing alkane-thiol length (i.e. butane-thiol > octane-thiol > dodecane-thiol). This magnitude of sensitivity to changes in alkane-thiol length would not be expected if the bulky PEG chains were also located in the spaces between particles. While the exact mechanism for obtaining this conformation is still unknown, we believe that our data suggest that PEG-thiol chains are somehow segregated from the alkane-thiol layers on the gold surface.

3.3.2 Mechanism and Sensitivity to Environment

Many alternative mechanisms could also explain the formation of particle clusters in colloidal dispersions such as those studied here. For example, in the work of Stradner and colleagues, short-range attraction and long-range electrostatic repulsions are balanced to induce spontaneous clustering.⁵⁰ In their work, the attractive interactions of the globular protein lysozyme are enhanced by decreasing the sample temperature. Salt concentration also controls the electrostatic repulsion by decreasing the Debye screening length, so higher salt concentrations in this system can lead to cluster instability due to increased cluster-cluster interactions. The average number of particles in their clusters is demonstrated to change as a function of the environmental conditions (i.e. salt and temperature). Changes in temperature and salt were used to investigate this as a possible clustering effect in our system. In contrast to the work of Stradner, the clusters formed in

this study are found to be largely unaffected by changes in temperature (over 5-50 °C) as demonstrated with SAXS in Figure 3.12. Similarly, the ionic strength (0-50 mM NaCl) of the dispersed phase had no effect on the cluster structure as shown in Figure 3.13. Therefore, it is likely that these are kinetically arrested cluster structures under these conditions. We can conclude that charge is not a primary means of stabilization in this system.

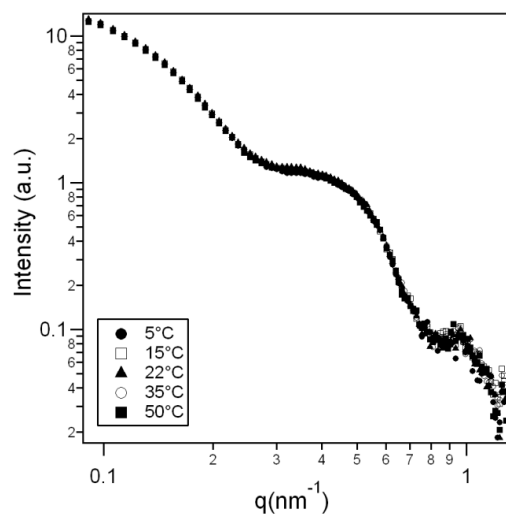


Figure 3.12. SAXS experimental curves for an octane functionalized 0.7 PEG chains/nm² Au clusters at varying temperature.

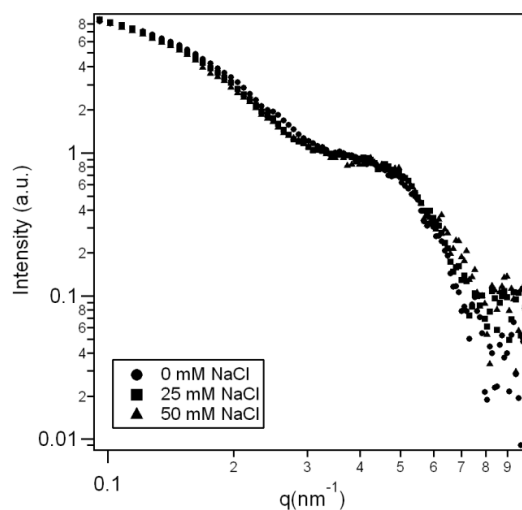


Figure 3.13. SAXS experimental curves for an octane functionalized 0.7 PEG chains/nm² Au clusters in dispersed phases of increasing NaCl concentration.

Depletion attraction, due to non-adsorbing polymer, can also compete with electrostatic repulsion and lead to stable cluster formation. Stradner also demonstrates the manipulation of this short-range attraction in the formation of equilibrium clusters.⁵⁰ Although this is a possible mechanism in other systems, depletion attraction due to unbound ‘free’ PEG-thiol is likely not a factor in our system due to the very low concentration of polymer that is used (< 0.1 wt%). Additionally, the clustering behavior in samples after extensive dialysis (i.e. removal of all free PEG-thiol) is found to be identical to the behavior of samples that still have unbound PEG-thiol in the solution (not dialyzed) as shown in Figure 3.14. Therefore, depletion attraction effects cannot explain the clustering in our system.

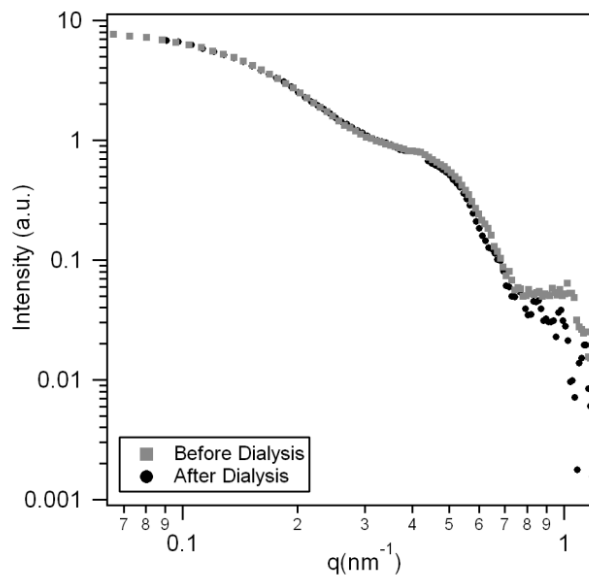


Figure 3.14. SAXS experimental curves for an octane functionalized 0.7 PEG chains/nm² Au clusters before and after the removal of unbound PEG.

Clusters from Janus particles with bipolar charge have also been shown to form spontaneously by Hong and coworkers. Furthermore, these cluster structures also have similar geometries to those observed by Manoharan.^{35, 41, 44} In that system, the clustering is induced by the electrostatic attraction of opposite surface charges located on opposite hemispheres of micrometer sized colloids. From TEM, UV-Vis and SAXS data, we also suspect that nanoparticles functionalized with PEG-thiol and alkane-thiol may also have segregated regions. Unfortunately, the nanometer size scale of the particles in our system makes the characterization of the exact surface composition a very challenging task. In addition to size, there are also other significant differences between these two particle cluster systems. Hong and co-workers use Janus particles with bipolar surface charges, so that ‘unlike’ sides of the hemispheres will come to contact due to electrostatic attraction. In our system, it is the ‘like’ parts of the particles that are attracted to each other due to hydrophobic attraction. In addition, the polymer chains in our system play an essential role by maintaining colloidal stability and by controlling the aggregation of additional particles via steric repulsion. Therefore, the clustering effect in our system is more akin to surfactants forming micelles. We show that the polymer is key to controlling the shape and the extent of aggregation due to controlled steric interactions. Altering the PEG-thiol concentration on the surface of the particles is analogous to changing the packing parameter for surfactants that form micelles. Therefore, we are presenting a novel mechanism for manipulating the cluster structure through controlled steric interactions of surface-bound polymers.

3.3.3 Expansion of Method to Other Systems

The amphiphilic particle synthesis method utilizing polymer steric hindrance can also be expanded to self-assemble other particle systems. The approach is most easily adaptable to other metallic nanoparticles that also covalently bond with thiol molecules. Silver nanoparticles ($r = 7.5$) are shown to form clusters when functionalized with dose PEG-thiol concentrations in the range of 0.5-5 chains/nm²Ag and octane-thiol. Figure 3.15a shows the hydrodynamic radii of PEG-functionalized silver particles without alkane-thiol increases with PEG-thiol concentration as determined by DLS. Conversely, the hydrodynamic size of octane-thiol functionalized particle increases as the PEG-thiol concentration is reduced because larger clusters are forming. This trend is identical to the one observed for gold particles. Similarly, SAXS also indicates larger clusters are forming at low PEG-thiol concentrations. Unfortunately, the particles used for this synthesis were polydisperse making the data difficult to quantitatively interpret. Still, Figure 3.15b shows that particles with lower PEG-thiol concentrations have more dramatic changes in the scattering curves compared to bare silver due to the inter-particle correlations. These preliminary data indicate that the general approach of using lateral steric hindrance to control particle clustering can be expanded to other particle materials.

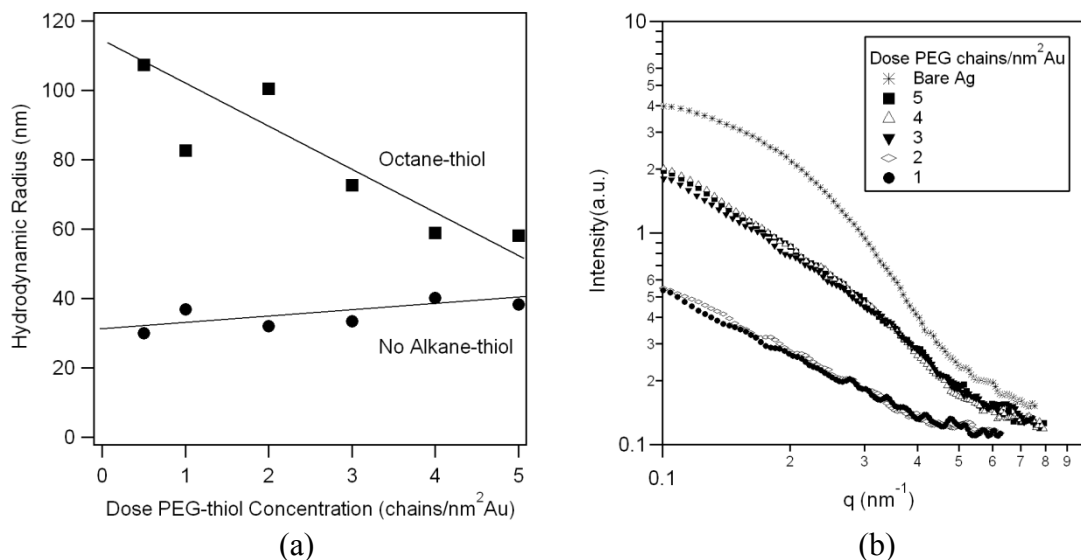


Figure 3.15 a) Hydrodynamic radii of PEG-functionalized silver before and after octane-thiol addition. Lines are only added to guide the eye. b) Slit-smear SAXS profiles of clusters at varying PEG-thiol concentrations.

The synthesis approach can also be modified to make clusters with mixed particle types and sizes. In one example, large gold nanoparticles were decorated with smaller gold particles to form a ‘raspberry’ structure. Here, 12 nm diameter gold particles were functionalized with a dose PEG-thiol concentration of 7.5 chains/nm² Au. The PEG-functionalized particles were then mixed directly with large bare gold particles ($r = 23$ nm) at a ratio of 84 small particles for each large particle. This ratio corresponds to enough small particles to be close-packed on the surface of the large particles. The particles were then clustered by octane-thiol functionalization. A representative TEM micrograph is shown in Figure 3.16. While it is clear that the small particles do not completely cover the large particle, we still see a structure that is a composite of the two particles. Much more optimization is needed to control the exact cluster structures. Still, this result shows it is possible to further expand this technique to mixed systems.

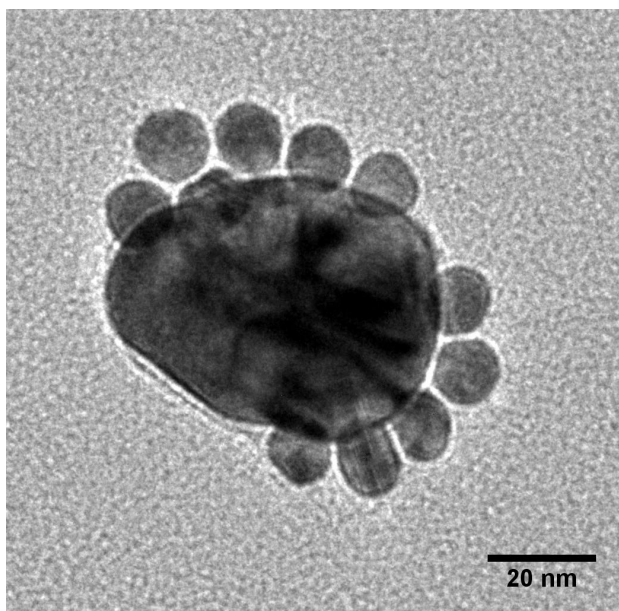


Figure 3.16 Representative TEM micrograph of a characteristic gold ‘raspberry’ composite particle.

3.4 Summary

The new technique for forming particle clusters described in this chapter is based on structural control through tuning of the steric interactions in amphiphilic particles. The lateral steric hindrance of the bulky PEG-thiol chains limits particle aggregation and also manipulates the structure of the clusters. Subsequent functionalization of the particles with short hydrophobic alkane-thiol chains renders them amphiphilic and induces stable cluster formation. The concentration of PEG-thiol on the surface is shown to effectively control the cluster size and to affect the structural arrangement. The structural analysis of the clusters shows that this control is based on balancing the attraction induced by the hydrophobic alkane-thiol layers with the steric repulsion of the long polymeric chains. Scattering and stability assessment also indicates that there is a lower limit to the concentration of PEG-thiol that is needed to sterically stabilize the particle clusters in aqueous dispersions. Clusters with small numbers of particles form spontaneously,

systematically and reproducibly at higher PEG-thiol concentrations. Nevertheless, there is significant polydispersity of the clusters that warrants further investigation. Clusters containing large numbers of particles ($N \gg 6$) are also formed at low PEG-thiol surface concentrations but their stability against sedimentation is lower and their structure is difficult to quantify from scattering alone.

The new approach for creating sterically stabilized amphiphilic particles offers great promise for the development of a variety of stable self-assembling clusters. It has been shown that the clusters are stable in dispersion and are not susceptible to further aggregation with time. Furthermore, we show that the structure of the clusters can be effectively tuned through variation of the surface composition. Scattering experiments and TEM suggest cluster structures that are in agreement with the results of Manoharan and coworkers but in the nanometer scale.³⁵ We believe that the simplicity of this novel method for creating amphiphilic particles will allow bottom-up self-assembly strategies to be more broadly adopted by the general scientific community.

Chapter 4: Competitive Adsorption of Thiolated Polyethylene Glycol and Alkane-thiols on Gold Nanoparticles

The surface concentration and conformation of thiol terminated polyethylene glycol (PEG) on gold nanoparticles are studied after co-adsorption of alkane-thiols. Thermogravimetric analysis (TGA) indicates alkane-thiol ligands will competitively adsorb on gold surfaces of nanoparticles and the extent of PEG-thiol replacement depends on the specific length of the alkane-thiol. The extension of the polymer is also affected by the length and packing density of the alkane-thiol. Dynamic light scattering (DLS) shows that the hydrodynamic size of coated particles has an intermediate maximum for the adsorption of octane-thiol, which also forms the most densely packed alkane-thiol monolayer. These two factors greatly impact the geometry and the formation of clusters by nanoparticle surfactants. Small angle x-ray scattering (SAXS) shows that the largest clusters are formed when particles have a low PEG-thiol surface concentration and an extended PEG conformation. The work presented in this chapter has been submitted for publication as a regular article in *Langmuir* entitled “Competitive Adsorption of Thiolated Polyethylene Glycol and Alkane-thiols on Gold Nanoparticles”. Reproduced with permission from *Langmuir*, submitted for publication. Unpublished work copyright 2012 American Chemical Society.

Chapter 4.1 Background

Controlling the properties of molecular monolayers on solid surfaces is critical for many applications including wear resistant coatings, corrosion protection and protein repellent biomedical devices.⁸⁹⁻⁹¹ One of the most commonly used surface treatments is

to form self-assembled monolayers (SAMS) with ligand molecules that chemisorb onto surfaces.^{92,93} These surface coatings are particularly easy to form on gold substrates via thiol-gold covalent bonding and by functionalizing the desired ligand with a terminal thiol group. Gold decorated with poly(ethylene glycol) (PEG) is particularly useful in biomedical applications because it can significantly enhance biocompatibility.⁹⁴ The presence of surface-bound PEG is shown to reduce the non-specific physisorption of proteins on metal surfaces, which reduces the immune response and tissue inflammation.^{94,95} Thus, it is important to understand and characterize the effects of PEG grafting density and chain conformation on gold nanoparticles. Furthermore, it is also common to functionalize surfaces with mixtures of ligands to induce multifunctionality in the SAMS coating. For cancer therapies, ligands with cell-targeting capabilities are used to decrease toxicity and improve treatment efficiency.⁹⁴ Therefore, it is critical to understand how mixtures of thiol molecules adsorb and interact with each other in surfaces.

Prior work has demonstrated that surface-bound thiolated ligands are mobile on gold surfaces and that mixtures of immiscible ligands will often segregate.^{78,96} More recently, it has been shown that chemically distinct ligands on gold nanoparticle surfaces will spontaneously form ordered striped patterns.^{77,91,97} However, there is also new evidence suggesting that bound thiol molecules are more likely to desorb from gold surfaces and exchange positions with unbound thiol ligands than they are to diffuse along the gold surface. Schlenoff and colleagues characterized the self-exchange of surface-bound radiolabeled thiols with unlabeled thiols in solution.⁹⁸ Hackley et al. showed that chemically different thiol molecules will also competitively adsorb onto gold particles.^{81,}

⁹⁹ They showed that previously bound PEG-thiol could be subsequently removed by adsorbing mercaptopropionic acid and that the extent of replacement was controlled by the concentration of mercaptopropionic acid in solution. These findings are critical to enhancing our understanding of the behavior of multicomponent PEG-functionalized nanoparticle systems.

In Chapter 3, we presented a new scheme for synthesizing self-assembling gold nanoparticle surfactants using thiol molecules.⁶⁹ The method involves first functionalizing the particles with a controlled amount of PEG-thiol at concentrations below particle surface saturation that sterically stabilizes the particles in water. The particles are subsequently functionalized with an alkane-thiol rendering them amphiphilic. In a manner analogous to molecular surfactant micelles, these nanoparticle surfactants form clusters with their hydrophobic alkane-coated regions in the center of the cluster. This is shown schematically in Figure 4.1. Additionally, it was found that the concentration of PEG-thiol on the gold surface controls the aggregation number of the clusters. The PEG chains sterically prevent particles from aggregating and this forces approaching particles to bind in regions that are not covered by polymer. We previously showed data suggesting that the two thiol molecules, PEG and alkane-thiol, must be partially segregated on the gold surface. Spectroscopy results show that the inter-particle spacing is controlled by the length of the alkane-thiol, which acts as a molecular spacer between close-packed particles in the clusters. In order to further control the cluster structure and self-assembly, it is important to fully understand the competitive adsorption of thiolated ligands on the gold particle surface. Furthermore, because steric interactions

affect particle binding, studying the conformation of tethered PEG chains as a function of concentration and surface composition is also critical to controlling clustering behavior.

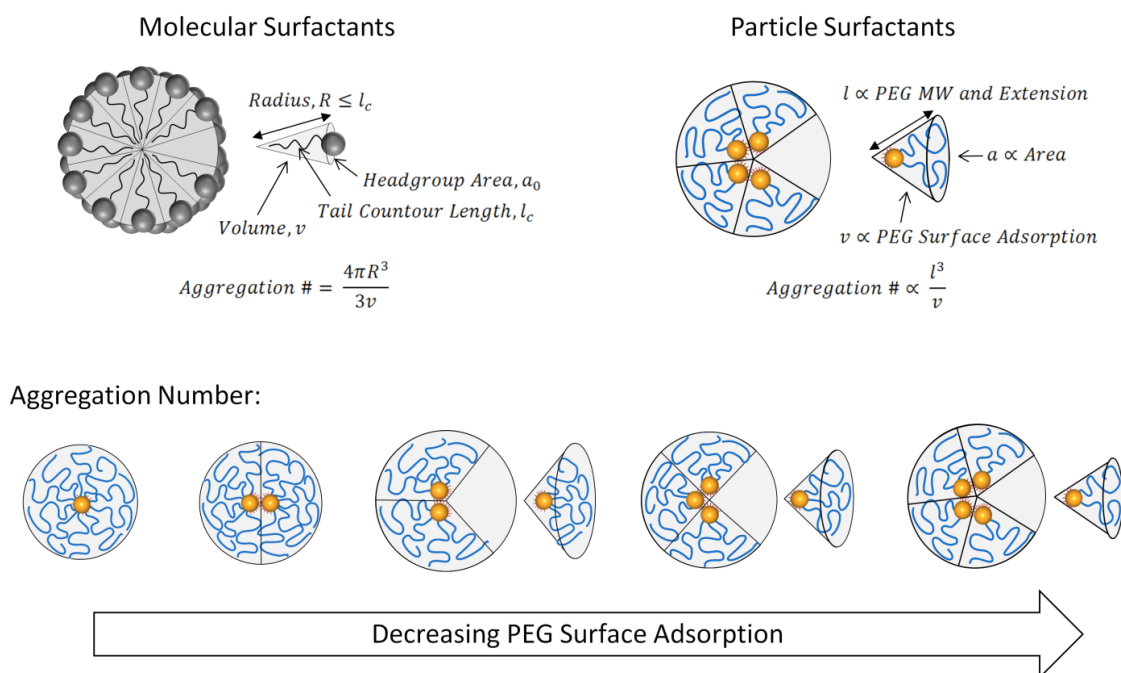


Figure 4.1. Schematic comparison of cluster and micelle structures formed in nanoparticle surfactants and in traditional molecular surfactants. The aggregation number in both systems is controlled by geometric parameters. For nanoparticle surfactants these correspond to the polymer conformation and the surface concentration.

In this chapter, we demonstrate that alkane-thiol molecules will competitively adsorb onto gold surfaces and replace previously bound PEG-thiol. Furthermore, the extent of thiol replacement is strongly dependent on the length of the alkane-thiol. Shorter alkane-thiol molecules are found to replace larger amounts of PEG-thiol than the longer alkane-thiol molecules. We also show that the conformation of the PEG-thiol is influenced to a large extent by the length of the alkane-thiol. Particles functionalized with alkanes of intermediate lengths (e.g. hexane-thiol and octane-thiol) cause the bound PEG

to have a more extended conformation. As expected, these factors have a profound impact on cluster formation and on the aggregation number of particles in each cluster.

4.2 Experimental Methods

Sodium citrate, auric chloride, butane-thiol, hexane-thiol, octane-thiol, decane-thiol, dodecane-thiol and tetradecane-thiol are purchased from Sigma Aldrich (St. Louis, MO) and used as received. Thiol terminated poly(ethylene glycol) methyl ether of 10 kDa, containing a single thiol group, is obtained from Polymer Source (Dorval, Quebec Canada). Monodisperse gold nanoparticles ($r = 5.5$ nm) are synthesized in aqueous buffer following the procedure described by Frens et al.⁸² Particles are subsequently functionalized using thiol-gold covalent bonding chemistry. First, the particles are functionalized with PEG-thiol at dose concentrations ranging from 1 to 20 PEG chains/nm² Au. The particle dispersions are then divided into seven aliquots, six of which are functionalized with alkane-thiols ranging in length from 4 to 14 carbons. The alkane-thiol is added at an excess concentration that is enough to bind with all of the available gold sites and to reach surface saturation (700 molecules/nm² Au). All samples are then dialyzed to remove any unbound thiol ligands. All experiments are performed in triplicates. The first set of samples are dialyzed using pressure diafiltration (Millipore) and are passed through a 50 kDa PBTK membrane 20 times. The other two data sets are dialyzed using 50 kDa cellulose ester dialysis tubing from Spectrum Laboratories with 5 solvent exchanges that lasted one day each. Different dialysis methods were used to corroborate that all un-bound molecules were removed from the samples. All three trials have remarkable reproducibility and the average values are presented.

Thermogravimetric Analysis (TGA) is performed on dialyzed and lyophilized samples. TGA is completed with a TA Instruments TGA-Q50 using a ramp rate of 1 °C/minute and a nitrogen flowrate of 40 mL/minute. The hydrodynamic radii and electrophoretic mobility of particles are measured with a Malvern Zetasizer Nano ZS (Worcestershire, United Kingdom) with a laser wavelength of 633 nm. A folded capillary cell (DTS 1060) was used for measuring the electrophoretic mobility. Zeta potentials of the particles are calculated from their mobility using the Hückel approximation.¹⁰⁰

Lyophilized clusters are also examined with a FEI Tecnai G2 F20 Transmission Electron Microscope (TEM) operating at 200 kV. Clusters are deposited on a copper TEM grid with a Formvar support film by placing a drop of 0.005 wt% gold dispersion on the grid followed by freeze-drying. The freeze-drying process is used to avoid aggregation due to capillary forces experienced during drying of liquid samples.

Small-Angle X-ray Scattering (SAXS) is used to examine the particle arrangement of the stable clusters in aqueous dispersion. SAXS is performed on an Anton Paar SAXSess (Graz, Austria) using a line-collimated Cu- $k\alpha$ source with a wavelength of 1.54 Å. The difference in scattering length density of gold and water ($\Delta\rho_{Au-H_2O}=1.14*10^{-4}$ Å⁻²) is much larger than PEG and water ($\Delta\rho_{PEG-H_2O}=1.80*10^{-7}$ Å⁻²), so the scattering intensity comes primarily from the particles.

4.3 Results

4.3.1 Thiol Surface Adsorption

The surface adsorption of thiols is quantified using TGA on particles that had been previously lyophilized to remove the water phase. For these measurements, particles are initially functionalized with a dose concentration of 20 PEG chains/nm²Au, which is enough PEG-thiol to ensure that the gold surface is fully saturated. Subsequently, particles are functionalized with an alkane-thiol that is added in large excess (700 molecules/nm²Au). After functionalization, the particles are dialyzed to remove any unbound PEG-thiol and alkane-thiol that is either never adsorbed to a particle or that may be desorbed from the surface as it is displaced through competitive adsorption. Figure 4.2 shows there is a clear decrease in PEG-thiol concentration when tetradecane-thiol is added. Particles that are fully saturated with PEG-thiol initially have a surface concentration of 2.0 ± 0.29 PEG chains/nm²Au. After functionalization with tetradecane-thiol, the concentration is reduced to only 0.87 ± 0.01 PEG chains/nm²Au. Additionally, two separate decays are observed for the amphiphilic particle corresponding to the alkane-thiol at 230 °C and the PEG thiol at 380 °C. These decays occur at the same temperature as those measured on particles that are only functionalized with tetradecane-thiol or PEG-thiol. The significant decrease in PEG surface concentration measured by TGA suggests that the alkane-thiol must competitively adsorb onto the gold surface and replace previously bound PEG-thiol. We also note that there is a very large surface concentration of tetradecane-thiol in amphiphilic particles, suggesting that the alkane-thiol must also replace citrate molecules that stabilize the bare gold nanoparticles.

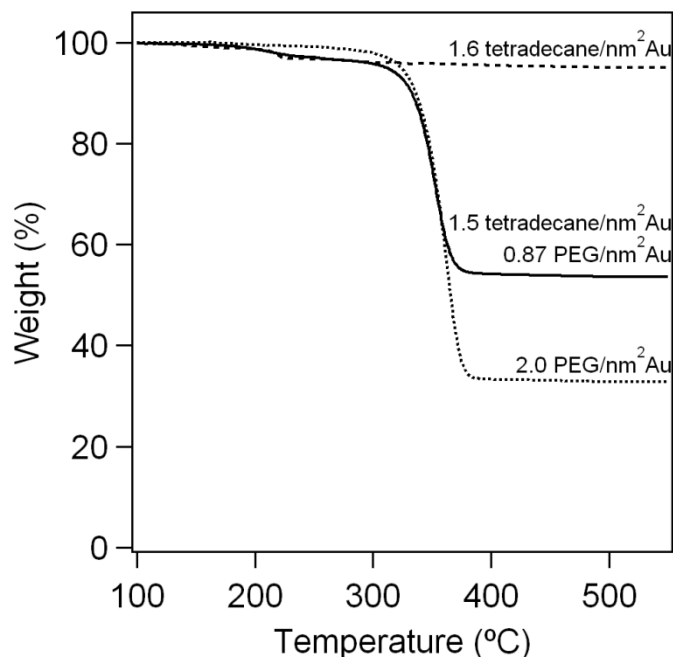


Figure 4.2. TGA profile of tetradecane-thiol (dashed), PEG-thiol (dotted) and both tetradecane –thiol and PEG-thiol (solid) functionalized gold samples after extensive dialysis to remove unbound ligands and after freeze-drying (lyophilization). The dose concentrations of each ligand are 700 tetradecane molecules/nm²Au and 20 PEG chains/nm²Au.

Similar TGA experiments are also performed using alkane-thiols of different chain length to render the particles amphiphilic. Figure 4.3a shows the surface adsorption of PEG-thiol as a function of the number of carbons in the alkane chain. We clearly see that alkane-thiols of different size replace the surface-bound PEG-thiol to different extents. Additionally, all alkane-thiols form self-assembled monolayers (SAMS) on the gold surface but the surface concentration of the molecules varies non-monotonically with chain length. Figure 4.3b shows that the highest surface density occurs for hexane-thiol and octane-thiol. This unexpected result is likely related to the capacity of different alkane-thiols to form orderly packed SAMS on gold. Porter and colleagues showed that alkane-thiols shorter than five carbons will not form ordered monolayers on flat gold

substrates like those observed for longer alkane-thiols because of weaker inter-chain van der Waals interactions and due to the presence of defects such as gauche kinks in these alkyl chains.⁸⁵ Chain-end defects are also known to occur in SAMs of longer alkane-thiols in nanoparticles because the high radius of curvature causes a decrease in packing density the further an alkane group is from the surface.¹⁰¹ Therefore, alkane-thiols of intermediate chain lengths are likely to form the most ordered and dense monolayers in nanoparticle surfaces.

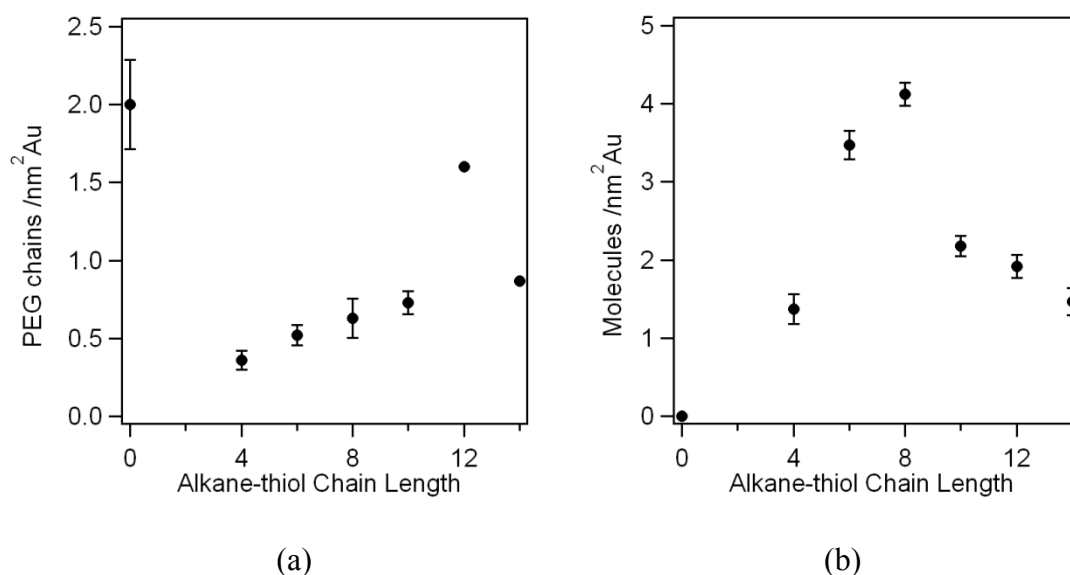


Figure 4.3. a) Surface concentrations of a) PEG-thiol and b) alkane-thiol after particles with a dose concentration of 20 PEG chains/nm²Au are functionalized with 700 alkane-thiol molecules/nm²Au. Surface concentrations are determined by TGA after the particles are dialyzed to remove unbound ligands and freeze-drying (lyophilization).

Zeta potential measurements can provide additional information on the amount of the citrate that is displaced through thiol adsorption and on the PEG conformation. As expected, the original gold particles show the largest zeta-potential magnitude (-56.8 ± 1.9 mV) due to the surface charge of the citrate molecules that stabilize the particles after

synthesis. There is a decrease in the magnitude of the zeta potential after saturating the surface with PEG-thiol (2.0 PEG chains/nm²Au) that is explained by shifting the shear plane away from the particle surface. Figure 4.4 also shows that the zeta potential is further reduced after functionalization with alkane-thiols because the negatively charged citrate is displaced. Importantly, there are remarkable similarities in the data trends that are also observed in the TGA results. The highest surface concentration from TGA occurs for octane-thiol and this sample also has the lowest magnitude of zeta potential. This suggests that octane-thiol is able to displace more citrate than other alkane-thiol molecules. However, it is impossible to get quantitative information about the particle surface charge because the PEG conformation will also affect the zeta potential by moving the slip plane.

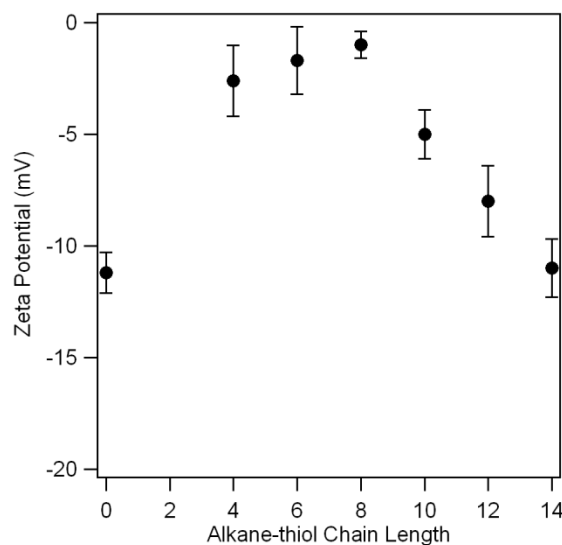


Figure 4.4. Zeta potential of nanoparticle surfactants with an initial PEG-thiol surface concentration of 2.0 PEG chains/nm² Au and different alkane-thiols.

4.3.2 PEG Conformation

Dynamic Light Scattering (DLS) is also used to characterize the extension of grafted PEG chains after functionalization with alkane-thiols of different length. For these studies, the particles are first saturated with PEG-thiol so that, even after alkane-thiol is added, the particles are in a ‘singlet’ state and are unable to form clusters. The formation of ‘singlets’ is confirmed with small-angle x-ray scattering (SAXS) and this is shown in the inset of Figure 4.5. All of the scattering curves of particles with PEG and alkane-thiol are identical to that of the original gold particles. This means that any differences observed in the hydrodynamic radii (R_h) measured with DLS originates from changes in the PEG extension and not from the clustering of particles. Figure 4.5 shows clear changes in R_h depending on the specific alkane-thiol that is co-adsorbed on the gold surface after PEG functionalization. For butane-thiol, decane-thiol, dodecane-thiol and tetradecane-thiol there is a modest decrease in R_h from 36 nm to approximately 31 nm upon alkane-thiol addition. This could originate from the partial replacement of PEG-thiol by alkane-thiol during the functionalization process. However, based on TGA results, one would expect butane-thiol to have the lowest R_h because it is shown to remove the largest amounts of PEG-thiol. Surprisingly, there is a significant increase in R_h observed for particles coated with hexane-thiol and octane-thiol, relative to particles only coated with PEG, even though TGA shows that there is a decrease in the amount of surface-bound PEG in these particles. This suggests that the hydrodynamic size of the particles is not solely controlled by the surface concentration of PEG-thiol and that other factors must also influence particle diffusion.

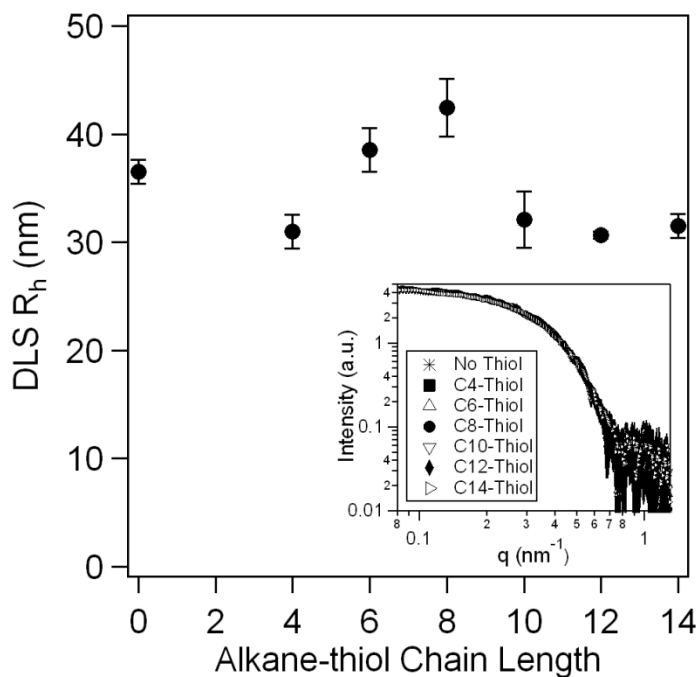


Figure 4.5. Hydrodynamic radii of nanoparticle surfactants with an initial PEG concentration of 2.0 PEG chains/nm² Au and different alkane-thiols added in large excess to saturate the surface. The inset contains SAXS curves proving that all of the individual nanoparticles are un-clustered in dispersion.

By plotting the surface concentration data (TGA) together with the hydrodynamic radii for singlet particles (DLS), we gain a deeper understanding of the influence of the conformation of the PEG-thiol (Figure 4.6). Figure 4.6a shows that in one extreme octane-thiol functionalization results in more extended PEG-thiol conformations even though they have a low surface concentration. In the other extreme we see dodecane-thiol functionalization results in the highest surface concentration of PEG-thiol but also that the polymer is in a more collapsed conformation. This result is best explained by also examining the surface concentration of alkane thiol molecules. Figure 4.6b shows a clear trend between the measured hydrodynamic radius of particles and the surface concentration of the alkane-thiol molecules. Particles with low alkane-thiol surface

concentrations also have smaller hydrodynamic radii and a more collapse PEG-thiol conformation. Conversely, octane-thiol has the highest surface coverage and also results in the most extended PEG-thiol conformation.

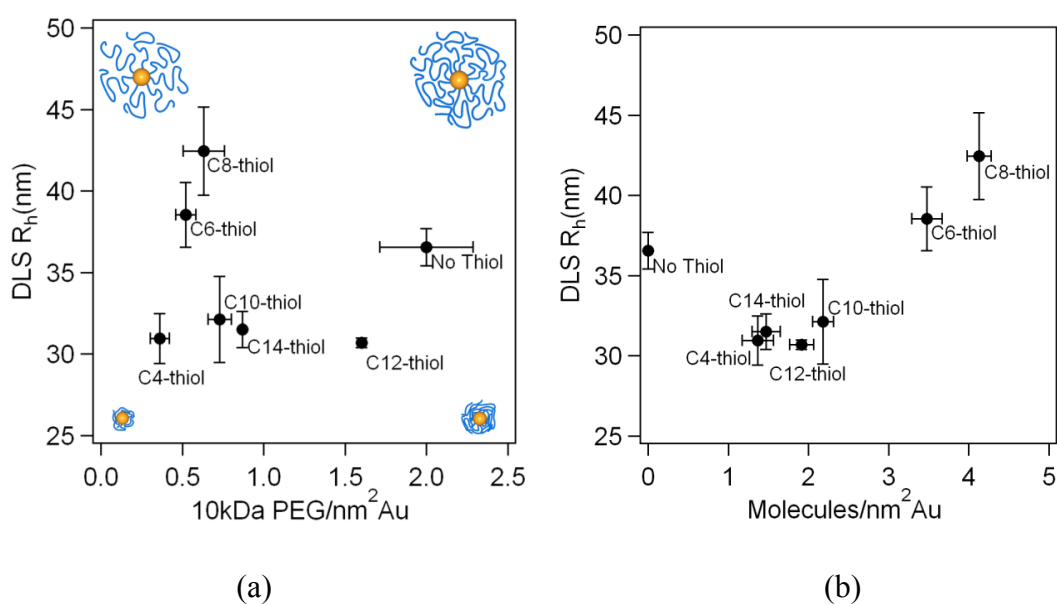


Figure 4.6. Comparison of hydrodynamic radii to a) PEG-thiol and b) alkane-thiol surface concentrations for fully saturated singlet particles.

Taken together, the data suggest that some of the PEG-thiol chains are likely in a collapsed conformation when there are exposed patches of citrate or gold atoms on the surface. Thus, we hypothesize that some PEG chains adsorb on the gold surface and may wrap around the particle due to favorable interactions. The case of PEG-thiol functionalized particles prior to alkane addition is illustrated schematically in Figure 4.7a. After the addition of butane-thiol, decane-thiol, dodecane-thiol or tetradecane-thiol, a somewhat disordered monolayer forms on the particle surface leaving patches of exposed gold or citrate. Some of the PEG-thiol chains will remain in a more contracted conformation as they interact with exposed patches of the gold particle as shown in

Figure 4.7b. The hydrodynamic radius will be smaller for these particles because some of the PEG-thiol is displaced from the particle when the alkane-thiol is added. Finally, when dense, ordered monolayers of octane-thiol or hexane-thiol cover the majority of the gold surface, the PEG-thiol chains will have repulsive interactions with the dense hydrophobic alkane surface and more extended conformation will be favored as illustrated in Figure 4.7c.

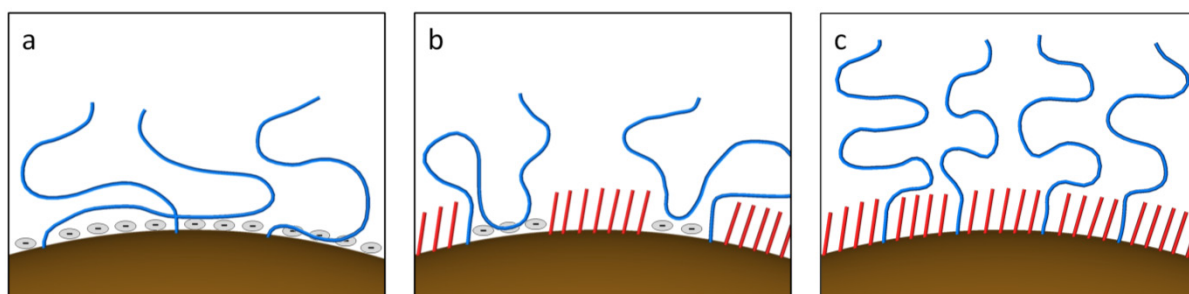


Figure 4.7. Schematic representation of the PEG-thiol conformation a) in the absence of alkane-thiol, b) in the presence of a patchy alkane-thiol monolayer and c) in the presence of an ordered alkane-thiol monolayer.

4.3.3 Effects of PEG Concentration and Conformation on Cluster Formation

The surface concentration and conformation of the PEG-thiol has a significant effect on the clustering of nanoparticle surfactants. The formation of clusters for samples with five different initial PEG-thiol concentrations ranging 0.1 – 1.0 PEG chains/nm²Au are examined as a function of the type of alkane-thiol that is added. The PEG-thiol concentrations reported in this section refer to the initial concentration and do not reflect the amount of PEG-thiol that is replaced during alkane-thiol functionalization. Small-angle x-ray scattering (SAXS) is used to probe the cluster structures directly in the

dispersed state. Due to the large scattering contrast of gold relative to PEG, the scattering contribution in SAXS originates primarily from the shape and arrangement of the gold nanoparticles. Figure 4.8 shows the systematic changes that occur in the scattering curves as the number of particles per cluster increases. At high values of q , all of the data collapse because the intra-particle correlations corresponding to the spherical shape dominates the scattering. In contrast, at medium and low values of q , there are large variations in the scattering profiles due to inter-particle correlations that occur with cluster formation. There is also a clear shift of the Guinier plateau towards lower values of q indicating the formation of larger structures. At PEG concentrations above 0.3 PEG chains/nm²Au, decane-thiol, dodecane-thiol and tetradecane-thiol show no clustering and the scattering curves are identical to those for particles without alkane-thiol. However, clustering is readily observed from the deviations in scattering at low q for nanoparticle surfactants with butane-thiol, hexane-thiol and octane-thiol. Particles with the longer alkane-thiol chains only begin to cluster at PEG-thiol concentrations lower than 0.2 PEG chains/nm²Au while the butane-thiol, hexane-thiol and octane-thiol particles form extremely large clusters that are not stable in dispersion. For all PEG-thiol concentrations, the scattering data indicates that octane-thiol coated nanoparticle surfactants contain the most particles in each cluster. SAXS curves for initial concentrations of 0.3, 0.7 and 1.0 PEG chains/nm²Au are shown in Figure 4.8.

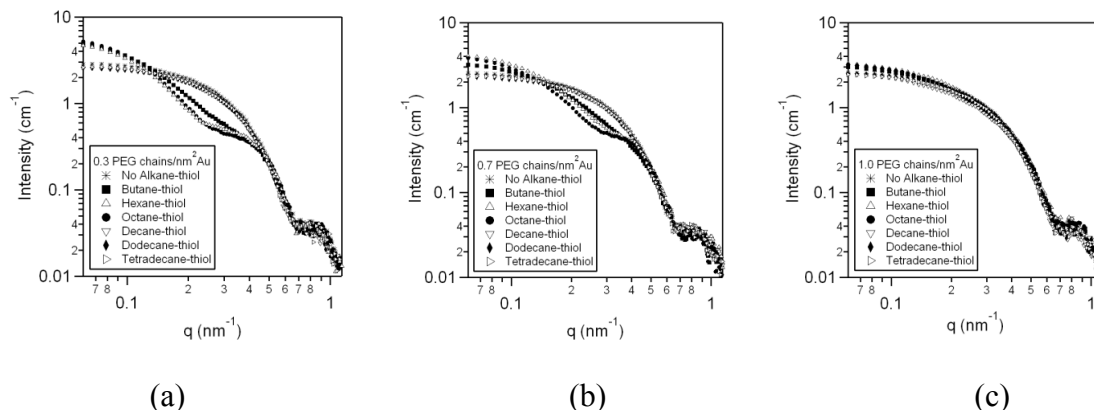


Figure 4.8. SAXS data corresponding to nanoparticle surfactants clustered with different alkane-thiol additives and after coating with a) 0.3 PEG chains/nm²Au, b) 0.7 PEG chains/nm²Au and c) 1.0 PEG chains/nm²Au.

The cluster size can be easily quantified from scattering data using a simple Guinier analysis to calculate the radius of gyration, R_g , for each structure. The radius of gyration for each sample is calculated from the Guinier regime of the scattering curves using Equation 4.1 where q is the scattering vector and a_0 is the zero angle intensity.⁸⁸ Due to the large difference in scattering contrast of gold-water ($\Delta\rho=1.14\cdot 10^{-4}\text{ \AA}^{-2}$) relative to PEG-water ($\Delta\rho=1.80\text{E-}7\text{ \AA}^{-2}$), the value of R_g only depends on the gold portion of the clusters. Details of this analysis are located in Chapter 2.

$$\ln[I(q)] = \ln[a_0] - \frac{R_g^2}{3} q^2 \quad (4.1)$$

Figure 4.9 shows that R_g for all 10kDa PEG-thiol loadings is constant at 5.8 nm when no alkane-thiol is added because the particles are not clustered. At initial PEG-thiol concentrations above 0.3 10kDa PEG chains/nm²Au and alkane-thiols equal or greater than 10 carbons, the nanoparticle surfactants are still ‘singlets’ and the R_g remains at 5.8 nm. In contrast, there is a sharp increase in R_g for alkane-thiol molecules with chain lengths below 8 carbons that corresponds to the increasing aggregation of particles.

Octane-thiol coated nanoparticle surfactants again result in the largest R_g for all of the 10kDa PEG-thiol loadings studied.

Clusters formed from nanoparticle surfactants with 5kDa PEG-thiol also show similar trends as 10kDa PEG-thiol nanoparticle surfactants but with some slight deviations as demonstrated in Figure 4.9b. Both samples show that alkane-thiol molecules smaller than eight carbons are more effective at inducing cluster formation. Furthermore, most samples show maxima in the cluster sizes for intermediate thiol lengths (octane and hexane thiol). Nanoparticle surfactants with decane-thiol, dodecane-thiol and tetradecane-thiol are also found to be ‘singlets’ at PEG-thiol concentrations that are greater or equal to 1.0 PEG chain/nm²Au (5 kDa). In general, the values necessary for forming clusters with the lower molecular weight polymer are larger than the surface concentrations necessary with 10kDa PEG-thiol. This suggests, as expected, that the larger effective volume of individual 10kDa PEG-thiol chains requires lower PEG surface concentrations, relative to 5 kDa PEG, to form clusters with similar aggregation numbers. This is further rationalized by considering that the total steric repulsion volume v (i.e. the volume of the exclusion cones in Figure 4.1) will be roughly proportional to the exclusion volume of individual chains multiplied by the number of chains attached to the particle surface.

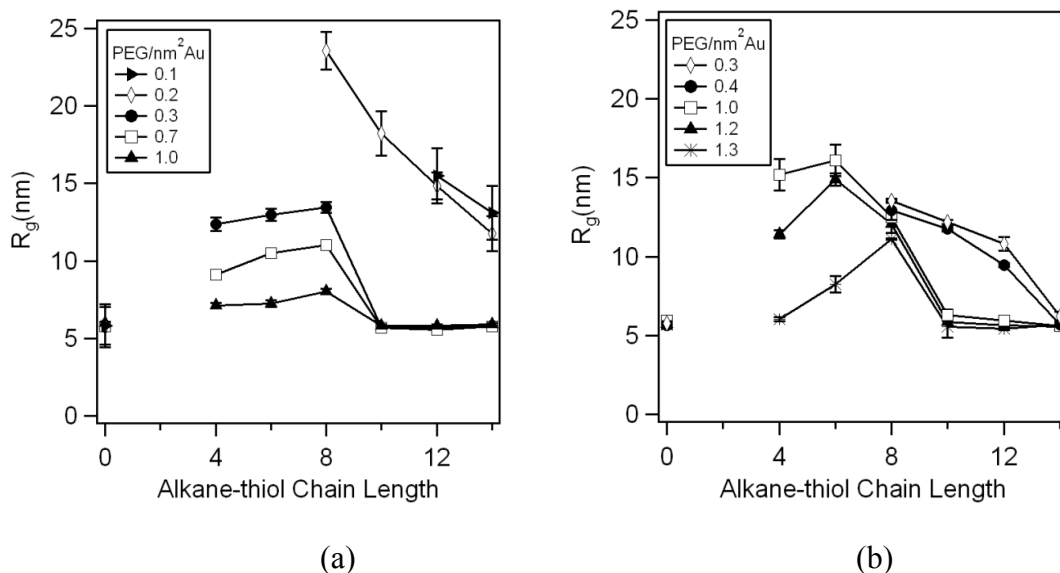


Figure 4.9. Radius of gyration of clusters plotted against the number of carbons in the alkane chain for variable initial PEG-thiol surface concentrations with (a) 10kDa PEG-thiol and (b) 5kDa PEG-thiol. The error bars correspond to the uncertainty in the fit to the Guinier equation.

Transmission electron microscopy (TEM) is also used to characterize the number of particles in each cluster for nanoparticle surfactants initially containing a surface concentration of 0.3 PEG chains/nm²Au (before alkane-thiol addition). Figure 4.10 shows representative electron micrographs out of tens of images that are taken for each sample. Unfortunately, clusters collapse during the drying so it is impossible to fully characterize their stable dispersion geometry despite the use of freeze-drying to minimize this effect. Still, TEM images are useful to directly quantify the number of particles in each cluster. TEM shows that there is a distribution of cluster sizes in each sample rather than a single cluster type. Histograms are created to quantify and compare the number of particles per cluster for each sample. As expected, the largest clusters are formed for octane-thiol nanoparticle surfactants with an average of 9 particles per cluster at this initial PEG concentration. The aggregation numbers for butane-thiol and hexane-thiol are 5 and 8

particles respectively. This trend is in perfect agreement with the SAXS data. As expected, the particles correspond to primarily singlets for larger alkane chain lengths (decane-thiol, dodecane-thiol and tetradecane-thiol).

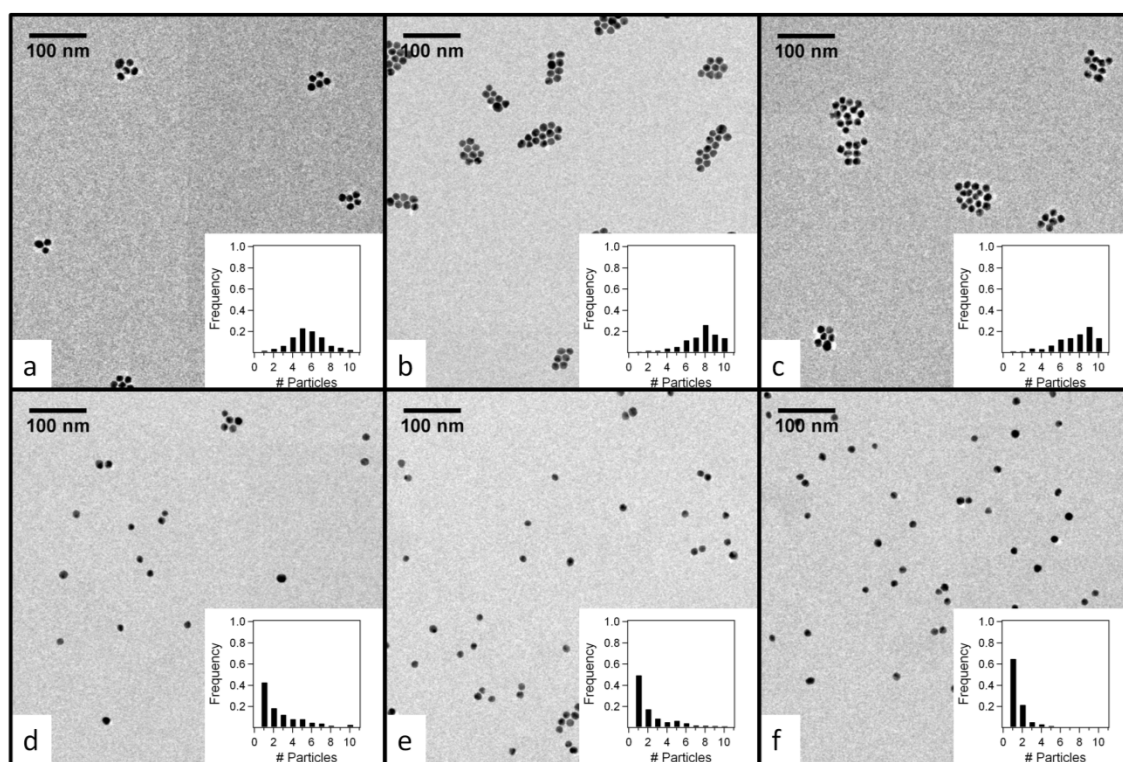


Figure 4.10. Representative TEM micrographs for nanoparticle surfactants with 0.3 PEG chains/nm²Au and a) butane-thiol, b) hexane-thiol, c) octane-thiol, d) decane-thiol, e) dodecane-thiol and f) tetradecane-thiol. The insets are histograms indicating the distribution of the particles per cluster for each sample.

4.4 Discussion

It is clear from electron microscopy and x-ray scattering results that the PEG-thiol surface concentration and the chain extension have a profound effect on cluster sizes in nanoparticle surfactants. As previously mentioned, these clusters form in a way that is analogous to molecular surfactants with the hydrophobic regions shielded on the inside of the structure. Therefore, it is not surprising that aggregation numbers will also be

controlled by the same geometric parameters that control aggregation in molecular surfactants. Equation 4.2 can be used to roughly relate the aggregation number of spherical surfactant micelles to geometric parameters. Here, R is the micelle radius and v is the volume occupied by the tail.^{32, 102}

$$Aggregation\#_{molecular} = \frac{4\pi R^3}{3v} \quad (4.2)$$

We propose that the aggregation number of nanoparticle surfactants will also be related to the concentration and conformation of the bound polymer. In Equation 4.3, the polymer length l will be controlled by the size and conformation of the PEG-thiol and, for mushroom chain conformations, it will be roughly proportional to the Flory radius. The steric interaction volume, v , will also be influenced by the surface conformation of the individual chains and by the total surface concentration of bound PEG-thiol. Thus, we expect the molecular weight of the PEG-thiol to also affect the aggregation behavior. However, it is still challenging to fully quantify the influence of this effect using this simplistic model because molecular weight could cause significant changes in chain conformation and in the steric exclusion volume. Scaling models for predicting micelle formation in bunched micelles could potentially be extended to more precisely predict and describe cluster formation in these systems.¹⁰³

$$Aggregation\#_{particle} \propto \frac{l^3}{v} \quad (4.3)$$

Nevertheless, this very simple analogy to molecular surfactants shows good general agreement with the observations in the experimental data. For any given molecular weight of PEG-thiol, the aggregation number is always inversely proportional to the surface concentration of polymer. This is best demonstrated by the data shown in

Figure 4.9. We also demonstrate this in a previous publication by systematically changing the dose PEG-thiol concentration and holding the alkane-thiol constant.⁶⁹ However, it must also be noted that the dependence will likely be different for particles coated with different alkane-thiols because it will be affected by any changes in PEG conformation that occur due to changing surface interactions (i.e. partial collapse vs. extended) and by preferential displacement of PEG with different alkane-thiols.

Our data suggests that the aggregation number of clusters is in-fact affected by changing polymer conformations. Nanoparticle clusters formed after adsorption of hexane-thiol and octane-thiol consistently have the most extended PEG-thiol conformations (Figure 4.6) and also show the largest aggregation numbers (Figure 4.9). Notably, this is observed in spite of having a higher PEG-thiol surface concentration, and therefore larger steric exclusion volumes, than butane-thiol coated particles. Unfortunately, it is not yet possible to fully determine the clustering mechanism of nanoparticle surfactants with partially collapsed PEG conformations. It is possible that these nanoparticles cluster to a somewhat lower degree because some of the PEG-thiol could wrap around the particle and make some of the alkane-thiol surfaces less accessible to other particles. Therefore, the hydrophobic and van der Waals interactions driving particle aggregation could be weakened. Still, it is clear that the polymer extension is a significant factor controlling the size and aggregation number of clusters formed from nanoparticle surfactants.

Finally, we also examine the effect of PEG-thiol molecular weight on the aggregation number. SAXS data shows that decreasing the PEG-thiol molecular weight from 10kDa to 5kDa while holding the initial PEG-thiol surface concentration constant,

causes nanoparticle surfactants to form larger clusters with larger aggregation numbers. This suggests, as expected from Equation 4.3, that a decrease in the steric exclusion volume occupied by the smaller PEG-thiol chains for similar surface concentrations has a large and inversely-proportional effect over the aggregation number.

Our findings show that polymer conformation and surface concentration are key to controlling the self-assembly of nanoparticle surfactants in dispersion. However, these results also have important implications to other systems that utilize gold-thiol bonding chemistry. For example, the functionalization of gold nanoparticles is of particular importance in nano-medicine applications. For these systems, the presence of surface-bound PEG has been shown to enhance biocompatibility and to prevent or postpone immune responses by preventing adsorption of proteins to gold surfaces.^{94,95} Additionally, ligands with antibody labels are frequently co-functionalized onto gold surfaces for targeted cancer therapies.^{104,105} Here we confirm prior work showing that significant thiol replacement occurs when a small thiol is added to nanoparticles after PEG-thiol functionalization. Thus, it is very important to quantify and understand the parameters that affect the relative adsorption and desorption of different thiol species that bind to the same surface. Our findings indicate that, even for simple alkanes, the length of the ligand can induce significant changes and that this could be used to tune relative adsorption to achieve desired surface concentrations. Furthermore, it is also important to note the influence of the alkane-thiol monolayer on the extension of PEG or other surface grafted polymers. This could significantly impact the ability to access other ligands and molecules located at the surface.

4.5 Summary

The concentration and conformation of surface-bound PEG-thiol in the presence of alkane-thiol ligands is critical to many applications utilizing thiol-metal functionalization. Here we show that alkane-thiols compete with PEG-thiol when they adsorb onto gold surfaces. We also show that the length of the alkane-thiol controls the extent of the PEG replacement. Furthermore, the alkane-thiol length also controls the packing density on the gold surface and this directly impacts the extension of the PEG-thiol. All of these factors are also shown to have a direct effect on the aggregation of self-assembly of nanoparticle surfactants and can be used to tune the cluster sizes.

Chapter 5: Charged Nanoparticle Adsorption at Oil-Water Interfaces

Here we examine the spontaneous adsorption of charged nanoparticles at hexadecane-water emulsion interfaces. The negative surface charge on the oil droplet surface has a significant effect on the adsorption of charged nanoparticles. The interaction potentials between the nanoparticles and oil droplets are calculated using DLVO theory. Calculations show that decreasing the surface charges with pH will reduce the energy barrier for particle adsorption. Additionally, increased ionic strength decreases the decay length of the electrostatic repulsion leading to enhanced particle adsorption. These theoretical calculations are corroborated with small-angle scattering experiments, which show that the highest particle adsorption of anionic PS latex to hexadecane oil droplets occurs at moderate ionic strength and low pH. This work shows that by carefully controlling solvent conditions such as pH and ionic strength, it is possible to tune particle adsorption at oil-water interfaces. The results presented in this chapter have previously been published as a regular article in *Langmuir*.¹⁰⁶ Reproduced with permission from Larson-Smith, K.; Jackson, A.; Pozzo, D. C., "SANS and SAXS Analysis of Charged Nanoparticle Adsorption at Oil-Water Interfaces" *Langmuir*, **2012**, 28, (5), 2493-2501. Copyright 2012 American Chemical Society.

5.1 Background

Particle-stabilized emulsions (Pickering emulsions) form when a fluid phase is mechanically dispersed in another immiscible fluid in the presence of solid particles.¹⁰⁷ These particles often adsorb and organize into a shell at the oil-water interface, which sterically prevents droplets from coalescing.¹⁰⁸⁻¹¹¹ In recent times, Pickering emulsions

have been the focus of much attention because of potential applications in the production of food, personal care and pharmaceutical products.¹¹²⁻¹¹⁴ Additionally, particle assemblies at oil-water interfaces can be used as templates for new materials such as composite particles and colloidosomes.^{1,2}

The remarkable stability of Pickering emulsions is mainly due to the favorable adsorption energy of colloidal particles at an oil-water interface. The energy necessary for particles to detach from the oil-water interface scales with the square of the particle radius as shown in Equation 5.1. Here, R is the particle radius, θ is the three-phase contact angle and γ_{ow} , γ_{pw} and γ_{po} are the oil-water, particle-water and particle-oil interfacial tension terms respectively.^{115, 116}

$$\Delta E = \frac{-\pi R^2}{\gamma_{ow}} \left[\gamma_{ow} - (\gamma_{po} - \gamma_{pw}) \right]^2 = \pi R^2 \gamma_{ow} (1 \pm \cos \theta)^2 \quad (5.1)$$

Frequently, the attachment energy of micrometer-sized particles is on the order of 10^7 kT making the adsorption extremely stable. In contrast, the attachment energy of nanoparticles decreases with decreasing size to the point where it can be comparable to thermal fluctuations. Thus, stability is highly dependent on the size of the particle and the stabilization of emulsions with nanoparticles is usually much less effective than for micrometer sized particles.¹¹¹ The interaction forces of particles located at dispersed oil-water interfaces are described in great detail in a review by Bresme and Oettel.¹¹⁷

Unfortunately, literature reports on the characterization of small particle (i.e. nanoparticles) adsorption to dispersed fluid interfaces are much less abundant than those of larger colloidal particles. This is in great part due to the experimental challenges that are encountered in analyzing very small length scales in complex dispersed systems.

Recently, Reincke and colleagues examined the self-assembly of charged gold nanoparticles at a macroscopic heptane-water interface.¹¹⁸ They showed that particles would reversibly adsorb and self-assemble at the oil-water interface when the surface charge of the particles was reduced. They modeled and explained this effect by accounting for dipolar and coulombic electrostatic repulsion and van der Waals attraction of particles at the interface. They found that, by reducing the particle surface charge, the equilibrium surface fraction of particles increased at the oil-water interface. This work provides great insight on the effect of interfacial and electrostatic interactions for nanoparticles at oil-water interfaces. However, before particles are able to experience these interfacial interactions they must first be able to reach the fluid-fluid interface. Under certain conditions, the interactions that are experienced by solid particles approaching an oil-water interface control emulsification efficiency and dominate over forces that would be experienced by adsorbed particles.

For Pickering emulsions, the specific method that is used to generate the dispersion can greatly affect the dominant physical interactions that govern colloidal behavior. In order to generate a Pickering emulsion, particles must either be forced towards the interface during mechanical emulsification or they must spontaneously adsorb to previously dispersed oil-water interfaces (Figure 5.1). Most reports usually focus on direct emulsification methods (Route 1) because they are more commonly used in practice. In this route, the large mechanical energy that is applied during the emulsification process (e.g. ultrasound application) allows most particles to reach an oil-water interface at some point. Therefore, colloidal behavior in these systems is largely governed by interfacial interactions that are experienced after the particles reach the

interface. In contrast, when particles are added after mechanical emulsification (Route 2), particle adsorption can be controlled by electrostatic and van der Waals forces between the oil drop and the dispersed particles.

The objective of this study is to improve our understanding of particle adsorption to existing oil-in-water dispersions when particles are added after mechanical emulsification. In this route, control of colloidal interactions through the change of solution conditions is found to be critical to controlling particle adsorption. Interfacial effects such as capillary forces only become relevant after particles reach the dispersed oil-water interface. This means that the magnitude of the adsorption energy due to the interfacial tension terms (Equation 5.1) is irrelevant if particles are prevented from approaching the interface due to electrostatic repulsion. The study is motivated by the fact that oil droplets frequently acquire large surface charges when dispersed in water and that these charges could prevent or enhance particle adsorption. To a first approximation, the classic DLVO theory can be used to describe the primary interactions of a charged particle approaching a larger oil droplet.

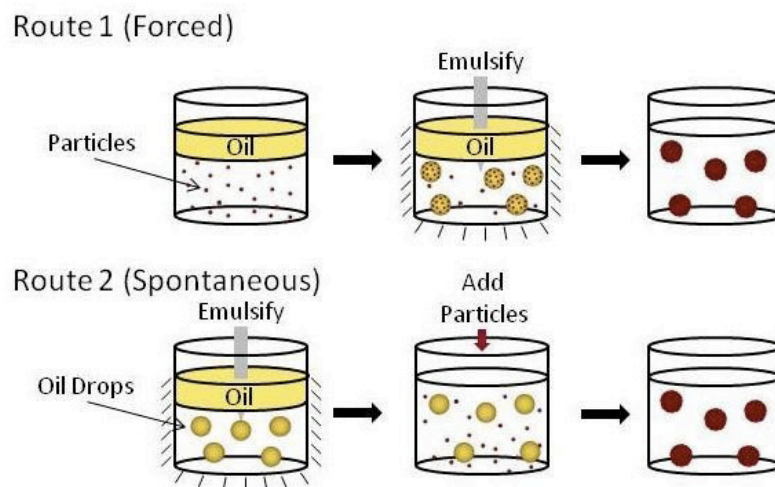


Figure 5.1. Methods to generate Pickering emulsions. Route 1: Direct mechanical dispersion of oil in the presence of particles. Route 2: Spontaneous adsorption of particles to an existing oil-in-water dispersion.

Aqueous emulsions prepared with simple alkanes in the dispersed phase can sometimes create a barrier to particle adsorption because they spontaneously acquire a significant surface charge. Stachurski and Michalek show that pure emulsions of all n-alkanes have a negative zeta potential that is effectively neutralized with decreasing pH.^{119, 120} The origin of the surface charge is widely discussed in the literature but a consensus is yet to be reached. One theory postulates that the negative zeta potential is caused by boundary-layer water molecules that are highly ordered at the interface with the oil phase.¹²⁰⁻¹²³ It has been shown that interfacial water molecules are preferentially oriented with the oxygen atoms pointing toward the oil phase.^{124, 125} This allows for selective adsorption of OH^- ions that interact with the exposed hydrogen atoms of the interfacial water molecules. Thus, an excess negative charge exists at the oil-water interface that is strongly dependent on the concentration of OH^- ions. A second theory postulates that the negative charge originates from charge transfer between different interfacial water molecules.¹²⁶ Regardless of the specific mechanism causing this surface charge, it is clearly important to consider the effects of electrostatic interactions on the formation of Pickering emulsions through spontaneous particle adsorption (Route 2). In addition, depending on emulsification conditions like the mechanical input power, electrostatic interactions could also dominate particle adsorption in mechanical emulsification processes (Route 1). Previously, Simovic and Prestige have shown the adsorption of hydrophilic silica particles at a polydimethylsiloxane-water interface is greatly dependent on salt concentration and weakly influenced by pH.^{127, 128} Whitby and colleagues also showed the adsorption and stability of amphiphilic silica particles at alkane-water interfaces is largely dependent on particle flocculation, which is controlled

by pH.¹¹¹ These studies further indicate that electrostatics play a large role in particle adsorption and must be carefully considered for spontaneous particle adsorption.

In this study, we use small angle neutron and x-ray scattering (SANS and SAXS) to evaluate the effect of surface charge on the spontaneous adsorption of charged particles at dispersed oil interfaces. SANS and SAXS are ideal techniques for probing the adsorption and arrangement of particles at buried oil-water interfaces. These techniques are especially valuable when optical or fluorescent microscopy is not possible because particles have sizes in the nanometer range.^{58, 129-137} Nevertheless, the extraction of quantitative data from scattering experiments is not always simple and requires the use of adequate models. The Pickering Model, introduced in Chapter 2, is an analytical model that can be used to determine the fraction of particles that adsorb at the oil-water interface.⁵⁸ Phase analysis light scattering (PALS) is also used to quantify zeta-potential values of the dispersed oil droplets and of the adsorbing particles under various solution conditions. Finally, the DLVO theory is used to calculate the interaction energy between a solid particle and an oil droplet. This simple model allows us to rationalize and understand the influence of electrostatic interactions in controlling nanoparticle adsorption for model oil-in-water emulsion systems.

5.2 Experimental Methods

Sodium chloride (NaCl), hydrochloric acid (1 N HCl), hexadecane (C₁₆H₃₄), gold chloride trihydrate (HAuCl₄·3H₂O), tetraoctylammonium bromide (TOAB), sodium borohydride (NaBH₄), toluene and mercaptoundecyl-trimethylammonium bromide are obtained from Sigma Aldrich (St. Louis, MO) and used as received. Deuterium oxide

($D > 99\%$) and d-hexadecane ($D > 98\%$) are purchased from Cambridge Isotopes (Andover, MA). Polystyrene (PS) latex nanoparticles (Nanosphere 80nm), purchased from Thermo Scientific (Fremont, CA), are dialyzed into water to remove any surfactant and then dialyzed into deuterium oxide (D_2O) for neutron scattering experiments. Gold nanoparticles ($r = 3$ nm) are synthesized in a water-toluene two phase system following the method of Brust et al.¹³⁸ A 0.025 M aqueous solution of hydrogen tetrachloroaurate (10 mL) is vigorously mixed with 25 mL of 0.05 M TOAB in toluene until all of the $AuCl_4^-$ is transferred into the organic phases. The $AuCl_4^-$ is reduced by slowly adding 10 mL of aqueous 0.4 M $NaBH_4$. After 6 hours of stirring, the particles are functionalized with mercaptoundecyl-trimethylammonium bromide and allowed to precipitate. The particles are then washed with copious amounts of toluene and ethanol before redispersion in water.

Hexadecane-in-water emulsions are prepared using a Branson Sonifier operated at 10% amplitude power pulsed one second on, two seconds off for a total of three minutes. Polystyrene or gold particles are added immediately after emulsification and the samples are placed on a roller mixer to prevent creaming. The size distribution of the emulsified oil drops is examined with a Zeiss Axiovert 40 CFL optical microscope at 40x magnification. Images are processed using Image J software developed at the National Institutes of Health.¹³⁹

The hydrodynamic radii and electrophoretic mobility of particles and oil are measured with a Malvern Zetasizer Nano ZS (Worcestershire, United Kingdom) with a laser with wavelength of 633 nm. A folded capillary cell (DTS 1060) was used for measuring the electrophoretic mobility of the particles and the hexadecane droplets in

separate experiments. Zeta potentials of the particles are calculated from mobilities using the White-Mangelsdorf model in the Zetasizer Nano ZS software that considers ionic mobility within the Stern layer.¹⁴⁰ The Helmholtz-Smoluchowski equation (Equation 5.2) is used to relate the electrophoretic mobility of the large hexadecane droplet (U_E) to the zeta potential (ζ). In this equation, η is the viscosity of the solvent, ϵ_0 is the dielectric permittivity in vacuum and ϵ_r is the relative dielectric permittivity of the solvent.³²

$$U_E = \frac{\epsilon_r \epsilon_0 \zeta}{\eta} \quad (5.2)$$

SANS experiments are performed on 1 vol% hexadecane in water emulsions stabilized by 80 nm PS latex at 0.25 vol%. The water phase consists of 6.0 vol% H₂O in D₂O and oil phase is comprised of 11.2 vol% h-hexadecane in d-hexadecane in order to eliminate the scattering contrast between the oil and water phases. At these conditions, the scattering contribution from the PS latex dominates the signal ($\Delta\rho_{PS-water} = 4.50 \cdot 10^{-6} \text{ \AA}^{-2}$). SANS and USANS experiments are performed at the National Institute of Standards and Technology (NIST) Center for Neutron Research using the NG3 SANS and BT5 USANS instruments.¹⁴¹ Three detector configurations were used for all SANS experiments. One detector configuration has a sample to detector distance of 15.3 m and utilizes lenses along with a neutron wavelength of 8 Å to focus the beam and reach a minimum wavevector value of 0.001 Å⁻¹. The other two configurations have sample to detector distances of 1 m and 4.5 m and use a wavelength of 6 Å to obtain a wide q range. USANS measurements are performed on the BT5 perfect crystal diffractometer extending the measured q range down to 8*10⁻⁵ Å⁻¹. The SANS and USANS data were fully reduced and placed on an absolute scale. Additionally, the USANS data were desmeared using Igor macros developed at NIST.⁵⁷

Small-Angle X-ray Scattering (SAXS) experiments are carried out on hexadecane emulsions stabilized by gold nanoparticles. SAXS experiments are performed on an Anton Paar SAXSess instrument (Graz, Austria) with a line-collimation system using a Cu-K α source with a wavelength of 1.54 Å. SAXS experiments are performed on a 0.2 vol% hexadecane in water emulsions stabilized by 0.002 vol% 5 nm mercaptoundecyl-trimethylammonium bromide capped gold nanoparticles. The difference in scattering length density of gold and water ($\Delta\rho_{\text{Gold-Water}}=1.14*10^{-4} \text{ \AA}^{-2}$) is much greater than hexadecane and water ($\Delta\rho_{\text{Hexadecane-Water}}=1.94*10^{-6} \text{ \AA}^{-2}$), so the gold particles also dominate the scattering in the SAXS system.

5.3 Surface Charge

5.3.1 Surface charges on dispersed oil droplets

The hexadecane-water interface has a negative charge that is neutralized by decreasing the pH of the aqueous phase. Figure 5.2 shows the variation of the zeta potential of hexadecane emulsions as a function of solvent conditions. The emulsion, without any additives, has a zeta potential of -103.4 mV at pH=7.5 and the magnitude linearly decreases until it is effectively neutralized at pH=2.5. The presence of salt only slightly decreases the zeta potential magnitude. Emulsions of pure oil in water at neutral pH are very stable and take several days to coalesce due to electrostatic stabilization. In contrast, we find that emulsions without added particles catastrophically destabilize at low pH due to the neutralization of the surface charge in the oil phase.

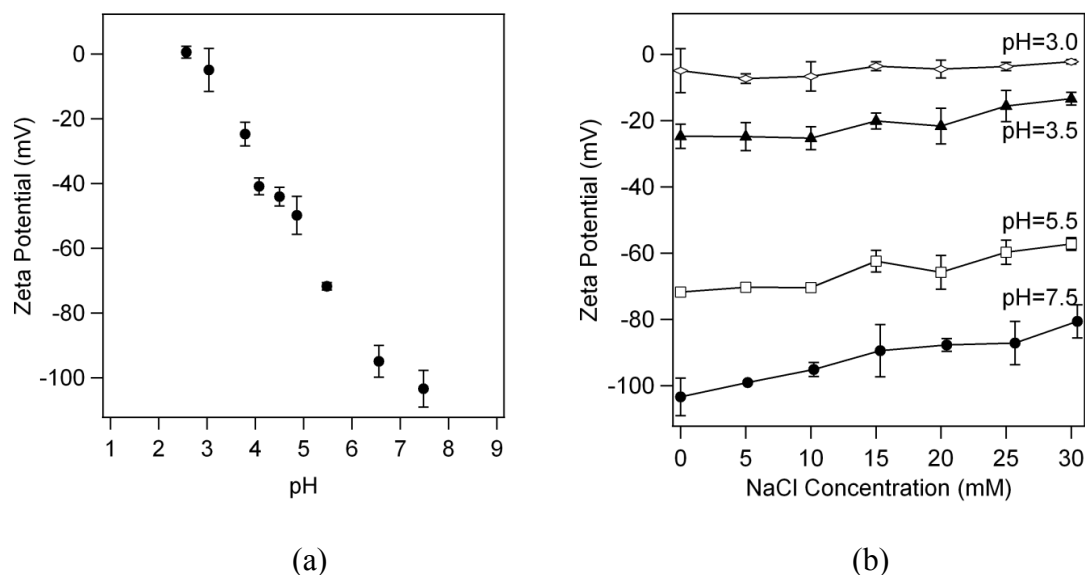


Figure 5.2. Zeta potential measurements for 0.001 vol% hexadecane emulsions as a function of (a) pH and (b) NaCl concentration.

5.3.2 Surface charges on sulfonated polystyrene latex

Changes in pH and salt concentration also affect the surface charge of the negatively charged PS latex particles. PS latex exhibits particularly interesting properties due to a hairy polymer layer that can form at the particle surface.¹⁴² Seebergh and Berg discussed the presence of these flexible polymer chains extending from the surface of the latex particles. These chains extend from the surface due to electrostatic repulsion between ionic groups in the ‘hairs’ and in the particle surface. By increasing the electrolyte content in the dispersion, the electrostatic repulsion is screened and the hairs collapse on the surface. This is demonstrated in Figure 5.3a, where the hydrodynamic radius shrinks from 44 to 41 nm in the presence of NaCl at concentrations higher than 5 mM. Figure 5.3b also shows that the surface charge of the PS latex systematically decreases at lower pH values. Lowering the pH causes cations to preferentially adsorb at the particle surface causing a reduction of the net surface charge.¹⁴³ The zeta potentials for PS latex as a function of pH in the presence of NaCl give a similar trend, but the

magnitude of the zeta potential is reduced. The PS latex never reaches neutrality at the conditions used in our study but, at pH=2, the smallest zeta potential is achieved with a value of -23 mV.

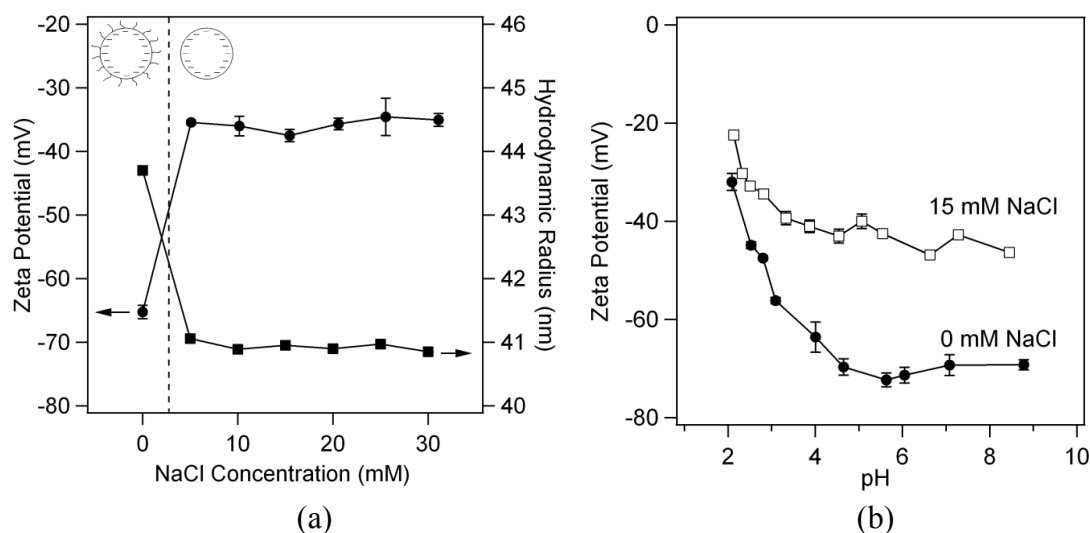


Figure 5.3. (a) Zeta potential and hydrodynamic radii for 0.05 vol% 80 nm PS latex as a function of NaCl concentration and (b) zeta potential for 0.05 vol% 80 nm PS latex as a function of pH.

5.3.3 Surface charges on gold nanoparticles

The surface charge of gold nanoparticles is easily manipulated through surface functionalization with self-assembled monolayers (SAMs).^{34, 83-85} Thiol chemistry has proven to be one of the most straightforward forms of gold functionalization because thiol groups have a strong affinity for metallic surfaces and form covalent bonds with surface atoms. Therefore, with careful selection of thiolated ligand, we can manipulate and control the surface charge of the particles. When mercaptoundecyl-trimethylammonium bromide is used, this yields a positive surface charge corresponding

to average zeta potential of 12 ± 3 mV. The zeta potential is found to be independent of pH and salt concentration over all solvent conditions that are used in this study.

5.4 DLVO theory and calculations

To a first approximation, DLVO theory is used to describe the interaction between particles and oil droplets before they make contact. The classic DLVO theory only accounts for the effects of van der Waals and electrostatic interactions between the two approaching surfaces.^{144, 145} The van der Waals interaction, U_{vdw} , is approximated by Equation 5.3 for two dissimilar spheres of radii a_1 and a_2 separated by a distance S_0 , where A_{213} is the corresponding Hamaker constant.¹⁴⁶ The effective Hamaker constant for different materials across a dissimilar medium is calculated according to Equation 5.4 such that $A_{gold-water-hexadecane} = 1.21 \cdot 10^{-20}$ J and $A_{PS-water-hexadecane} = 2.27 \cdot 10^{-21}$ J. The Hamaker constant for two polystyrene particles in water is $A_{PS-water-PS} = 1.3 \cdot 10^{-20}$ J. In all cases, the net force due to van der Waals interactions is found to be attractive.

$$U_{vdw} = -\frac{A_{213}}{3} \left[\frac{a_1 a_2}{S_0^2 + 2S_0 a_1 + 2S_0 a_2} + \frac{a_1 a_2}{S_0^2 + 2S_0 a_1 + 2S_0 a_2 + 4a_1 a_2} \right] + \frac{1}{2} \ln \left(\frac{S_0^2 + 2S_0 a_1 + 2S_0 a_2}{S_0^2 + 2S_0 a_1 + 2S_0 a_2 + 4a_1 a_2} \right) \quad (5.3)$$

$$A_{213} = \left(\sqrt{A_{22}} - \sqrt{A_{11}} \right) \left(\sqrt{A_{33}} - \sqrt{A_{11}} \right) \quad (5.4)$$

Electrostatic interactions can be either repulsive between like-charged particles or attractive between oppositely charged particles. In addition, electrostatic interactions can be manipulated through the control of the ionic strength in the solvent. Understanding these forces is useful for identifying the conditions that are adequate to drive the adsorption of dispersed particles to an oil-water interface. The electrostatic interaction,

U_{es} , can be approximated by Equation 5.5 where n_{∞} is the total ion concentration, κ^{-1} is the Debye length, k is Boltzmann's constant, T is temperature, z is the valence number, e is the electron charge and Ψ_{δ} is the Stern potential. γ is calculated with Equation 5.6 from the Stern potential, which is approximated by the measured zeta potential.

$$U_{es} = \frac{128\pi n_{\infty} kT \gamma_1 \gamma_2}{\kappa^2} \left(\frac{a_1 a_2}{a_1 + a_2} \right) \exp[-\kappa S_0] \quad (5.5)$$

$$\gamma = \tanh\left(\frac{ze\Psi_{\delta}}{4kT}\right) \quad (5.6)$$

Summing the van der Waals and electrostatic interactions gives the apparent net force between two approaching particles. The interaction force between n-decane droplets and micron-sized silica particles has previously been measured using atomic force microscopy. Hartley and colleagues showed agreement with DLVO theory at large separation distances where the decay length of the electrostatic interaction decreased with the addition of electrolyte.¹⁴⁷ Sunkel and Berg previously used DLVO theory to inform the adsorption of 150 nm titanium dioxide particles on mineral oil droplets.¹⁴⁸

One way to reduce the electrostatic repulsion between two equally charged surfaces is to decrease the Debye screening length (κ^{-1}) by increasing the ionic strength of the solution. In order to approximate conditions of our experiments, Figure 5.4 models the interaction potential for a 40 nm radius PS latex particle ($\zeta_1 = -43$ mV) and a 2 μm radius hexadecane droplet ($\zeta_2 = -95$ mV) at various concentrations of sodium chloride in the solvent. The addition of low amounts of NaCl can significantly decrease the decay length of the electrostatic repulsion. Still, in all cases the energetic barrier for adsorption is close to 200 kT.

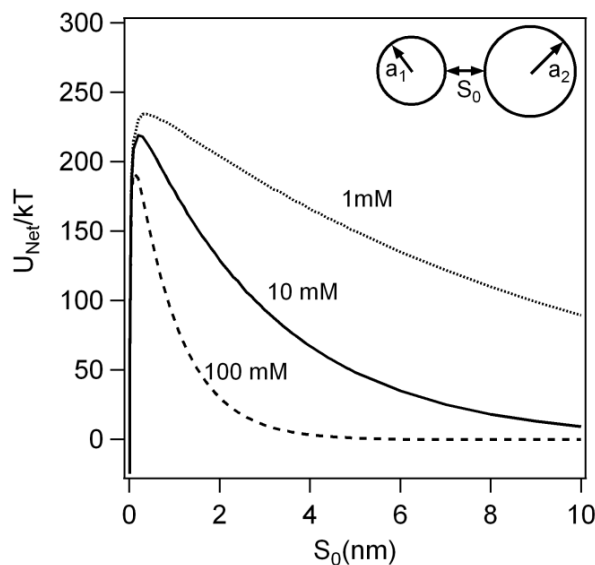


Figure 5.4. Interaction potential for a 2 μm hexadecane droplet and 40 nm PS latex particle at $\text{pH} = 7$ and increasing sodium chloride concentration as a function of their distance of closest approach, S_0 .

Under most solution conditions, the hexadecane drops and the PS latex particles have net negative surface charges that lead to electrostatic repulsion and can prevent spontaneous adsorption. Nevertheless, the energy barrier could be significantly reduced if this surface charge is neutralized or screened. Figures 5.2 and 5.3 suggest that decreasing pH is the most effective method to reduce the surface charge of both the dispersed oil and the PS particles. Hexadecane has a zeta potential of -95 mV at $\text{pH} = 7$ that is effectively neutralized by decreasing the pH to 2.5. Similarly, PS latex particles have a zeta potential of -70 mV that is reduced to just -35 mV at $\text{pH} = 2.5$. It is important to note that the zeta potential for both components in the dispersion varies differently with pH so that the net interactions will be a non-trivial function of solution conditions. Figure 5.5a shows the net interaction energy as a function of pH with a concentration of 1 mM NaCl in the solvent. Figures 5.2b and 5.3b also show that the zeta potential is dependent on salt concentration. Figure 5.5b shows that the energy barriers for adsorption are further

reduced with the addition of salt (30 mM NaCl) such that at pH = 2.5 the energetic penalty is a mere 0.5 kT. Therefore, one would expect that particle adsorption would be most effective at low pH and high salt concentrations. However, extremely high ionic strength can also be detrimental to particle adsorption. Figure 5.6 demonstrates that at high NaCl concentration, the net interaction energy between the PS particles becomes attractive so that they will aggregate in the dispersion before reaching the emulsion interface. Thus, dispersions of moderate ionic strength will allow for effectively stabilized particles to adsorb at the oil-water interface.

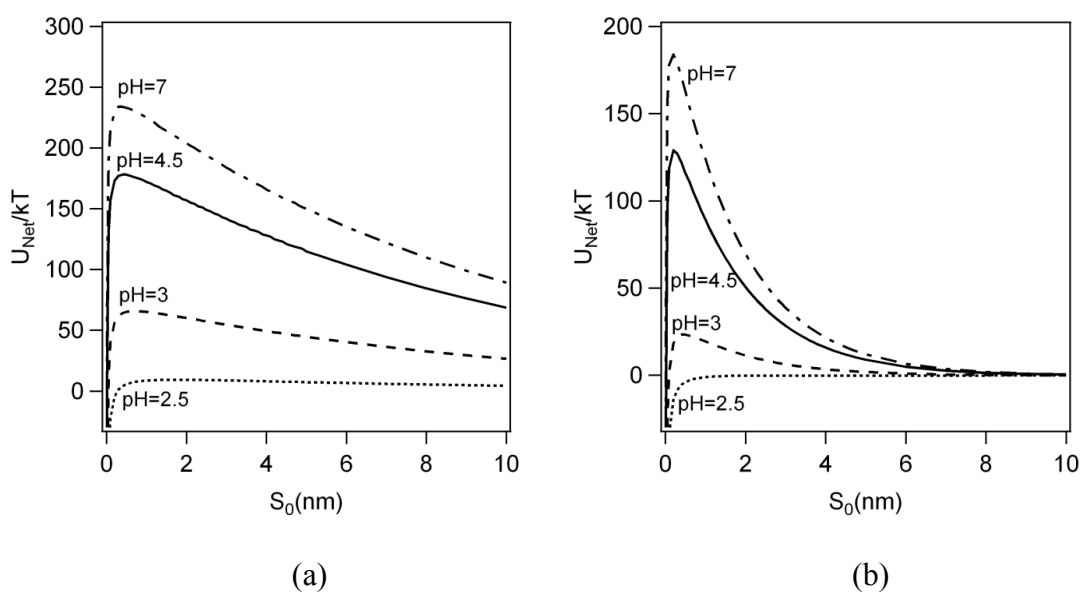


Figure 5.5. Interaction potential for a 2 μm hexadecane droplet and 40 nm PS latex particle at a) 1 mM NaCl and b) 30 mM NaCl as a function of their distance of closest approach, S_0 .

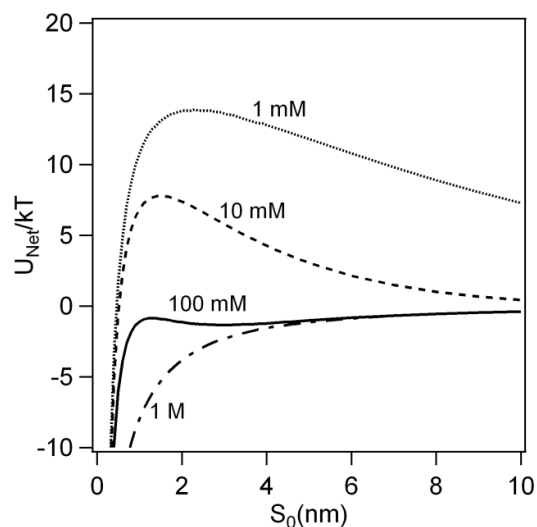


Figure 5.6. Interaction potential for two 40 nm PS latex particles at pH = 2.5 and increasing sodium chloride concentration as a function of their distance of closest approach, S_0 .

Given the importance of electrostatic interactions in these systems, we could also use them to enhance emulsification efficiency. The energy barrier that prevents particle adsorption in the PS system can be converted to a net attractive force through the use of positively charged particles and negative oil droplets. In Figure 5.7, the interaction potential for a 3 nm radius gold particle ($\zeta_1 = 10$ mV) and a 2 μm radius hexadecane droplet is calculated at several pH values. At neutral solvent conditions, the lowest energy is observed because the greatest difference in surface charge exists between the negative potential of the oil and the positive particles. However, a reduction in pH also reduces the magnitude of the negative surface charge in the oil and therefore reduces the net attraction.

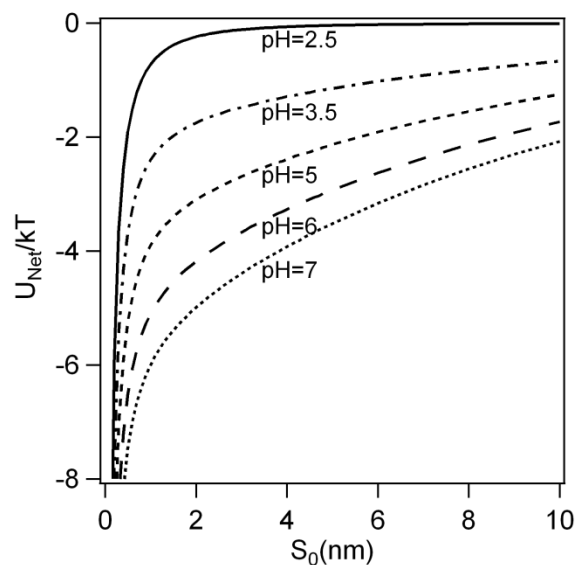


Figure 5.7. Interaction potential for a 2 μm hexadecane droplet and a 3 nm ammonium functionalized gold particle with 1 mM NaCl as a function of separation distance (S_0). The zeta-potentials of hexadecane are 0.5, -5, -25, -50 and -95 mV at pH 2.5, 3.5, 5, 6 and 7 respectively.

5.5 Measurement of particle adsorption at oil-water interfaces

5.5.1 Adsorption of polystyrene latex nanoparticles

A combined SANS and USANS study of emulsions prepared with PS latex particles was conducted using a recently developed model for Pickering emulsions.⁵⁸ The scattering model appropriately accounts for size polydispersity in the oil drops, which typically arises from mechanically forming the emulsion. At high q , the signal is dominated by the form factor of the particles while scattering at low q is controlled by the extent of particle adsorption and by the average oil droplet size. Figure 5.8 shows the entire scattering curve (SANS and USANS) for an emulsion prepared at 20 mM NaCl and pH = 2.5 and the corresponding fit to the Pickering emulsion model. The oil and water phases are contrast-matched to eliminate scattering contributions from the oil droplets. The best fit is achieved when the mean drop radius is $R_o = 1.97 \mu\text{m}$ with a

polydispersity of 0.4 (Gaussian distribution) and with 67.3% of the oil-water interface covered with adsorbed polystyrene latex particles. All other parameters ($\rho_w = \rho_o = 6.02 \cdot 10^{-6} \text{ \AA}^{-2}$, $\rho_p = 1.52 \cdot 10^{-6} \text{ \AA}^{-2}$, $R_p = 40.6 \text{ nm}$, $\delta = 0$, $\phi_o = 0.009$ and $\phi_p = 0.0014$) are held fixed during data fitting because they are known from the sample preparation or they are determined from independent neutron scattering measurements. Optical microscopy was also used to verify that the average drop size ($R_o = 2 \mu\text{m}$) remained constant over a one-week period as long as creaming was prevented via continuous sample rotation.

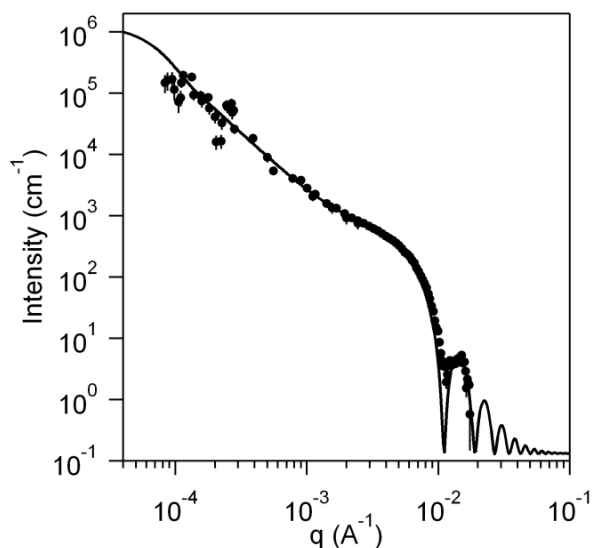


Figure 5.8. SANS and USANS data for 1 vol% hexadecane in water emulsion stabilized by 0.25 vol% 80 nm PS latex. Parameters of the model are $R_o = 1.97 \mu\text{m}$, $R_p = 40.6 \text{ nm}$, $\delta = 0$, $\phi_o = 0.009$, $\phi_p^T = 0.0014$, $\rho_w = \rho_o = 6.02 \cdot 10^{-6} \text{ \AA}^{-2}$, $\rho_p = 1.52 \cdot 10^{-6} \text{ \AA}^{-2}$, 67.3% surface coverage and a polydispersity index of 0.4.

Figure 5.9 shows SANS data for hexadecane-in-water emulsions at pH=7 and with increasing salt concentration. Upon increasing the ionic strength, a systematic upturn in the scattering at low q is observed that is indicative of increased particle adsorption at the hexadecane droplet interface. As expected from the interaction energy calculations, there is enhanced particle adsorption at higher salt concentrations due to the

screening of the electrostatic repulsion. Emulsions above 30 mM NaCl are unstable because the PS particles are found to uncontrollably aggregate on their own. This behavior is also verified with DLVO calculations in Figure 5.6. The maximum adsorption that could be achieved at pH 7 occurs at 30 mM NaCl (largest stable salt concentration) and corresponds to coverage of only 33.5% of the oil droplet area. This value is far from the maximum coverage (90%) that can be observed in ordered close-packed lattices formed from micrometer sized colloidal particles.¹⁰⁹ As demonstrated with DLVO theory, the decay-length of the repulsive potential preventing particle adsorption at an oil-water interface decreases with the addition of salt. The increased ionic strength causes the electrical double layer around the particles and oil to shrink and the van der Waals attractions and interfacial interactions begin to dominate.^{149, 150} The DLVO calculations suggest that a reduction of the surface potential in the particles and the oil is necessary to further increase the particle adsorption.

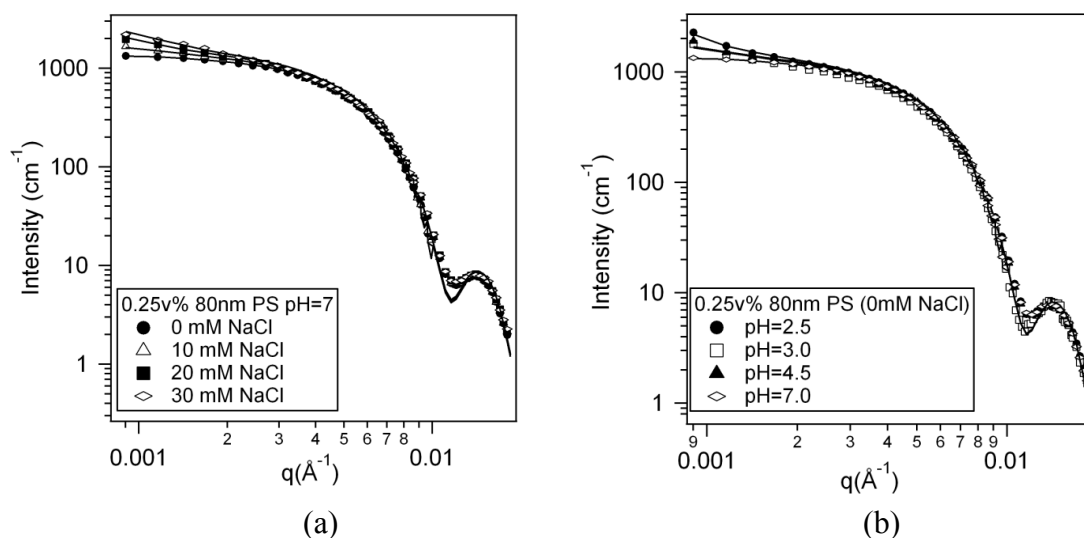


Figure 5.9. SANS data for 1 vol% hexadecane in water emulsion stabilized by 0.25 vol% 80 nm PS latex at (a) pH = 7 for varying NaCl concentrations and (b) 0 mM NaCl and varying pH. Lines correspond to the best-fit of the model for Pickering emulsions.

Figure 5.9b shows that pH changes can neutralize surface charges at the oil-water interface and at the particle surface leading to increased adsorption. As expected, there are systematic changes in the scattering curves at low q with the largest upturn occurring at the lowest pH values. It is important to note that the negative charge of the hexadecane-water interface effectively repels the negative particles away from the interface even when strong capillary interactions ($50,000 kT$) suggest that adsorption is very favorable. By neutralizing these charges particle adsorption events become increasingly more likely leading to larger surface coverage.

Using the results of all of the SANS experiments, we can create particle adsorption isotherms (Figure 5.10) as a function of pH and NaCl concentration. In general, low pH and high salt concentration lead to more particles at the interface. These trends agree very well with the interaction potentials that are calculated from DLVO theory. Therefore, it is shown that simple electrostatic and van der Waals interactions dominate the formation of Pickering emulsions when mechanical forces are absent or not strong enough to drive particles past these potential barriers. In this particular system, the pH of the solution is found to be the strongest factor to control particle adsorption. However, increases in NaCl concentration reduce the Debye length and the decay of the repulsive potential. Both of these effects make it more probable for a PS particle to adsorb at the hexadecane-water interface. Once particles reach this interface, other complex interfacial interactions will dominate their behavior and likely result in irreversible adsorption.

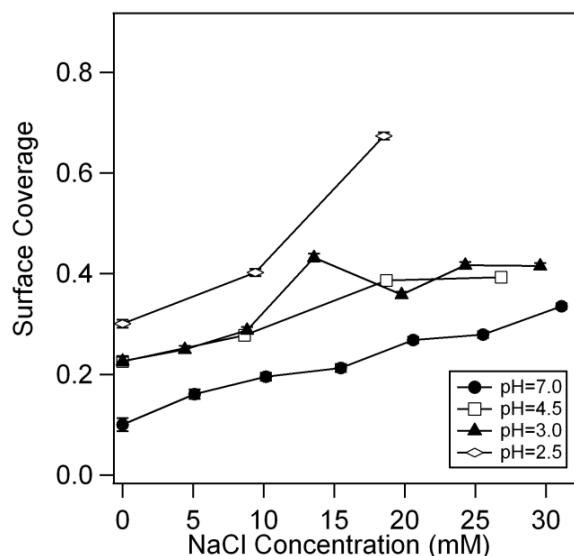


Figure 5.10. Particle adsorption isotherms calculated from SANS data for 0.25 vol% 80 nm PS latex 1 vol% hexadecane emulsions at varying ionic strength and pH.

5.5.2 Adsorption of cationic gold nanoparticles

The formation of Pickering emulsions from nanoparticles is significantly more challenging, when compared to micrometer particles, due to the lower adsorption energy. Typically a surface-active coating is essential to drive the particles into the interface. Here, cationic particles were synthesized to demonstrate that electrostatic attraction could also be used to generate particle stabilized emulsions via spontaneous adsorption. Figure 5.11a shows the SAXS patterns for a 0.2 vol% hexadecane emulsion stabilized by 0.002 vol% 6 nm mercaptoundecyl-trimethylammonium capped gold particles at pH 7. At these conditions the zeta potential of the particles and the hexadecane drops are 12 mV and -95 mV respectively. The particles were added to an existing hexadecane-in-water emulsion at time zero. After 5 minutes, the scattering curve is still identical to the particle form factor because the particles have not had sufficient time to migrate to the oil interface. As time elapses, an upturn at low q develops indicating that more particles are adsorbing at

the hexadecane-water interface. Additionally, a correlation peak develops at $q=0.078 \text{ \AA}^{-1}$ suggesting an ordered arrangement at the interface. In two dimensions, monodisperse spherical particles will usually arrange in hexagonal lattices. Since higher order peaks are not distinguished in the scattering, we assume a hexagonal arrangement in order to estimate the average inter-particle spacing. This is obtained approximately from the

position of the first diffraction peak by $D = \frac{4\pi}{\sqrt{3}q_{peak}} = 9.3nm$.¹⁵¹

In order to confirm the dominance of the electrostatic effects, a control experiment was also carried out at pH = 2.5 where the zeta potential of the particles remains at 12 mV but the hexadecane interface is effectively neutralized. Thus, these conditions are expected to decrease the electrostatic driving force for adsorption. The SAXS curves in Figure 5.11b show that the scattering curves of the emulsion remain identical to the particle form factor even after one week. This indicates that no particles are adsorbed to the hexadecane-water interface due to the lack of electrostatic attraction. This difference in adsorption between the two samples highlights the importance of considering the nanoparticle and oil droplet charges in the design of emulsification protocols.

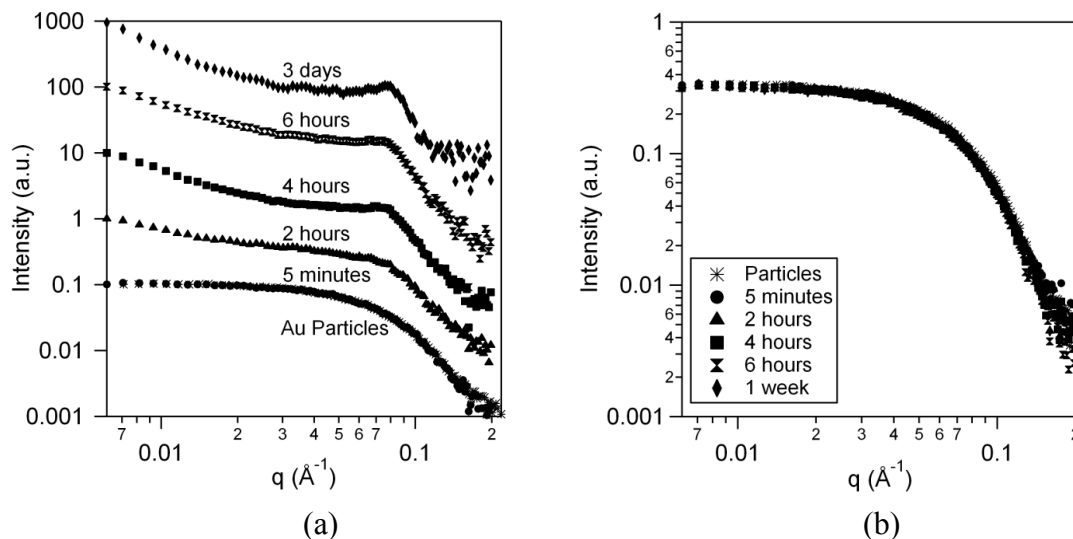


Figure 5.11. SAXS profiles for 0.2 vol% hexadecane in water emulsion stabilized by 0.002 vol% 6 nm ammonium capped gold particles at (a) pH = 7 and (b) pH = 2.5. The curves in (a) are shifted vertically for clarity.

5.6 Discussion

The method and solvent conditions used for generating a Pickering emulsion can have a clear impact on emulsion stability. In many applications, it may be necessary to add stabilizing particles after oil emulsification if, for example, the particles are susceptible to degradation due to heating during mechanical emulsification. In these cases, capillary forces may not be the primary driving forces for particle adsorption. Instead, it is electrostatic and van der Waals interactions that dominate particle adsorption at the oil-water interface. Through DLVO calculations and scattering studies, we show the charges on the oil drops and particles are critical to controlling particle adsorption. Because many organic oils are negatively charged in pure water at neutral pH, cationic particles more readily adsorb at the interface than anionic particles. This result is similar to the findings of Reincke and colleagues.¹¹⁸ They used anionic carboxylic acid functionalized gold particles that were dispersed in water with a macroscopic heptane layer. At pH = 9, the particles remained in the water phase because both the heptane interface and particles had

a negative charge. However, at low pH the charge on the particles is neutralized and they adsorbed at the heptane interface to form a film. This phenomenon is reversible and the particles disperse back into the water phase when the pH is increased back to 9. Reincke and colleagues attributed this behavior to a reduction in the surface charge density on the particles and its effect on the chemical potential for particles held at an interface.

However, these data are also consistent with our findings and also show that surface charges are critical considerations for particles approaching an oil-water interface.

There are some important limitations inherent to our simple DLVO calculations. Namely, in these calculations we assume that particles approach a bare oil-water interface. However, in most cases, particles will eventually adsorb onto an interface that is already populated by previously adsorbed particles. The adsorption of particles will continuously change the net surface charge of the interface and in this way also affect the subsequent adsorption of particles. The net interaction energy will actually be a complex function of the interface particle concentration and it may no longer resemble the interaction potential that was estimated for a bare interface. A natural extension of this work would be to incorporate the effect of adsorbed particles into the calculations of the interaction potential. This could give a more realistic estimate for the interaction potential of particles and oil drops over time and could allow modeling of the adsorption kinetics. Despite these simplifications, with SAXS experiments we clearly observe that particle adsorption of cationic gold particles continues to increase over time reaching high densities that are evident from the formation of a correlation peak. The fluid nature of the oil-water interface presumably allows particles to rearrange in order to pack more effectively. We expect that the adsorption process transitions from a diffusion-limited to

a reaction-limited process as the surface concentration of particles increases. This could play an important role in controlling particle arrangement at the interface and could allow the formation of a close-packed nanoparticle array. These ordered particle lattices are frequently documented in colloidosomes prepared from micrometer particles but have been significantly more challenging to produce from nanometer-scale particles due to the enhanced Brownian motion and weaker adsorption energy.^{6, 127}

5.7 Summary

The interaction of charged particles and hexadecane emulsion droplets has been carefully examined. For emulsions formed prior to particle addition, the interaction potential is a critical consideration when describing the spontaneous adsorption of particles at an oil-water interface. These potentials can be modeled with the classic DLVO theory and can be shown to correlate well to particle adsorption isotherms that are determined from small-angle scattering experiments. In the case of like-charged hexadecane and polystyrene particles, the potential is reduced by neutralizing the surface charge at low pH and by shrinking the electrostatic screening length with added salt. Conversely, positively charged gold particles are especially attracted to the hexadecane interface even though they are very small and have low attachment energy. These results demonstrate the importance of the particle and oil surface charges in describing the spontaneous adsorption of particles to an oil-water interface.

Chapter 6: Pickering Emulsions Stabilized by Nanoparticle Surfactants

Amphiphilic gold nanoparticles are demonstrated to effectively stabilize emulsions of hexadecane in water. Nanoparticle surfactants are synthesized using a simple and scalable one-pot method that involves the sequential functionalization of particle surfaces with polyethylene glycol (PEG) chains and short alkane-thiol molecules. The resulting nanoparticles are shown to be highly effective emulsifying agents due to their strong adsorption at oil-water and air-water interfaces. The original bare gold nanoparticles and PEG-functionalized particles without alkane-thiol are unable to effectively stabilize oil-water emulsions due to their small size and low adsorption energy. Small angle x-ray scattering and electron microscopy are used to demonstrate the formation of nanoparticle-stabilized colloidosomes that are stable against coalescence and show significant shifts in plasmon resonance, enhancing the near-infrared optical absorption. The work presented in this chapter has been published as a regular article in *Langmuir*. Reproduced in part with permission *Langmuir*, in press. Unpublished work copyright 2012 American Chemical Society.

6.1 Background

Solid gold nanoshells with a dielectric core are a novel class of optically tunable nanostructures that show remarkable promise in medical imaging and photothermal cancer therapy applications.¹⁵² The relative dimensions of the core radius and shell thickness can be tuned to absorb light over a broad spectral range due to the plasmon resonance of gold. The ideal structure will have a high absorbance in the near-infrared (NIR) wavelength region where blood and tissue are most transmissive as a result of low

scattering and absorption from intrinsic chromophores.¹⁵³⁻¹⁵⁵ When illuminated, the nanoshells serve as a localized heat source, photothermally inducing cell death in targeted tissues. The NIR absorbance of the nanoshells also makes them useful contrast agents in photoacoustic cell imaging applications.^{156, 157} Gold nanoshells are also easily functionalized with antibodies and other targeting ligands using gold-thiol covalent bonding. While these nanoshells are very effective, they are typically 100-200 nm in diameter, which is too large for clearance via the renal system. Therefore, accumulation of these nanoshells with the potential for long-term toxicity is a major obstacle for this technology.¹⁵⁸ In contrast, development of a composite colloidosome of gold nanoparticles that could disassemble when necessary may offer additional advantages and benefits in this regard.¹⁵⁹

The self-assembly of gold nanoparticles at emulsion interfaces could be utilized to form small composite nanoshell structures that are photoactive in the NIR region. These stable emulsion droplets will have a plasmon resonance comparable to solid gold nanoshells because of their similar shape. It is also possible to further tune the optical properties of these plasmonic emulsion materials by controlling the particle size and inter-particle spacing at the interface. Therefore, emulsions can be optimized for maximum NIR absorbance. The major benefit of using a composite colloidosome is that, after imaging or treatment, these could be designed to decompose into individual nanoparticles that could be naturally excreted from the body.¹⁶⁰ Another advantage of using armored emulsion droplets is the potential for vaporization of the oil phase. By selecting organic phases with adequate boiling points, we can control the maximum localized temperature that can be reached upon heating with NIR irradiation. When the

local temperature of the droplet exceeds the boiling point of the oil phase, the droplet will vaporize and expand to form a bubble. This could cause an increase in the inter-particle distance and reduce the surface plasmon resonance and NIR absorptivity. This control could prevent uncontrollable heating that could potential harm surrounding healthy tissue. A schematic representation of the organic phase liquid-vapor transition is shown in Figure 6.1.

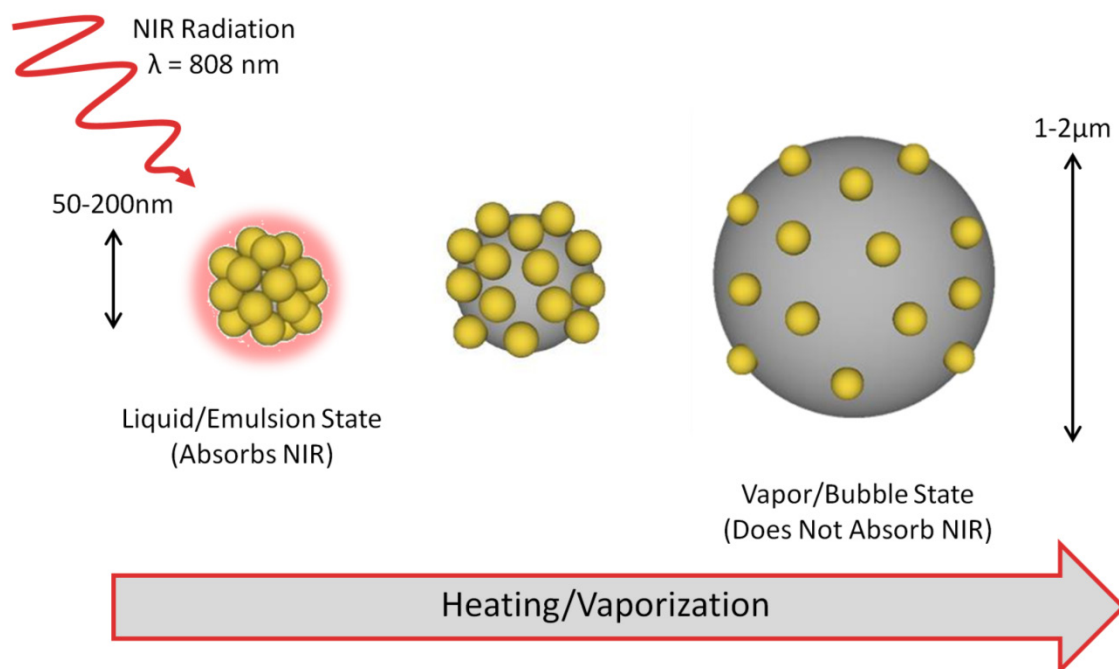


Figure 6.1. Schematic representation of the NIR induced liquid-vapor phase transition of composite plasmonic emulsions.

The ability to locally blow a controlled bubble also has potential applications in simultaneous photoacoustic (PA) and ultrasound (US) imaging. For this application, emulsion droplets will be generated from oil phases that have boiling points that are just higher than the internal body temperature (37 °C). In the same way as previously

described, the dispersed phase of the nanoparticle-stabilized emulsions will be vaporized by local NIR-induced heating of the plasmonic nanoparticles at the interface. This will cause the oil drop to expand and to form a large bubble with a lower mass density than the surrounding materials. In ultrasound imaging, the scattering of the incident sound wave is a strong function of the particle size and of the density difference with the surroundings. Therefore, one expects a large increase in ultrasound contrast upon formation of a bubble. A primary advantage of this approach over traditional US contrast agents is that the size of the original oil drops could be made to be one order of magnitude smaller than traditional bubble contrast agents ($> 1 \mu\text{m}$) so these could navigate more effectively throughout the vasculature. When the plasmonic emulsion is in the desired location, it can be ‘blown up’ via application of local NIR radiation to provide localized US contrast enhancement. In this chapter we will discuss the initial steps that we have been taken to produce ‘armored’ emulsions for use as advanced contrast agents in US and PA imaging.

As discussed in Chapter 5, the adsorption energy of nanoparticles at emulsion interfaces is usually similar to the energy of thermal fluctuations (kT) and this can severely limit their effectiveness as emulsion stabilizers. One way to improve the adsorption of nanoparticles to an oil-water interface is to modify the particle surface. Binks and colleagues showed an improvement in emulsion stabilization by functionalizing Fe_3O_4 nanoparticles with a carboxylic acid when compared with the adsorption of bare particles.¹⁶¹ Dinsmore et al. measured an increase in the binding energy of gold nanoparticles to oil-water interfaces after grafting mercaptoundecyl-tetra(ethylene glycol) to the gold surface.¹⁶² Another way to improve particle adsorption

to an interface is to graft surface-active polymers onto the particle surface. Abdulwahab showed with simulations that nanoparticles grafted with a purely hydrophilic polymer do not adsorb to an oil-water interface while particles grafted with amphiphilic block copolymers composed of at least 30% hydrophobic polymer will readily adsorb to an oil-water interface.¹⁶³ Tilton and coworkers also modified iron nanoparticles by grafting a poly(methacrylic acid)-poly(methyl methacrylate)-poly(styrenesulfonate) triblock copolymer to make them effective stabilizers of dodecane in water emulsions.¹⁶⁴ Similarly, they also grafted poly(2-(dimethylamino)ethyl methacrylate) onto silica nanoparticles that could be tuned to penetrate the oil-water interface to different extents.¹⁶⁵ While this elegant approach of polymerizing copolymers on the particles surfaces proved to be highly effective, the processes required for synthesizing tethered nanoparticles can be labor intensive and costly.

As described in Chapter 3, we have developed a simple, scalable and cost effective method for synthesizing gold nanoparticle surfactants that spontaneously self-assemble into clusters of controllable structure.⁶⁹ In this approach colloidal gold in water is first functionalized with thiol terminated poly ethylene glycol (PEG) through simple thiol chemistry. The long, bulky PEG-thiol chains sterically stabilize the particles in water. Subsequent functionalization with a short alkane-thiol renders the particles amphiphilic. The resulting particles are surface active and form rafts at the air-water interface and stable nanoparticle clusters in dispersion. These clusters are reminiscent of micelles formed from molecular surfactants with aggregation numbers that can also be accurately controlled by modifying the grafting density of the polymer on the nanoparticle surface. Like molecular surfactants, the nanoparticle surfactants are also

effective emulsifiers because of their amphiphilic nature. During the emulsification of oil with an aqueous dispersion of these clusters, the clusters readily break apart and particles adsorb to the oil-water interface. Figure 6.2 illustrates the preparation method for the nanoparticle surfactants and the hypothesized particle arrangement at the interface after emulsification. In this chapter, we demonstrate the effectiveness of these emulsifiers through the formation of stable emulsion droplets using several types of nanoparticle surfactants.

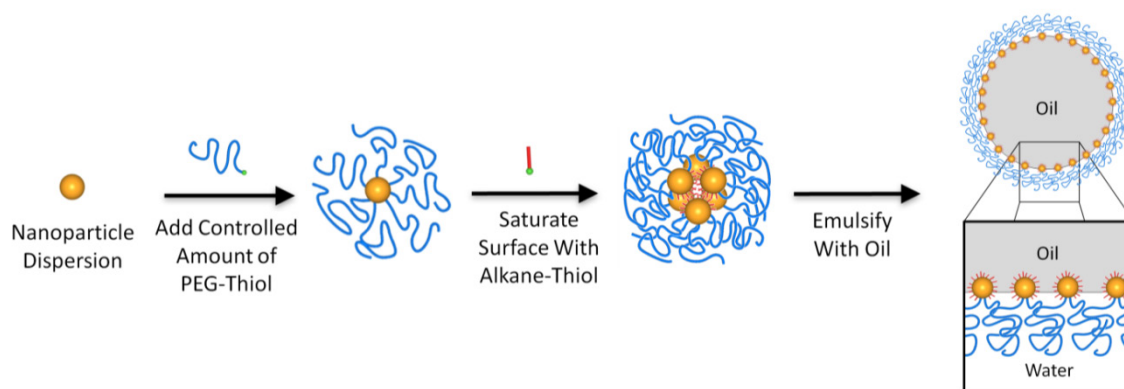


Figure 6.2. Schematic representation of the synthesis of nanoparticle surfactants and the stabilized oil-water emulsions. Particles are functionalized with a controlled amount of PEG-thiol (represented in blue) followed by saturation with a hydrophobic alkane-thiol (represented in red). Clusters spontaneously form in water dispersions. After emulsification with oil, nanoparticles adsorb to the oil-water interface with the alkane-functionalized portion of the particle exposed towards the oil phase.

6.2 Experimental Methods

Hexadecane, perfluorohexane, 2,2-dimethylbutane, sodium citrate, gold chloride trihydrate, butane-thiol, octane-thiol and dodecane-thiol are purchased from Sigma Aldrich (St. Louis, MO) and used as received. Thiol-terminated Poly(ethylene glycol) methyl ether (10 kDa) is obtained from Polymer Source (Dorval, Quebec Canada). Colloidal gold nanoparticles are synthesized using the citrate reduction method described

by Frens to produce 12 nm diameter particles that are approximately 0.02 wt% gold in an aqueous buffer.⁸² The particles are rendered amphiphilic by sequential functionalization with PEG-thiol and alkane-thiol using a process described in a previous publication.⁶⁹ The surface concentrations of PEG-thiol used in this study are 0.6, 0.8 and 1.8 chains/nm² Au as determined from thermogravimetric analysis (TGA). After functionalization, the particles are concentrated by pressurized diafiltration (Millipore) to a 0.47 wt% gold dispersion.

Hexadecane-in-water emulsions (1 vol% hexadecane and 0.02 vol% gold) are prepared using a Branson Digital Sonifier with a 102C microtip operated at 30% amplitude power that is pulsed one second on, one second off for one minute in the presence of particles. The UV-Vis spectroscopy is carried out using a Thermo Scientific Evolution 300 system in the visible and ultra-violet range (300-1100 nm). The size distribution of the emulsified oil drops is examined with a Zeiss Axiovert 40 CFL optical microscope at 40x magnification. The lyophilized oil droplet dispersions are also examined at a 15,000x magnification with a FEI Sirion Scanning Electron Microscope (SEM) operating at 5 kV. Oil droplets and clusters are also examined with a FEI Tecnai G2 F20 Transmission Electron Microscope (TEM) operating at 200 kV. Images are processed using ImageJ software developed at the National Institutes of Health.¹³⁹ Interfacial tension measurements are performed with a Kruss Tensiometer K12 equipped with a Wilhelmy slide.

Small-Angle X-ray Scattering (SAXS) is used to determine the particle arrangement before and after emulsification. SAXS experiments are performed in an Anton Paar SAXSess instrument (Graz, Austria) with a line-collimation system using a

Cu-K α source with a wavelength of 1.54 Å. The data are placed on an absolute scale by referencing to the scattering of pure water which is known to have an absolute scattering cross-section of 0.0162 cm⁻¹.¹⁶⁶ The scattering curves are subsequently desmeared using the Lake iterative method prior to data fitting with Igor macros developed at NIST.^{54, 57} The smeared scattering curves are also fit directly using the DANSE SansView software and both methods result in identical fit parameters.⁵⁵ SAXS experiments are performed on 0.01 wt% gold samples. The difference in scattering length density (SLD) of gold and water ($\Delta\rho_{Au-H_2O} = 1.14 \times 10^{-4} \text{ \AA}^{-2}$) is much greater than hexadecane and water ($\Delta\rho_{C_{16}H_{34}-H_2O} = 1.94 \times 10^{-6} \text{ \AA}^{-2}$), so the gold particles dominate the scattering.

6.3 Results and Discussion

6.3.1 Hexadecane Emulsions

Amphiphilic gold particles functionalized with PEG-thiol and alkane-thiol using the new synthesis scheme are shown to readily adsorb at a macroscopic hexadecane-water interface. The particles are surface active and can reduce the interfacial tension, similar to a small molecule surfactant. We measure the interfacial tension of our hexadecane and water to be 34.72 ± 0.32 mN/m. The interfacial tension value decreases to 28.05 ± 0.32 mN/m when 0.8 PEG chains/nm²Au and butane-thiol functionalized particles is added at extremely low concentrations (0.00005 vol% Au). The interfacial tension is also constant at much higher particle concentrations (up to 0.005 vol% Au). In addition, the interfacial tension values are also affected by the type of alkane-thiols that coats the nanoparticle surfactants. The interfacial tension of hexadecane and water in the presence of 0.005 vol% Au particles that are functionalized with 0.8 PEG chains/nm² Au

and octane-thiol or dodecane-thiol is 29.80 ± 0.29 mN/m and 31.12 ± 0.28 mN/m respectively. This shows that shorter alkane-thiol chains reduce interfacial tension to a larger extent implying that they are more surface active.

In this study we examined Pickering emulsions composed of 1 vol% hexadecane and 0.02 vol% amphiphilic gold particles in water at neutral pH. The formation of particle-stabilized oil droplets from nanoparticle surfactants containing 0.8 PEG chains/nm²Au and butane-thiol on the surface is confirmed with several microscopy techniques. Optical microscopy of a dilute emulsion shows many small stable droplets that are approximately 1 μm diameter (Figure 6.3a). Smaller drops could also be present but these would not be visible with simple optical microscopy. Scanning electron microscopy (SEM) has a higher magnification that allows closer examination of nanoparticle-stabilized emulsion droplets. Unfortunately, the samples had to be dried prior to analysis with electron microscopy. Freeze-drying (lyophilizing) was used to dry the samples while preventing the complete destruction of the interfacial particle structures so that these could be imaged. In Figure 6.3b we see that the droplets are partially deflated and fractured from the drying process, but the particles still retain their shell structure after the hexadecane and water have fully evaporated. Only one representative droplet is shown here, but tens of similar droplets were imaged using this approach. Finally, transmission electron microscopy (TEM) is also shown in Figure 6.3c. This technique also shows collapsed droplets with parts of the shell structure still evident. However, the higher resolution of TEM also allows imaging of the individual gold particles at the interface. TEM is also used to examine the structure of the particle clusters that form in water (analogous to surfactant micelles) before emulsification. While

there is a clear distribution of cluster sizes, the most abundant cluster geometry for the 0.8 PEG chains/nm²Au and butane-thiol functionalized particles is that of a trigonal dipyramid structure with five particles in each cluster. One of these representative clusters is also shown in Figure 6.3d.

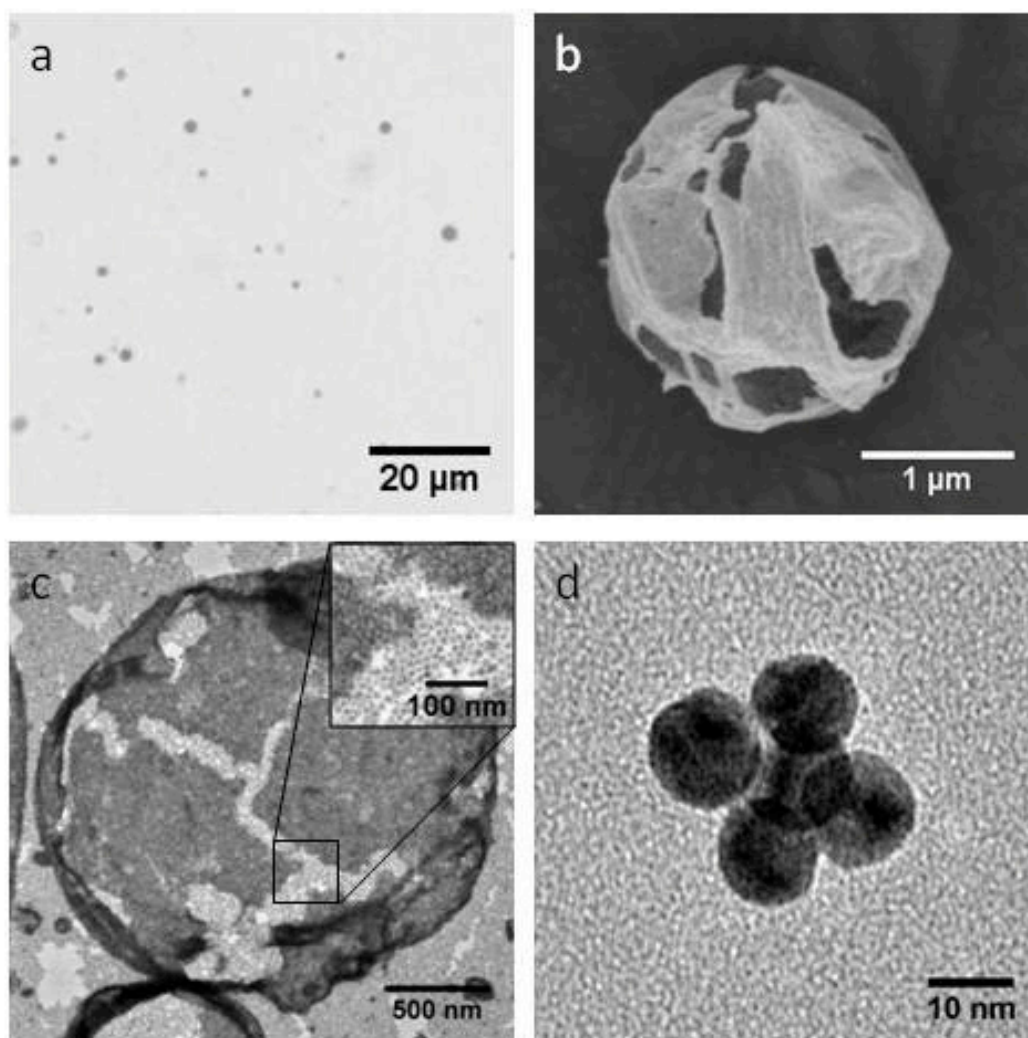


Figure 6.3. Micrographs of a 0.01 vol% hexadecane in water emulsion stabilized by 0.8 PEG chains/nm²Au and butane-thiol functionalized amphiphilic gold nanoparticles taken with a) optical microscopy, b) scanning electron microscopy and c) transmission electron microscopy. d) Characteristic particle cluster observed with transmission electron microscopy.

UV-Vis spectroscopy gives further information about the relative particle arrangement in the dispersed emulsions. Colloidal gold exhibits a unique absorbance spectrum that is dependent on the particle size and shape due to surface plasmon resonance.^{167, 168} The characteristic peak for 12 nm bare gold particles occurs at 520 nm and this is red-shifted when particles are in close proximity to each other. Figure 6.4a shows UV-Vis absorbance measurements for PEG-functionalized particles before (individual particles) and after (multi-particle clusters) butane-thiol functionalization and for hexadecane emulsions stabilized with the nanoparticle surfactants. The peak absorbance for particles with 0.8 PEG chains/nm² Au prior to butane-thiol addition occurs at a wavelength of 522 nm and appears red in color as shown in Figure 6.4b. The slight shift in absorbance peak occurs because of a change in the local refractive index around the particles due to the bound PEG chains surrounding the particles. After the addition of butane-thiol, the particles are amphiphilic and the absorbance peak shifts more significantly to 536 nm with the dispersion now appearing purple. This occurs because the particles are organized into small clusters and the plasmon resonance of particles couple with neighbors within the cluster to shift the resonant wavelength.¹⁶⁸⁻¹⁷⁰ Finally, the absorbance peak broadens and shifts dramatically to 680 nm when the particles are emulsified with hexadecane indicating that the particles are close-packed and form a dense shell at the emulsion interface. Figure 6.4c shows a picture of the concentrated emulsion with light illuminating the sample from behind (transmitted) and from the front (reflected). This demonstrates the deep blue color acquired by the emulsion due to the increased absorption of red light and also the metallic sheen that is a clear indication that particles are close-packed at the oil-water interface.

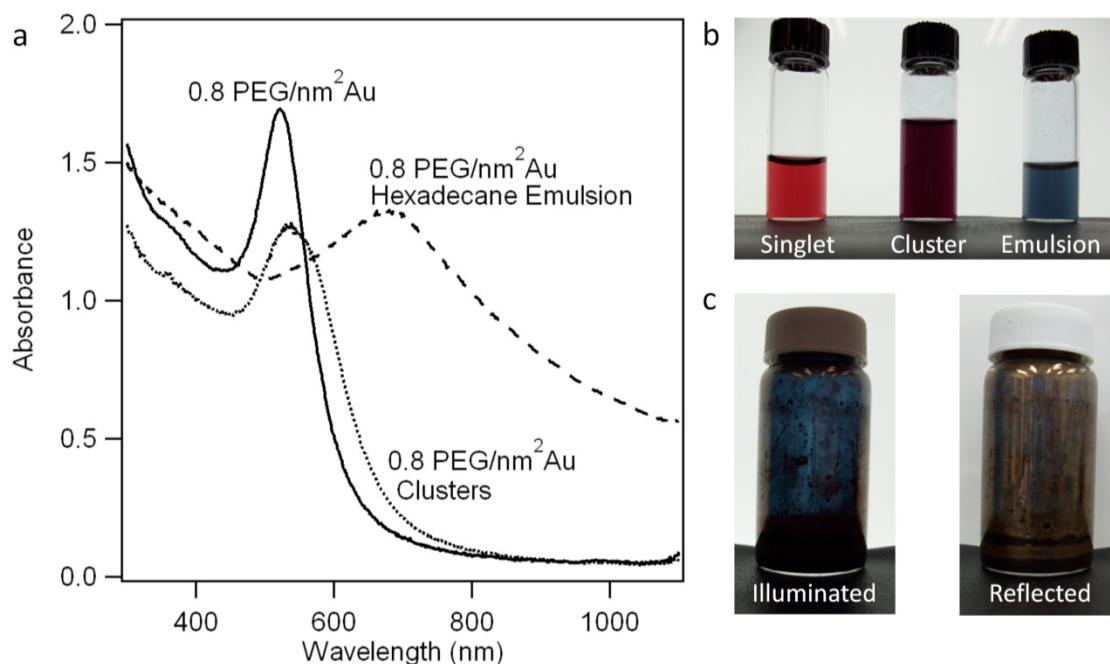


Figure 6.4. a) UV-Vis absorption spectra of gold nanoparticles functionalized with 0.8 PEG chains/nm² Au before and after butane-thiol functionalization and after emulsification with hexadecane. b) Photograph demonstrating the color shift of PEG-functionalized singlet particles, clustered nanoparticle surfactants and emulsions stabilized by the nanoparticle surfactants. c) Photographs of a concentrated particle-stabilized emulsion with light transitted through and reflected.

Small-angle x-ray scattering (SAXS) is also used to examine the nanostructure and particle arrangement in the emulsions directly in the dispersed state without solvent removal. Due to the large scattering contrast between gold and water relative to hexadecane-water and PEG-water, the scattering measured with SAXS originates primarily from the shape and arrangement of the gold nanoparticles. Figure 6.5 shows the desmeared scattering curves for bare particles, clustered particles and emulsified particles. The curves are shifted vertically by factors of 10 (clusters) and 10⁴ (emulsion) to help the reader distinguish between curves. The desmeared data are shown here so that the correlation peak positions can be determined directly. However, the fits are also

performed on the original smeared scattering data in an absolute scale by properly accounting for smearing due to the line-collimation system. The curve for the bare particles is fit using a spherical particle model resulting in a particle radius of 6.11 nm. The scattering length densities and volume fractions are known and held constant ($\phi_p = 0.00024$, $\rho_w = 9.46 \times 10^{-6} \text{ \AA}^{-2}$ and $\rho_p = 1.25 \times 10^{-4} \text{ \AA}^{-2}$).

A predicted scattering curve for the clustered particles is calculated using the classic Debye model.⁸⁷ The scattering profiles for the various cluster types can be calculated from simple geometric models as we have previously done and discussed in detail in Chapter 3.⁶⁹ TEM micrographs indicate the most abundant cluster geometry for this sample is a five particle trigonal dipyrmaid. However, from TEM data we can also measure the distribution of sizes in terms of the number of primary particles in each cluster. The experimental scattering curve of the cluster dispersions can then be predicted by weighting the calculated curves for each cluster geometry with a population histogram generated from the TEM data. The resulting calculated scattering curve matches the experimental data closely without any data fitting.

Finally, the scattering curve of the particle-stabilized emulsion is fit with a model that was recently developed specifically for Pickering emulsions.⁵⁸ The best fit of the data is achieved when a mean oil droplet radius of 494 nm is used with a polydispersity index of 0.1 (Gaussian distribution) and with 88.0% of the oil-water interface covered with adsorbed amphiphilic gold particles. All other parameters ($\rho_w = 9.46 \times 10^{-6} \text{ \AA}^{-2}$, $\rho_o = 7.52 \times 10^{-6} \text{ \AA}^{-2}$, $\rho_p = 1.25 \times 10^{-4} \text{ \AA}^{-2}$, $R_p = 6.11 \text{ nm}$, $\delta = 0$, $\phi_o = 0.01$ and $\phi_p = 0.00024$) are held fixed during data fitting because they are known from the sample preparation or they are determined from independent x-ray scattering measurements.

Additionally, there are slight deviations compared to the bare particle curve in the high q region that is typically dominated by the individual particle size and shape. These deviations arise from in-plane correlations of particles located at the oil droplet interface. Moreover, in this region the data shows a broad correlation peak that is located at approximately $q = 0.55 \text{ nm}^{-1}$ suggesting that some degree of lateral order is present at the interface. While the Pickering model is not able to account for in-plane particle correlations, we can still use the rough location of the broad diffraction peak to approximate the inter-particle spacing at the interface. Assuming a hexagonal arrangement, we estimate the inter-particle distance by the position of the first diffraction peak using $D = \frac{4\pi}{\sqrt{3}q_{peak}} = 13.2 \text{ nm}$.¹⁵¹ This distance is on the order of a particle diameter, which should also correspond to the inter-particle distance for close-packing. However, it should be noted that this is only a rough approximation because the exact peak position is difficult to determine from the broad peak.

From the fit parameters we can also calculate that only 10.5% of all the particles in the sample are located at the oil-water interface. This suggests that potentially more particles could have adsorbed to an oil-water interface if there was more room available. Thus, it could also be possible to stabilize higher concentrations of oil or smaller oil droplets (i.e. more total interface) if it were possible to generate smaller droplets via sonication or with other emulsification methods. Nevertheless, another possible explanation for the low adsorption value could also be that there is a dynamic equilibrium between particles in the bulk and the interface. Yet, we find that the average size of the oil droplets remains constant when varying the relative concentrations of both oil and particles. Emulsions with 1 vol% hexadecane and varying amounts of gold (0.0005 vol%

Au, 0.00025 vol% Au and 0.0001 vol% Au) all result in oil droplet radii of ~ 500 nm as measured by DLS. Therefore, the results suggest that it is the mechanical forces of the sonication process that limit the total amount of interface that can be generated.

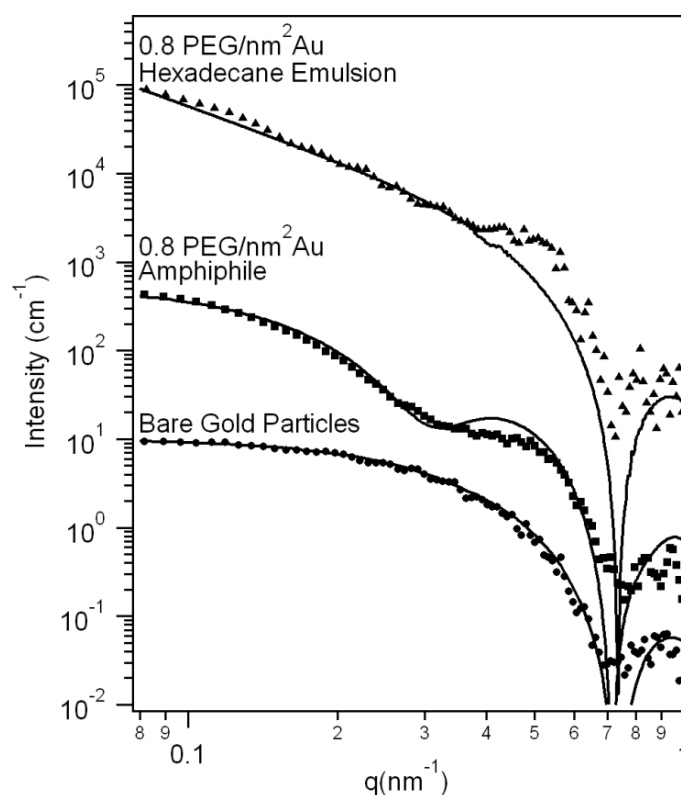


Figure 6.5. Desmeared SAXS data for bare gold nanoparticles, clustered amphiphilic gold nanoparticles in water and emulsified amphiphilic gold nanoparticles. The bottom curve is scattering from bare gold particles in water which is fit by a spherical model with $R_p = 6.11$ nm, $\phi_p = 0.00024$, $\rho_w = 9.46 \times 10^{-6} \text{ \AA}^{-2}$ and $\rho_p = 1.25 \times 10^{-4} \text{ \AA}^{-2}$. The middle curve (shifted by a factor of 10 for clarity) is the scattering data for a nanoparticle surfactant cluster in water and the modeled scattering curve calculated using the Debye equation. The top curve (shifted by a factor of 10^4) is for a 1.0 vol% hexadecane in water emulsion stabilized by 0.024 vol% 6.11 nm amphiphilic gold particles. Parameters of the model are $R_o = 494$ nm with a polydispersity index of 0.1 (Gaussian distribution), $R_p = 6.11$ nm, $\delta = 0$, $\phi_o = 0.00998$, $\phi_p^\dagger = 0.00024$, $\rho_w = 9.46 \times 10^{-6} \text{ \AA}^{-2}$, $\rho_o = 7.52 \times 10^{-6} \text{ \AA}^{-2}$, $\rho_p = 1.25 \times 10^{-4} \text{ \AA}^{-2}$, 88.0% interface coverage.

Nanoparticle surfactants with varied PEG-thiol concentrations and different alkane-thiols will also effectively stabilize emulsions but to different extents. In addition to inducing adsorption, the alkane-thiol length and the surface PEG-thiol concentration

also control how closely the particles are able to pack when located at the interface.

Figure 6.6a shows the absorbance spectra for emulsions stabilized by particles with 0.6 PEG chains/nm²Au and different alkane-thiols. It is clear that, when the length of the alkane-thiol shrinks, the peak absorbance red-shifts to higher wavelengths. This indicates that the particles are more closely packed at the interface allowing for stronger coupling between surface plasmons in adjacent particles.¹⁷⁰ Particles containing PEG-thiol but without alkane-thiol are not able to stabilize an emulsion and the spectra is identical to that of the particles in water prior to emulsification. Although the samples were initially turbid, the samples recovered the original spectra after the emulsion droplets coalesced. Figure 6.6b shows the wavelength of the peak absorbance plotted as a function of the surface concentration of PEG-thiol and the type of alkane-thiol. For all PEG-thiol loadings, emulsions using the butane-thiol particles (circles) have the largest shift in absorbance wavelength while the dodecane-thiol particles (squares) result in emulsion with the smallest shift. The PEG-thiol concentration on the nanoparticle surface also causes slight changes in the absorbance where higher concentrations result in a smaller peak shift due to larger steric interactions between neighboring particles. Furthermore, nanoparticle surfactants having the highest polymer concentration (1.8 PEG chains/nm²Au) stabilize emulsions despite being ‘singlets’ in water. In other words, the steric hindrance prevents the particles from forming clusters in dispersion but it does not prevent their adsorption at oil-water interfaces.

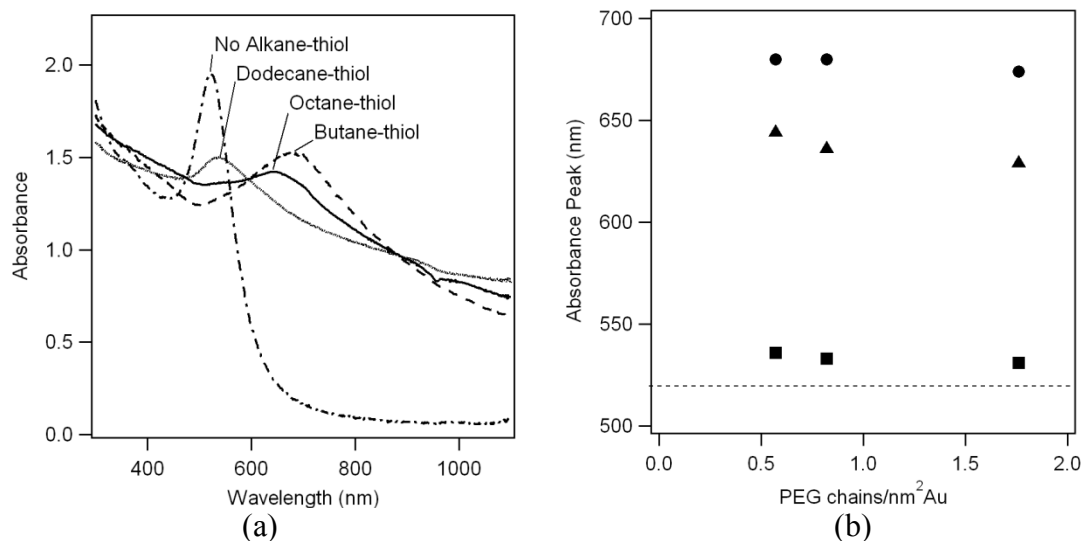


Figure 6.6. a) UV-Vis spectra of 1 vol% hexadecane in water emulsions stabilized by nanoparticle surfactants with 0.6 PEG chains/nm²Au and different alkane-thiols. The curves are normalized by the total particle concentration in each sample. b) Absorbance peak plotted as a function of PEG-thiol concentration for butane-thiol (circles), octane-thiol (triangles) and dodecane-thiol (squares) where the dotted line is the absorbance for bare gold particles.

SAXS allows us to directly quantify particle adsorption at the oil droplet interface and values are found to be quite high. The scattering curves for all samples, containing different polymer concentrations and alkane-thiol lengths, are also fit using the Pickering emulsion model as demonstrated previously in Figure 6.5. The scattering length densities and oil and particle volume fractions are held fixed as before, but the particle radii are 6.55 nm for the 0.6 and 1.8 PEG chains/nm²Au nanoparticle surfactants because a different batch of particles was used. All fits result in an oil droplet radius of 498 ± 2 nm and a polydispersity index of 0.1 (Gaussian distribution) but with varying nanoparticle surface coverage. Examples of the scattering curves and data fits are shown in Figure 6.7a for the 1.8 PEG chains/nm²Au particle emulsions. The increasing slope with decreasing alkane-thiol length at low q indicates that more particles cover the oil-water interface for shorter thiols. We also clearly see that particles with PEG-thiol but without

alkane-thiol functionalization do not show any interfacial particle adsorption and the emulsion is therefore unstable. The percentage of the oil surface area that is covered with particles is plotted as a function of PEG-thiol concentration for various nanoparticle surfactants in Figure 6.7b. The particles with 0.6 PEG chains/nm²Au and butane-thiol result in the highest interface coverage (88.5%) at a hexadecane-water interface, which nearly reaches the limit of hexagonally closed-packed particles (90%). Using particles with the same PEG-thiol loadings but with octane-thiol or dodecane-thiol, causes the percent interface coverage to reduce to 75.4% and 50.0% respectively. This corresponds to an increase in the average gold particle spacing of 0.5 nm and 2.1 nm relative to emulsions stabilized with butane-thiol. The measured difference between butane-thiol monolayer film thicknesses on flat substrates and those of the longer alkane-thiols is approximately 0.5 nm (octane-thiol) and 1.3 nm (dodecane-thiol).⁸⁵ This correlates well with the spacing differences calculated from scattering suggesting that the small thiol ligands are acting as spacers between particles. However, this trend breaks down at higher PEG-thiol loadings. Particles with 1.8 PEG chains/nm²Au and dodecane-thiol adsorb strongly to the interface but have a significantly lower interface coverage value (34.6%). This suggests that these surfactant nanoparticles are effective emulsifiers, but the gold only covers a small area of the total interface because of lateral repulsion between particles.

We also observe a clear correlation between the packing density measured with SAXS and the absorbance shift in the spectroscopy data. Emulsions formed with butane-thiol nanoparticle surfactants have the highest particle packing at the interface and this results in a spectrum where the main plasmon peak is red-shifted by the largest extent.

The butane-thiol nanoparticle surfactants have the most efficient packing because they have the shortest alkane chain length. Additionally, we can tune the packing at the interface by controlling steric hindrance through variations in the PEG-thiol concentration. By modifying the inter-particle spacing of particles at the interface, we can thus tune the UV-Vis absorption spectra. This is particularly important in emerging applications such as photothermal therapy where we must carefully engineer absorbance in the NIR region for optimal heating.

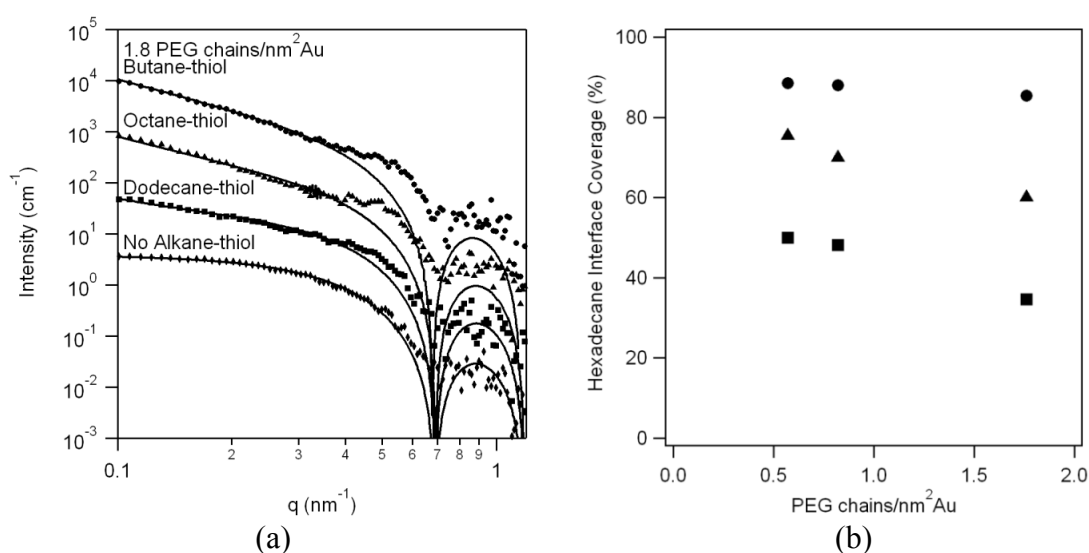


Figure 6.7. a) SAXS data and fits to the Pickering emulsion model for 1 vol% hexadecane in water emulsions stabilized by surfactant nanoparticles containing 1.8 PEG chains/nm²Au and different types of alkane-thiol molecules. Parameters of the model are $R_o = 498$ nm with a polydispersity index of 0.1 (Gaussian distribution), $R_p = 6.55$ nm, $\delta = 0$, $\phi_o = 0.0998$, $\phi_p^T = 0.00024$, $\rho_w = 9.46 \times 10^{-6} \text{ \AA}^{-2}$, $\rho_o = 7.52 \times 10^{-6} \text{ \AA}^{-2}$, $\rho_p = 1.25 \times 10^{-4} \text{ \AA}^{-2}$. The butane-thiol emulsion (shifted by a factor of 10^3), octane-thiol emulsion (shifted by a factor of 10^2), dodecane-thiol emulsion (shifted by a factor of 10) and no alkane-thiol emulsion are best fit with a 85.5%, 60.0%, 34.6% and 0% interface coverage respectively. b) Percent interface coverage plotted as a function of PEG-thiol concentration for butane-thiol (circles), octane-thiol (triangles) and dodecane-thiol (squares).

Bare gold nanoparticles and PEG-functionalized particles without alkane-thiol do not adsorb at the oil-water interface nor do they exhibit any emulsification properties.

The UV-Vis spectra and x-ray scattering curves are identical before and after

emulsification in the presence of bare particles and no stable oil droplets are observed with microscopy. Conversely, the data clearly show that the nanoparticle surfactants are stabilizing the hexadecane in water emulsion, and they are adsorbed at the oil-water interface. This is significant because it indicates that the self-assembly of particles at an interface can be tuned through a simple functionalization protocol to form nanoparticle surfactants. Particle adsorption at oil-water interfaces has previously been demonstrated using particles grafted with amphiphilic block copolymers.^{164, 171} Our approach, however, does not require costly or time-consuming polymerization and purification steps. Furthermore, the particle packing density can be tuned through the formulation of different types of nanoparticle surfactants.

6.3.2 Low Boiling Point Oil Emulsions

One of the unique benefits of forming a composite gold nanoshell around an oil droplet core is the potential to vaporize the oil phase for controlled heating and ultrasound contrast enhancement. However, for this application, the organic phase must be chosen carefully. The boiling point must be higher than body temperature so that the oil only vaporizes upon external irradiation, but also low enough so that the heat generated from NIR absorbance is sufficient to drive vaporization. Additionally, the toxicity of the organic phase is an important consideration for biomedical applications.

Emulsions for this study are generated by two methods, sonication and extrusion. In the first method, the organic phase is sonicated with water in the presence of nanoparticle surfactants with sequential pulses (one second on, four seconds off) for a total of one minute at a 30% power amplitude. The intermittent pulsing is used to

prevent oil evaporation due to excessive heating that can occur during sonication. In the second method, the oil and water are sonicated for five seconds and then passed through a 200 nm pore extrusion filter to control the size of the final oil droplets. The extruded emulsion is then added to the particle dispersion, requiring spontaneous adsorption of the nanoparticle surfactants. It is not possible to extrude Pickering emulsions directly because the particles adsorb to the polycarbonate filter.

Due to its boiling point ($T_B = 50\text{ }^\circ\text{C}$), 2,2-dimethylbutane is tested as a possible vaporizable hydrocarbon oil. Dilute 0.5 vol% 2,2-dimethylbutane emulsions are generated using 0.001 vol% gold with a dose concentration of 5 PEG chains/nm²Au and 700 butane-thiol molecules/nm²Au. Neither of the emulsion preparation methods resulted in stable droplets that are visible with optical microscopy. However, many of the particles form large aggregates in dispersion. This unexpected result is related to the dilute nature of the emulsions that are used (0.5 vol%). The solubility of 2,2-dimethylbutane in water at room temperature is 2 wt%. This exceeds the concentration that is used in the emulsification process.¹⁷² Thus, all of the oil is eventually dissolved into the dispersed phase and stable emulsion droplets cannot be formed in dilute conditions. For the intended application, a dilute suspension of the plasmonic emulsions is a key requirement. Thus, it is essential to utilize oils that are much more insoluble in water.

Perfluorohexane is insoluble in water (solubility < 10 ppm) and also has an adequate boiling point of 60 °C.¹⁷³ When emulsified with water by extrusion through 200 nm membrane and subsequent addition of the nanoparticle surfactant, the particles are not able to adsorb strongly at the oil-water interface. This is indicated by the UV-Vis

absorbance spectrum that is shown in Figure 6.8a. The absorbance in the NIR region is low, suggesting low particle concentrations at the interface. Similarly, the small angle x-ray scattering curve of the emulsion (Figure 6.8b) is almost identical to the scattering of bare gold particles. This suggests that the nanoparticle surfactants may not be able to spontaneously adsorb to the oil-water interface and that they must be mechanically forced to the interface.

A 0.5 vol% perfluorohexane emulsion is also generated through sonication in the presence of 0.001 vol% nanoparticle surfactants that are functionalized with a dose concentration of 5 PEG chains/nm²Au and with excess butane-thiol as described in Chapter 3. Small angle x-ray scattering and UV-Vis spectroscopy both indicate that these particles are singlets in dispersion prior to emulsification. When sonicated with perfluorohexane, a stable emulsion is formed with an average oil droplet diameter of 140 nm as determined by dynamic light scattering (DLS). The particles adsorb strongly to the interface, resulting in increased NIR absorbance that arises from the plasmon resonance of the coupled particles. Additionally, the SAXS curve from the emulsion has a significant slope at low q that indicates effective particle adsorption to the oil-water interface. The slight development of a correlation peak at $q = 0.55 \text{ nm}^{-1}$ also suggests that some in-plane ordering is occurring.

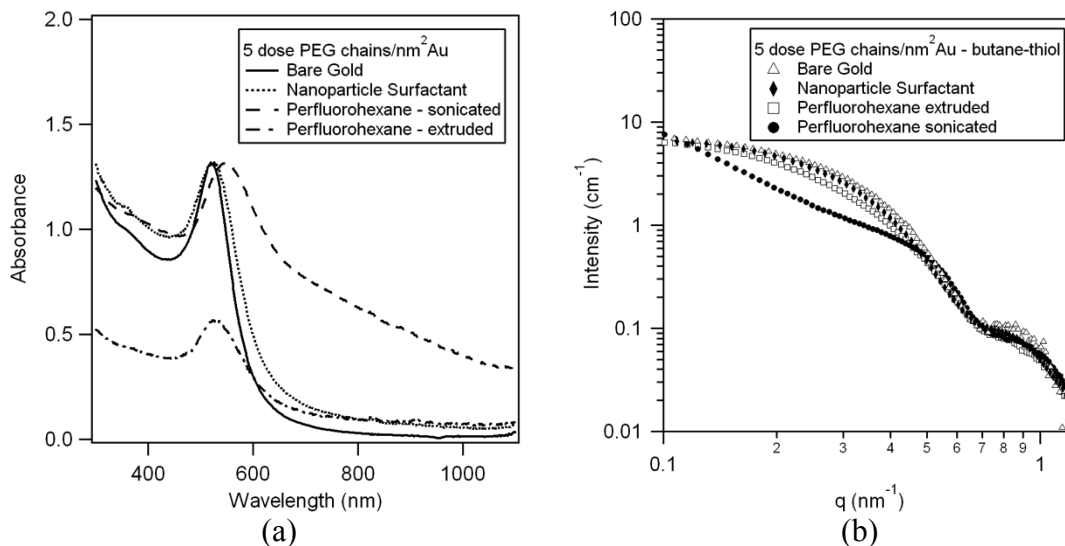


Figure 6.8 a) UV-Vis absorption spectra and b) smeared SAXS data for 0.001 vol% bare gold particles, gold nanoparticles functionalized with a dose of 5 PEG chains/nm² Au and a large excess of butane-thiol and for emulsions of these particles with 0.5 vol% perfluorohexane.

An optical micrograph of the stable emulsion at room temperature taken at 40x magnification is shown in Figure 6.9a. Additional small droplets are visible through the eye piece but these are smaller than the resolution limit of the camera. Still, the micrograph shows many individual droplets. The sample is then heated to 70 °C directly in the microscope slide with the use of a heat gun. Many of the oil droplets expand by approximately one order of magnitude as seen in Figure 6.9b. This indicates the oil droplets are vaporizable if sufficient heat is applied.

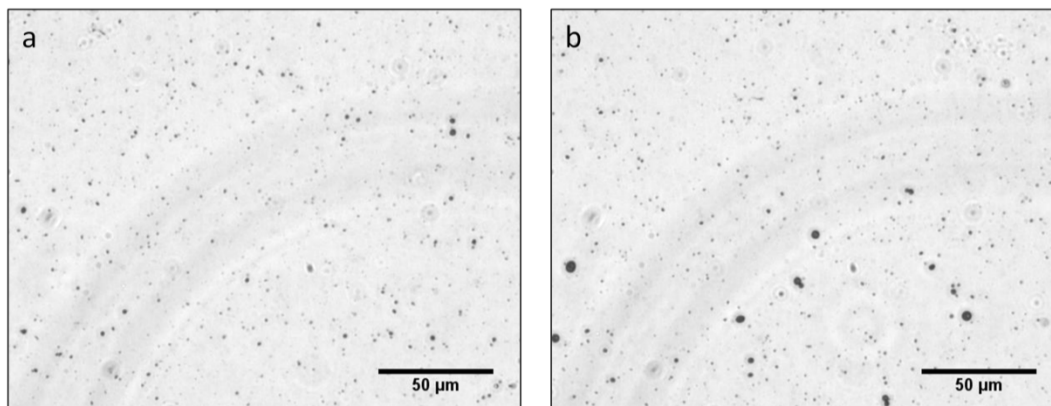


Figure 6.9 Optical microscopy of a 2.8 vol% perfluorohexane emulsion stabilized by 0.2 vol% gold nanoparticles functionalized with 5 dose PEG chains/nm² Au and butane-thiol at a) 21 °C and b) 70 °C.

Through collaboration with the O'Donnell group in Bioengineering, the perfluorohexane emulsions are also evaluated for use as contrast agents in US and PA imaging. The sonicated perfluorohexane emulsion is irradiated with NIR light while simultaneously measuring the ultrasound and photoacoustic signals. The dispersed nanoparticle surfactant emulsion nanostructures are loaded into a 1 mm diameter polytetrafluoroethylene optically transparent tube that is immersed in a water tank. The radiation source is a variable wavelength pulsed laser operating at $\lambda = 810$ nm, 4.5 mJ and 20 Hz pulses, resulting in an average power output of 90 mW spread over an area that is 3-5 mm in diameter. An ultrasound transducer simultaneously acquires the photoacoustic signal and ultrasound pulse-echo imaging. The details of the experimental setup are located in Appendix B. Figure 6.10 shows snapshots of the photoacoustic signal (Figure 6.10a) and ultrasound signal (Figure 6.10b) after the sample has been irradiated for 1.10 seconds. The bright orange color in the photoacoustic measurement will be strongest when the NIR absorbance is highest and the particles are in close contact. Conversely, the backscattered ultrasound signal increases when there are large density differences in

the sample and when the size of the dispersed objects is larger. Therefore, this should correspond to oil vaporization. Figure 6.11 shows the change in the integrated intensity signal as a function of time irradiated. The signal is integrated over the yellow boxes denoted in Figure 6.10. Interestingly, we see definite increases in the photoacoustic signal once the sample is irradiated by the laser. Similarly, there is a sharp increase in the ultrasound signal suggesting that bubbles are forming. There are also some very interesting changes in the signal over time, but much more work is required to fully interpret the meaning of these changes. Still, these exciting results demonstrate that plasmonic emulsions have significant potential for success in medical imaging and photothermal therapy applications. Despite this early success, the system requires significant optimization for specific applications and should be a major thrust for ongoing research in this field.

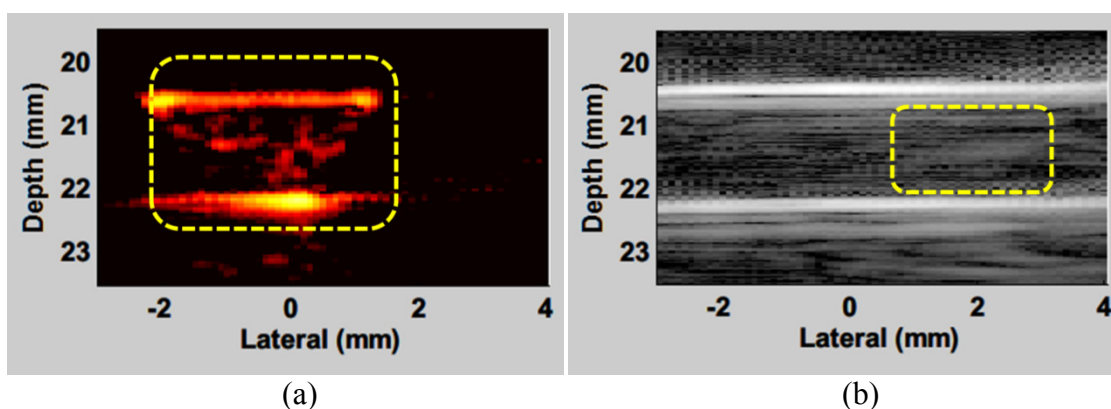


Figure 6.10. a) Photoacoustic and b) ultrasound signal of a 2.8 vol% perfluorohexane emulsion stabilized by 0.2 vol% gold nanoparticles functionalized with 5 dose PEG chains/nm² Au and butane-thiol after irradiation with a 810 nm wavelength laser for 1.10 seconds.

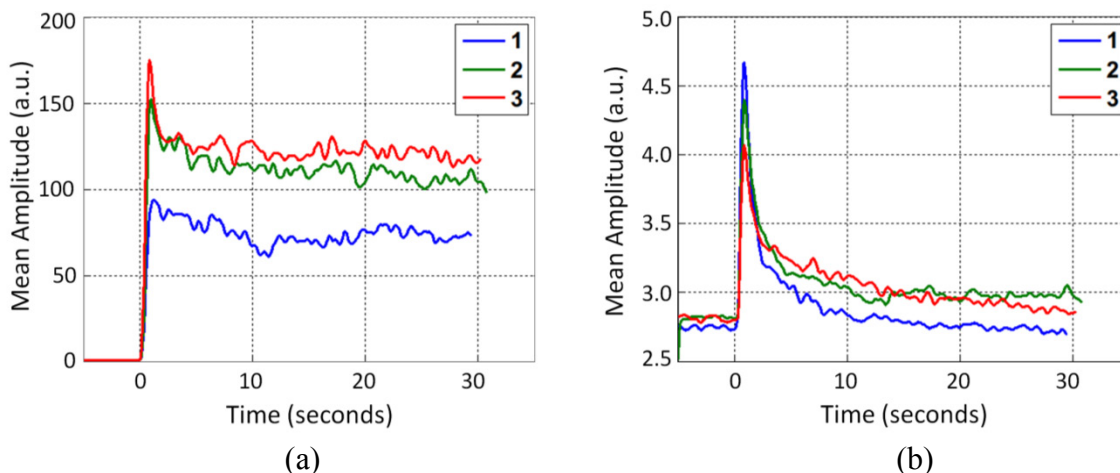


Figure 6.11. a) Integrated photoacoustic and b) ultrasound signal as a function of irradiation time with a 810 nm laser for a 2.8 vol% perfluorohexane emulsion stabilized by 0.2 vol% gold nanoparticles functionalized with 5 dose PEG chains/nm² Au and butane-thiol. The numbers in the legend correspond to sequential repetitions of the measurement.

6.4 Summary

The ability to tune nanoparticle packing at a dispersed oil interface and also the resulting plasmon resonance of metallic particles can be useful for a number of applications. As previously discussed, the ability to engineer the gold particle spacing and therefore the NIR absorbance is critical to the design of nanostructures for medical imaging and photothermal therapy. While solid gold shells have been proven effective theranostic agents due to a high NIR absorbance, they are too large to clear through the renal system. Thus, composite structures of small nanoparticles ($D < 5$ nm) that are NIR absorbent and can be cleared by the renal system could be advantageous for new cancer therapies and imaging technologies.

Self-assembling nanoparticle surfactants are shown to effectively stabilize hexadecane-in-water and perfluorohexane-in-water emulsions. These functional nanoparticles are synthesized through sequential grafting of controlled amounts of

hydrophilic PEG-thiol chains and short hydrophobic alkane chains using thiol chemistry. This simple protocol results in amphiphilic particles that are able to assemble at an oil-water interface at high interfacial concentrations. Furthermore, it is possible to control the particle packing density at the interface through manipulation of steric interactions. This also provides a mechanism to tune the plasmon resonance of the self-assembled metallic particles. These new types of plasmonic emulsions make it possible to design new nanomaterials for a wide range of applications in nanomedicine and renewable energy among others.

Chapter 7: Conclusion

7.1 Key Results

Nanoparticle self-assembly is critical to the engineering of many new materials for a wide range of applications. While there have been many approaches to particle self-assembly in recent years, they often have unique limitations including short-term stability, high production costs or limited batch size. To address these issues, this research was focused on the development of simple, scalable and cost effective strategies for the reliable self-assembly of nanoparticles. More specifically, we have developed methods for directed self-assembly of nanoparticles in dispersion and enhanced self-assembly of nanoparticles at oil-water interfaces.

In Chapter 3 we presented a simple, one-pot method for synthesizing self-assembling nanoparticle surfactants in dispersion. The gold nanoparticles are first functionalized with thiol-terminated polyethylene glycol to sterically stabilize the particles in water. Subsequently, the particles are saturated with an alkane-thiol to render them amphiphilic. In a manner reminiscent of molecular surfactants, the particles cluster with the hydrophobic region shielded in the center of the cluster. We also show the initial PEG-thiol concentration on the particles dictates the size of the final cluster. Dynamic light scattering, small angle x-ray scattering and transmission electron microscopy show that large clusters are formed at the lower PEG-thiol concentration limit and particles remain singlets at the upper PEG-thiol saturation limit. Additionally, it is also possible to expand this new cluster synthesis method, where self-assembly is controlled with steric hindrance, to make clusters from particles of various materials and size.

The mechanism for nanoparticle surfactant synthesis is further examined in Chapter 4. Thermogravimetric analysis indicates that alkane-thiol ligands competitively adsorb on the gold surface and replace previously surface-bound PEG-thiol. The extent of this competitive adsorption is directly dependent on the alkane-thiol length. Moreover, the alkane-thiol forms monolayers with varying surface packing density. The densest monolayer is observed for octane-thiol ligands, which is evidenced by the largest particle alkane molecule to gold ratio as determined by TGA. Interestingly, the alkane-thiol packing density and length also control the PEG-thiol extension. Dynamic light scattering (DLS) shows that the hydrodynamic size of singlet particles is largest after adsorption of octane-thiol and smallest after the adsorption of butane-thiol, which forms the least dense monolayer. This difference in PEG-thiol conformation occurs because the polymer is repelled from the hydrophobic alkane-thiol surface. In the case of patchy alkane monolayers, the PEG-thiol partially wraps around the particle next to the open, citrate-capped gold surface. However, the PEG-thiol extends into the solvent in the presence of a dense alkane monolayer.

The PEG-thiol extension and surface concentration both impact the formation of clusters from nanoparticle surfactants. In a way that is analogous to molecular surfactants, the aggregation number is controlled by the occupied volume and length of the hydrophilic polymers. The occupied volume of the polymer is directly controlled by the surface concentration of PEG-thiol. This was first shown in Chapter 3 by changing the dose PEG-thiol concentration and using octane-thiol as the clustering ligand. In Chapter 4, we show the same principle is true for particle surfactants with different alkane-thiols but the same dose PEG-thiol concentration. In the latter case, the length of the alkane-thiol

determines the extent of PEG-thiol replacement on the gold surface and therefore the aggregation number. Additionally, nanoparticle surfactants that have a more extended polymer conformation will result in larger clusters. Understanding these parameters is extremely useful for the engineering of self-assembling particles in dispersion for a wide range of applications.

Another important class of self-assembly is the adsorption of nanoparticles at oil-water interfaces. Specifically, in Chapter 5 we examined the spontaneous adsorption of charged nanoparticles to hexadecane droplets. The adsorption energy of particles to the oil-water interface scales with the square of particle radius, so nanoparticles are not tightly bound to the interface and are usually less effective emulsifiers. Typically, Pickering emulsions are mechanically formed in the presence of particles, which forces the particles to the interface. However, the adsorption of particles to a previously formed emulsion droplet is more complex. Here we showed the spontaneous adsorption of particles is dependent on the interaction potential between the surface of the oil droplet and particles. These potentials are modeled using DLVO theory to show that the ionic strength of the solution and the charges on the oil droplet and particles are critical to particle adsorption. The adsorption of charged nanoparticles to hexadecane in water emulsions is determined experimentally with small angle scattering. Both theory and experiments show that for like-charged hexadecane and polystyrene particles, the potential is reduced by neutralizing the surface charge at low pH and by shrinking the electrostatic screening length with the addition of salt. In contrast, positively charged particles are electrostatically attracted to the negative hexadecane interface despite having

a low attachment energy. These studies show the importance of surface charges in the spontaneous adsorption of particles to an oil-water interface.

Another method for controlling the nanoparticle adsorption at emulsion interfaces is through particle functionalization. In Chapter 6 we demonstrate the strong adsorption of nanoparticle surfactants at oil-water interfaces. The amphiphilic nature of these particles makes them highly effective emulsifying agents that pack to form stable colloidosomes. Additionally, the close packing of the metallic particles causes significant shifts in plasmon resonance so that the structures have a high absorbance in the near-infrared wavelength region. Small angle x-ray scattering shows we are able to control the fraction of the oil interface that is covered by particles, and therefore the inter-particle spacing, by changing the PEG-thiol surface concentration and the alkane-thiol length. Differences in the inter-particle spacing also result in varying shifts in the plasmon resonance. Thus, it is also possible to tune the NIR absorbance of the colloidosomes through particle functionalization. The ability to engineer the NIR absorbance is critical to the design of nanostructures for photothermal therapy.

In Chapter 6 we introduced the use of plasmonic emulsions for medical imaging and cancer theranostics. Solid gold shells have been shown to be effective for photoacoustic imaging, but they have potential long-term toxicity because they are too large for clearance via the renal system. Thus, a composite structure of nanoparticles that is NIR absorbent could offer equal performance and still be naturally excreted from the body. We also show the added benefit of using an oil core with a low boiling point to gain control over the extent of heating and prevent damage to healthy tissue. This also allows for simultaneous ultrasound imaging because the generated bubble is an additional

contrast agent. In a preliminary study, we demonstrate the use of perfluorohexane emulsions for this application, however additional ongoing work is necessary to optimize this system.

7.2 Future Outlook

The work presented in this thesis provides the fundamental framework for synthesizing nanoparticle surfactants and assembling them into colloidosomes using an emulsion template. However, this is merely an initial effort in demonstrating the feasibility of synthesizing these self-assembling nanostructures. Much work remains to further develop these materials into functional products. The following studies are proposed as an expansion of this effort.

7.2.1 Effect of PEG-thiol Molecular Weight

Chapter 5 focused on how the PEG-thiol conformation and surface concentration affect nanoparticle surfactant self-assembly. We showed the aggregation number of the particles will increase with the PEG-thiol length, or extension, and decrease as the volume occupied by PEG-thiol increases. The effect of changing the PEG-thiol molecular weight is unclear. A smaller PEG-thiol chain will decrease both the polymer extension and volume, which are competing effects on the aggregation number. Initial studies show that nanoparticle surfactants with 5 kDa PEG-thiol will have higher aggregation numbers than the well studied 10 kDa PEG-thiol for a given PEG-thiol surface concentration. The specific details of this effect, however, warrant further investigation.

7.2.2 Scattering Pickering Model

The Pickering Model developed for analyzing small angle scattering data is an extremely effective tool for determining the surface concentration of particles at an emulsion droplet. It has perfect agreement with experimental data for systems that have randomly ordered particles at the interface. However, particles in an ordered arrangement will result in a diffraction peak in the high q region due to particle-particle correlations. The current Pickering Model is not able to account for these in-plane correlations. The highly ordered colloidosomes that were presented in Chapter 6 have clear diffraction peaks due to their high degree of order. Thus, this model should be further expanded to account for such correlations.

7.2.3 Photoacoustic Imaging and Photothermal Therapies

Organic Phase Selection - Choosing the appropriate organic phase is critical to ‘bubble blowing’ aspect of this system. In addition to being non-toxic, the boiling point of the oil phase has to be higher than body temperature but low enough that the heat generated from NIR adsorption will be sufficient for vaporization. Initial studies also indicate that the organic phase must have low water solubility because of the dilution *in vivo*. This is an especially difficult design challenge because typically smaller molecules with low boiling points are more soluble in water. Perfluorohexane has shown to be a promising choice; however there is still room for further optimization.

5 nm Nanoparticle Surfactants - The primary advantage to composite nanoshells over solid nanoshell theranostic agents is the ability to decompose the nanostructure post treatment or imaging. The maximum size particle that can pass through the renal system

is 5 nm in diameter; therefore the particles used to form the plasmonic emulsions must be smaller than this limit. The particles used in this thesis are 12 nm in diameter and are still too large for clearance through the body. Thus, it is necessary to synthesize smaller nanoparticle surfactants for this application.

Optimize Near-Infrared Absorption - Maximizing NIR absorption of the gold nanostructure that occurs upon radiation is paramount to the success of this application. The localized heating that results from NIR absorption is used to vaporize the organic phase and become a bubble. We have shown it is possible to tune NIR absorbance by carefully choosing the alkane-thiol and PEG-thiol concentrations on the nanoparticle surfactants. Furthermore, the plasmonic emulsion size will also likely affect the absorbance. These parameters need to be fully investigated in order to maximize adsorption in the NIR region.

Target-label Gold Nanoparticles - Possibly the most challenging design parameter that remains to be studied is functionalizing the gold particles to target specific tissues. Using thiol-gold covalent bonding, attaching the antibody or other targeting ligand should be a simple task. However, the effect of this additional ligand on the plasmonic emulsion self-assembly needs to be fully examined. In Chapter 5 of this thesis, we showed that thiolated ligands will competitively adsorb on gold surfaces. Thus, we expect there will be some added complexity with the introduction of a third thiolated species. One potential way to ensure the targeting ligands remain on the outside of the emulsions is to functionalize the gold after the formation of the plasmonic emulsion. Alternatively, it may be possible to use PEG-thiol with a terminal targeting functional group. These two possible routes for attaching targeting ligands to the gold particles are

meant to show that there may be many ways to address this design challenge. Still, much work remains to make this technology successful.

7.2.4 Organic Photovoltaics

Tunable plasmon resonance can also be utilized in the design of organic photovoltaic devices. The assembly of organic semiconducting polymers is another active area of research and expertise in the Pozzo Lab. Recently, Richards, Weigandt and Pozzo developed a method for encapsulating photoactive gels of semi-conducting polymer in emulsion droplets that can be easily coated into thin films.¹⁷⁴ The ability to coat concentrated polymer gels is revolutionary way to improve device efficiency because it makes it possible to coat carefully engineered bulk polymer gels. Additionally, Wu et al. showed an improvement in organic solar cell efficiency by utilizing the plasmonic effects of gold nanoparticles that were incorporated into the polymer network.¹⁷⁵ Utilizing a self-assembling structure with a tunable plasmon resonance might result in even further enhancements in device efficiency. For this application the photoactive polymer gel beads could be encapsulated in the self-assembled gold clusters prior to coating in order to harness more energy from the photovoltaic device.¹⁷⁴

The vastly different applications briefly discussed here illustrate the potential impact that these self-assembling nanoparticle surfactants can have in the development of new nanomaterials. The number of proposed experiments presented here show that this is still an important and active research area. The work presented in this thesis lays the fundamental framework for these future application-driven projects.

List of References

1. Velev, O. D.; Furusawa, K.; Nagayama, K., Assembly of latex particles by using emulsion droplets as templates .1. Microstructured hollow spheres. *Langmuir* **1996**, 12, (10), 2374-2384.
2. Dinsmore, A. D.; Hsu, M. F.; Nikolaides, M. G.; Marquez, M.; Bausch, A. R.; Weitz, D. A., Colloidosomes: Selectively permeable capsules composed of colloidal particles. *Science* **2002**, 298, (5595), 1006-1009.
3. Harris, P. J. F., Carbon Nanotube Composites. *International Materials Review* **2004**, 49, (1), 31-43.
4. Murray, C. B.; Kagan, C. R.; Bawendi, M. G., SELF-ORGANIZATION OF CDSE NANOCRYSTALLITES INTO 3-DIMENSIONAL QUANTUM-DOT SUPERLATTICES. *Science* **1995**, 270, (5240), 1335-1338.
5. Alivisatos, A. P.; Barbara, P. F.; Castleman, A. W.; Chang, J.; Dixon, D. A.; Klein, M. L.; McLendon, G. L.; Miller, J. S.; Ratner, M. A.; Rossky, P. J.; Stupp, S. I.; Thompson, M. E., From molecules to materials: Current trends and future directions. *Advanced Materials* **1998**, 10, (16), 1297-1336.
6. Miguel, A. S.; Behrens, S. H., Permeability control in stimulus-responsive colloidosomes. *Soft Matter* **2011**, 7, (5), 1948-1956.
7. Alivisatos, A. P., Semiconductor clusters, nanocrystals, and quantum dots. *Science* **1996**, 271, (5251), 933-937.
8. Sander, D., Surface stress: implications and measurements. *Curr. Opin. Solid State Mat. Sci.* **2003**, 7, (1), 51-57.
9. Tiwari, S.; Rana, F.; Chan, K.; Shi, L.; Hanafi, H., Single charge and confinement effects in nano-crystal memories. *Appl. Phys. Lett.* **1996**, 69, (9), 1232-1234.
10. Kelly, K. L.; Coronado, E.; Zhao, L. L.; Schatz, G. C., The optical properties of metal nanoparticles: The influence of size, shape, and dielectric environment. *Journal of Physical Chemistry B* **2003**, 107, (3), 668-677.
11. Brus, L., QUANTUM CRYSTALLITES AND NONLINEAR OPTICS. *Applied Physics a-Materials Science & Processing* **1991**, 53, (6), 465-474.
12. Empedocles, S. A.; Neuhauser, R.; Bawendi, M. G., Three-dimensional orientation measurements of symmetric single chromophores using polarization microscopy. *Nature* **1999**, 399, (6732), 126-130.
13. Harkins, W. D., A GENERAL THEORY OF THE MECHANISM OF EMULSION POLYMERIZATION. *Journal of the American Chemical Society* **1947**, 69, (6), 1428-&.
14. Gorup, L. F.; Longo, E.; Leite, E. R.; Camargo, E. R., Moderating effect of ammonia on particle growth and stability of quasi-monodisperse silver nanoparticles synthesized by the Turkevich method. *Journal of Colloid and Interface Science* **2011**, 360, (2), 355-358.
15. Turkevich, J.; Stevenson, P. C.; Hillier, J., A STUDY OF THE NUCLEATION AND GROWTH PROCESSES IN THE SYNTHESIS OF COLLOIDAL GOLD. *Discussions of the Faraday Society* **1951**, (11), 55-&.
16. Lu, Y.; Yin, Y. D.; Li, Z. Y.; Xia, Y. N., Colloidal crystals made of polystyrene spheroids: Fabrication and structural/optical characterization. *Langmuir* **2002**, 18, (20), 7722-7727.

17. Sun, Y. G.; Xia, Y. N., Shape-controlled synthesis of gold and silver nanoparticles. *Science* **2002**, 298, (5601), 2176-2179.
18. Sugimoto, T.; Khan, M. M.; Muramatsu, A.; Itoh, H., FORMATION MECHANISM OF MONODISPERSE PEANUT-TYPE ALPHA- Fe_2O_3 PARTICLES FROM CONDENSED FERRIC HYDROXIDE GEL. *Colloids and Surfaces a-Physicochemical and Engineering Aspects* **1993**, 79, (2-3), 233-247.
19. Sugimoto, T.; Khan, M. M.; Muramatsu, A., PREPARATION OF MONODISPERSE PEANUT-TYPE ALPHA- Fe_2O_3 PARTICLES FROM CONDENSED FERRIC HYDROXIDE GEL. *Colloids and Surfaces a-Physicochemical and Engineering Aspects* **1993**, 70, (2), 167-169.
20. Wang, X. S.; Li, Q. Q.; Xie, J.; Jin, Z.; Wang, J. Y.; Li, Y.; Jiang, K. L.; Fan, S. S., Fabrication of Ultralong and Electrically Uniform Single-Walled Carbon Nanotubes on Clean Substrates. *Nano Letters* **2009**, 9, (9), 3137-3141.
21. Guo, T.; Nikolaev, P.; Thess, A.; Colbert, D. T.; Smalley, R. E., CATALYTIC GROWTH OF SINGLE-WALLED NANOTUBES BY LASER VAPORIZATION. *Chemical Physics Letters* **1995**, 243, (1-2), 49-54.
22. Joseyacaman, M.; Mikiyoshida, M.; Rendon, L.; Santiesteban, J. G., CATALYTIC GROWTH OF CARBON MICROTUBULES WITH FULLERENE STRUCTURE (APPLIED PHYSICS LETTER, VOL 62, PG 202, 1993). *Applied Physics Letters* **1993**, 62, (6), 657-659.
23. Ito, T.; Okazaki, S., Pushing the limits of lithography. *Nature* **2000**, 406, (6799), 1027-1031.
24. Hong, S. H.; Zhu, J.; Mirkin, C. A., Multiple ink nanolithography: Toward a multiple-pen nano-plotter. *Science* **1999**, 286, (5439), 523-525.
25. Grabar, K. C.; Allison, K. J.; Baker, B. E.; Bright, R. M.; Brown, K. R.; Freeman, R. G.; Fox, A. P.; Keating, C. D.; Musick, M. D.; Natan, M. J., Two-dimensional arrays of colloidal gold particles: A flexible approach to macroscopic metal surfaces. *Langmuir* **1996**, 12, (10), 2353-2361.
26. Pawar, A. B.; Kretschmar, I., Fabrication, Assembly, and Application of Patchy Particles. *Macromolecular Rapid Communications* **2010**, 31, (2), 150-168.
27. Glotzer, S. C.; Solomon, M. J.; Kotov, N. A., Self-assembly: From nanoscale to microscale colloids. *Aiche Journal* **2004**, 50, (12), 2978-2985.
28. Boncheva, M.; Whitesides, G. M., Making things by self-assembly. *Mrs Bulletin* **2005**, 30, (10), 736-742.
29. Whitesides, G. M.; Mathias, J. P.; Seto, C. T., MOLECULAR SELF-ASSEMBLY AND NANOCHEMISTRY - A CHEMICAL STRATEGY FOR THE SYNTHESIS OF NANOSTRUCTURES. *Science* **1991**, 254, (5036), 1312-1319.
30. Watson, J. D.; Crick, F. H. C., MOLECULAR STRUCTURE OF NUCLEIC ACIDS - A STRUCTURE FOR DEOXYRIBOSE NUCLEIC ACID. *Nature* **1953**, 171, (4356), 737-738.
31. Chantalat, L.; Jones, N. D.; Korber, F.; Navaza, J.; Pavlovsky, A. G., THE CRYSTAL-STRUCTURE OF WILD-TYPE GROWTH-HORMONE AT 2.5 ANGSTROM RESOLUTION. *Protein and Peptide Letters* **1995**, 2, (2), 333-340.
32. Berg, J. C., *An Introduction to Interfaces & Colloids: The Bridge to Nanoscience*. World Scientific Publishing Co.: Singapore, 2010.

33. Rockford, L.; Liu, Y.; Mansky, P.; Russell, T. P.; Yoon, M.; Mochrie, S. G. J., Polymers on nanopericodic, heterogeneous surfaces. *Physical Review Letters* **1999**, 82, (12), 2602-2605.
34. Love, J. C.; Estroff, L. A.; Kriebel, J. K.; Nuzzo, R. G.; Whitesides, G. M., Self-assembled monolayers of thiolates on metals as a form of nanotechnology. *Chemical Reviews* **2005**, 105, (4), 1103-1169.
35. Manoharan, V. N.; Elsesser, M. T.; Pine, D. J., Dense packing and symmetry in small clusters of microspheres. *Science* **2003**, 301, (5632), 483-487.
36. Anyfantakis, M.; Bourlinos, A.; Vlassopoulos, D.; Fytas, G.; Giannelis, E.; Kumar, S. K., Solvent-mediated pathways to gelation and phase separation in suspensions of grafted nanoparticles. *Soft Matter* **2009**, 5, (21), 4256-4265.
37. Gentilini, C.; Evangelista, F.; Rudolf, P.; Franchi, P.; Lucarini, M.; Pasquato, L., Water-Soluble Gold Nanoparticles Protected by Fluorinated Amphiphilic Thiolates. *Journal of the American Chemical Society* **2008**, 130, (46), 15678-15682.
38. Gentilini, C.; Pasquato, L., Morphology of mixed-monolayers protecting metal nanoparticles. *Journal of Materials Chemistry* **2009**, 20, (8), 1403-1412.
39. van Herrikhuyzen, J.; Portale, G.; Gielen, J. C.; Christianen, P. C. M.; Sommerdijk, N.; Meskers, S. C. J.; Schenning, A., Disk micelles from amphiphilic Janus gold nanoparticles. *Chemical Communications* **2008**, (6), 697-699.
40. Narayanan, R. A.; Thiyagarajan, P.; Zhu, A. J.; Ash, J.; Shofner, M. L.; Schadler, L. S.; Kumar, S. K.; Sternstein, S. S., Nanostructural features in silica-polyvinyl acetate nanocomposites characterized by small-angle scattering. *Polymer* **2007**, 48, (19), 5734-5741.
41. Hong, L.; Cacciuto, A.; Luijten, E.; Granick, S., Clusters of amphiphilic colloidal spheres. *Langmuir* **2008**, 24, (3), 621-625.
42. Yake, A. M.; Snyder, C. E.; Velegol, D., Site-specific functionalization on individual colloids: Size control, stability, and multilayers. *Langmuir* **2007**, 23, (17), 9069-9075.
43. Pawar, A. B.; Kretzschmar, I., Patchy particles by glancing angle deposition. *Langmuir* **2008**, 24, (2), 355-358.
44. Hong, L.; Cacciuto, A.; Luijten, E.; Granick, S., Clusters of charged Janus spheres. *Nano Letters* **2006**, 6, (11), 2510-2514.
45. Saleh, N.; Sirk, K.; Liu, Y. Q.; Phenrat, T.; Dufour, B.; Matyjaszewski, K.; Tilton, R. D.; Lowry, G. V., Surface modifications enhance nanoiron transport and NAPL targeting in saturated porous media. *Environ. Eng. Sci.* **2007**, 24, (1), 45-57.
46. Chatterjee, U.; Jewrajka, S. K.; Guha, S., Dispersion of Functionalized Silver Nanoparticles in Polymer Matrices: Stability, Characterization, and Physical Properties. *Polymer Composites* **2009**, 30, (6), 827-834.
47. Li, C. Z.; Benicewicz, B. C., Synthesis of well-defined polymer brushes grafted onto silica nanoparticles via surface reversible addition-fragmentation chain transfer polymerization. *Macromolecules* **2005**, 38, (14), 5929-5936.
48. Pyun, J.; Matyjaszewski, K., Synthesis of nanocomposite organic/inorganic hybrid materials using controlled/"living" radical polymerization. *Chem. Mat.* **2001**, 13, (10), 3436-3448.

49. Park, S. Y.; Lytton-Jean, A. K. R.; Lee, B.; Weigand, S.; Schatz, G. C.; Mirkin, C. A., DNA-programmable nanoparticle crystallization. *Nature* **2008**, 451, (7178), 553-556.
50. Stradner, A.; Sedgwick, H.; Cardinaux, F.; Poon, W. C. K.; Egelhaaf, S. U.; Schurtenberger, P., Equilibrium cluster formation in concentrated protein solutions and colloids. *Nature* **2004**, 432, (7016), 492-495.
51. Lindner, P.; Zemb, T., *Neutrons, X-rays and Light: Scattering Methods Applied to Soft Condensed Matter*. Elsevier Science: Amsterdam, 2002.
52. Glatter, O.; Kratky, O., *Small Angle X-ray Scattering*. Academic Press Inc.: London, 1982.
53. Hammouda, B., Probing Nanoscale Structures - The SANS Toolbox. In 2011.
54. Lake, J. A., AN ITERATIVE METHOD OF SLIT-CORRECTING SMALL ANGLE X-RAY DATA. *Acta Crystallographica* **1967**, 23, 191-&.
55. Alina, G.; Cortes Hernandez, R.; Butler, P.; Doucet, M.; Jackson, A.; Kienzle, P.; Kline, S.; Zhou, J. DANSE/SANSView.
56. Guinier, A., *Small Angle Scattering*. In 1955; p 127.
57. Kline, S. R., Reduction and analysis of SANS and USANS data using IGOR Pro. *Journal of Applied Crystallography* **2006**, 39, 895-900.
58. Larson-Smith, K.; Jackson, A.; Pozzo, D. C., Small angle scattering model for Pickering emulsions and raspberry particles. *Journal of Colloid and Interface Science* **2010**, 343, (1), 36-41.
59. Debye, P., MOLECULAR-WEIGHT DETERMINATION BY LIGHT SCATTERING. *Journal of Physical and Colloid Chemistry* **1947**, 51, (1), 18-32.
60. Rayleigh, On Dr. Johnstone Stoney's logarithmic law of atomic weights. *Proceedings of the Royal Society of London Series a-Containing Papers of a Mathematical and Physical Character* **1911**, 85, (580), 471-473.
61. Pedersen, J. S., Structure factors effects in small-angle scattering from block copolymer micelles and star polymers. *Journal of Chemical Physics* **2001**, 114, (6), 2839-2846.
62. Gill, M.; Mykytiuk, J.; Armes, S. P.; Edwards, J. L.; Yeates, T.; Moreland, P. J.; Mollett, C., NOVEL COLLOIDAL POLYANILINE SILICA COMPOSITES. *Journal of the Chemical Society-Chemical Communications* **1992**, (2), 108-109.
63. Bourgeat-Lami, E.; Lang, J., Encapsulation of inorganic particles by dispersion polymerization in polar media - 1. Silica nanoparticles encapsulated by polystyrene. *Journal of Colloid and Interface Science* **1998**, 197, (2), 293-308.
64. Percy, M. J.; Amalvy, J. I.; Randall, D. P.; Armes, S. P.; Greaves, S. J.; Watts, J. F., Synthesis of vinyl polymer-silica colloidal nanocomposites prepared using commercial alcoholic silica sols. *Langmuir* **2004**, 20, (6), 2184-2190.
65. Yoshinaga, K.; Yokoyama, T.; Sugawa, Y.; Karakawa, H.; Enomoto, N.; Nishida, H.; Komatsu, M., PREPARATION OF MONODISPERSED POLYMER-MODIFIED SILICA PARTICLES BY RADICAL POLYMERIZATION USING SILICA COLLOID AND INTRODUCTION OF FUNCTIONAL-GROUPS ON THE COMPOSITE SURFACE. *Polymer Bulletin* **1992**, 28, (6), 663-668.
66. Schmid, A.; Armes, S. P.; Leite, C. A. P.; Galembeck, F., Efficient Preparation of Polystyrene/Silica Colloidal Nanocomposite Particles by Emulsion

- Polymerization Using a Glycerol-Functionalized Silica Sol. *Langmuir* **2009**, *25*, (4), 2486-2494.
67. Maeda, S.; Armes, S. P., PREPARATION AND CHARACTERIZATION OF POLYPYRROLE TIN(IV) OXIDE NANOCOMPOSITE COLLOIDS. *Chemistry of Materials* **1995**, *7*, (1), 171-178.
 68. Lin, Y.; Skaff, H.; Emrick, T.; Dinsmore, A. D.; Russell, T. P., Nanoparticle assembly and transport at liquid-liquid interfaces. *Science* **2003**, *299*, (5604), 226-229.
 69. Larson-Smith, K.; Pozzo, D. C., Scalable synthesis of self-assembling nanoparticle clusters based on controlled steric interactions. *Soft Matter* **2011**, *7*, (11), 5339-5347.
 70. Cobley, C. M.; Skrabalak, S. E.; Campbell, D. J.; Xia, Y. A., Shape-Controlled Synthesis of Silver Nanoparticles for Plasmonic and Sensing Applications. *Plasmonics* **2009**, *4*, (2), 171-179.
 71. Brust, M.; Kiely, C. J., Some recent advances in nanostructure preparation from gold and silver particles: a short topical review. *Colloids and Surfaces a-Physicochemical and Engineering Aspects* **2002**, *202*, (2-3), 175-186.
 72. Glotzer, S. C.; Solomon, M. J., Anisotropy of building blocks and their assembly into complex structures. *Nature Materials* **2007**, *6*, (8), 557-562.
 73. Burda, C.; Chen, X. B.; Narayanan, R.; El-Sayed, M. A., Chemistry and properties of nanocrystals of different shapes. *Chemical Reviews* **2005**, *105*, (4), 1025-1102.
 74. Tompa, P.; Fuxreiter, M., Fuzzy complexes: polymorphism and structural disorder in protein-protein interactions. *Trends in Biochemical Sciences* **2008**, *33*, (1), 2-8.
 75. McCarley, R. L.; Dunaway, D. J.; Willicut, R. J., MOBILITY OF THE ALKANETHIOL GOLD(111) INTERFACE STUDIED BY SCANNING PROBE MICROSCOPY. *Langmuir* **1993**, *9*, (11), 2775-2777.
 76. Carney, R. P.; DeVries, G. A.; Dubois, C.; Kim, H.; Kim, J. Y.; Singh, C.; Ghorai, P. K.; Tracy, J. B.; Stiles, R. L.; Murray, R. W.; Glotzer, S. C.; Stellacci, F., Size limitations for the formation of ordered striped nanoparticles. *Journal of the American Chemical Society* **2008**, *130*, (3), 798-+.
 77. Singh, C.; Ghorai, P. K.; Horsch, M. A.; Jackson, A. M.; Larson, R. G.; Stellacci, F.; Glotzer, S. C., Entropy-mediated patterning of surfactant-coated nanoparticles and surfaces. *Physical Review Letters* **2007**, *99*, (22).
 78. Schreiber, F., Structure and growth of self-assembling monolayers. *Progress in Surface Science* **2000**, *65*, (5-8), 151-256.
 79. Sondaghuethorst, J. A. M.; Schonenberger, C.; Fokkink, L. G. J., FORMATION OF HOLES IN ALKANETHIOL MONOLAYERS ON GOLD. *J. Phys. Chem.* **1994**, *98*, (27), 6826-6834.
 80. Ghorai, P. K.; Glotzer, S. C., Atomistic Simulation Study of Striped Phase Separation in Mixed-Ligand Self-Assembled Monolayer Coated Nanoparticles. *Journal of Physical Chemistry C* **2010**, *114*, (45), 19182-19187.
 81. Tsai, D. H.; DelRio, F. W.; MacCuspie, R. I.; Cho, T. J.; Zachariah, M. R.; Hackley, V. A., Competitive Adsorption of Thiolated Polyethylene Glycol and

- Mercaptopropionic Acid on Gold Nanoparticles Measured by Physical Characterization Methods. *Langmuir* **2010**, 26, (12), 10325-10333.
82. Frens, G., CONTROLLED NUCLEATION FOR REGULATION OF PARTICLE-SIZE IN MONODISPERSE GOLD SUSPENSIONS. *Nature-Physical Science* **1973**, 241, (105), 20-22.
83. Shan, J.; Tenhu, H., Recent advances in polymer protected gold nanoparticles: synthesis, properties and applications. *Chemical Communications* **2007**, (44), 4580-4598.
84. Nuzzo, R. G.; Allara, D. L., ADSORPTION OF BIFUNCTIONAL ORGANIC DISULFIDES ON GOLD SURFACES. *Journal of the American Chemical Society* **1983**, 105, (13), 4481-4483.
85. Porter, M. D.; Bright, T. B.; Allara, D. L.; Chidsey, C. E. D., SPONTANEOUSLY ORGANIZED MOLECULAR ASSEMBLIES .4. STRUCTURAL CHARACTERIZATION OF NORMAL-ALKYL THIOL MONOLAYERS ON GOLD BY OPTICAL ELLIPSOMETRY, INFRARED-SPECTROSCOPY, AND ELECTROCHEMISTRY. *Journal of the American Chemical Society* **1987**, 109, (12), 3559-3568.
86. Corbierre, M. K.; Cameron, N. S.; Lennox, R. B., Polymer-stabilized gold nanoparticles with high grafting densities. *Langmuir* **2004**, 20, (7), 2867-2873.
87. Debye, P., X-ray dispersal. *Annalen Der Physik* **1915**, 46, (6), 809-823.
88. Gunier, A., *Small Angle Scattering* **1955**, 127.
89. Yamada, S.; Israelachvili, J., Friction and adhesion hysteresis of fluorocarbon surfactant monolayer-coated surfaces measured with the surface forces apparatus. *Journal of Physical Chemistry B* **1998**, 102, (1), 234-244.
90. Notoya, T.; Poling, G. W., PROTECTION OF COPPER BY PRETREATMENT WITH BENZOTRIAZOLE. *Corrosion* **1979**, 35, (5), 193-200.
91. Jackson, A. M.; Myerson, J. W.; Stellacci, F., Spontaneous assembly of subnanometre-ordered domains in the ligand shell of monolayer-protected nanoparticles. *Nature Materials* **2004**, 3, (5), 330-336.
92. Bain, C. D.; Troughton, E. B.; Tao, Y. T.; Evall, J.; Whitesides, G. M.; Nuzzo, R. G., FORMATION OF MONOLAYER FILMS BY THE SPONTANEOUS ASSEMBLY OF ORGANIC THIOLS FROM SOLUTION ONTO GOLD. *Journal of the American Chemical Society* **1989**, 111, (1), 321-335.
93. Strong, L.; Whitesides, G. M., STRUCTURES OF SELF-ASSEMBLED MONOLAYER FILMS OF ORGANOSULFUR COMPOUNDS ADSORBED ON GOLD SINGLE-CRYSTALS - ELECTRON-DIFFRACTION STUDIES. *Langmuir* **1988**, 4, (3), 546-558.
94. Eck, W.; Craig, G.; Sigdel, A.; Ritter, G.; Old, L. J.; Tang, L.; Brennan, M. F.; Allen, P. J.; Mason, M. D., PEGylated Gold Nanoparticles Conjugated to Monoclonal F19 Antibodies as Targeted Labeling Agents for Human Pancreatic Carcinoma Tissue. *Acs Nano* **2008**, 2, (11), 2263-2272.
95. Paciotti, G. F.; Myer, L.; Weinreich, D.; Goia, D.; Pavel, N.; McLaughlin, R. E.; Tamarkin, L., Colloidal gold: A novel nanoparticle vector for tumor directed drug delivery. *Drug Delivery* **2004**, 11, (3), 169-183.

96. Tamada, K.; Hara, M.; Sasabe, H.; Knoll, W., Surface phase behavior of n-alkanethiol self-assembled monolayers adsorbed on Au(111): An atomic force microscope study. *Langmuir* **1997**, *13*, (6), 1558-1566.
97. Jackson, A. M.; Hu, Y.; Silva, P. J.; Stellacci, F., From homoligand- to mixed-ligand-monolayer-protected metal nanoparticles: A scanning tunneling microscopy investigation. *Journal of the American Chemical Society* **2006**, *128*, (34), 11135-11149.
98. Schlenoff, J. B.; Li, M.; Ly, H., Stability and self-exchange in alkanethiol monolayers. *Journal of the American Chemical Society* **1995**, *117*, (50), 12528-12536.
99. Tsai, D. H.; Davila-Morris, M.; DelRio, F. W.; Guha, S.; Zachariah, M. R.; Hackley, V. A., Quantitative Determination of Competitive Molecular Adsorption on Gold Nanoparticles Using Attenuated Total Reflectance-Fourier Transform Infrared Spectroscopy. *Langmuir* **2011**, *27*, (15), 9302-9313.
100. Huckel, E., The cataphoresis of the sphere. *Physikalische Zeitschrift* **1924**, *25*, 204-210.
101. Hostetler, M. J.; Stokes, J. J.; Murray, R. W., Infrared spectroscopy of three-dimensional self-assembled monolayers: N-alkanethiolate monolayers on gold cluster compounds. *Langmuir* **1996**, *12*, (15), 3604-3612.
102. Israelachvili, J. N., *Intermolecular and Surface Forces*. 3rd ed.; Elsevier Inc.: Amsterdam, 2011.
103. Marques, C. M., Bunchy micelles. *Langmuir* **1997**, *13*, (6), 1430-1433.
104. Farma, J. M.; Puhlmann, M.; Soriano, P. A.; Cox, D.; Paciotti, G. F.; Tamarkin, L.; Alexander, H. R., Direct evidence for rapid and selective induction of tumor neovascular permeability by tumor necrosis factor and a novel derivative, colloidal gold bound tumor necrosis factor. *International Journal of Cancer* **2007**, *120*, (11), 2474-2480.
105. Goel, R.; Swanlund, D.; Coad, J.; Paciotti, G. F.; Bischof, J. C., TNF-alpha-based accentuation in cryoinjury - dose, delivery, and response. *Molecular Cancer Therapeutics* **2007**, *6*, (7), 2039-2047.
106. Larson-Smith, K.; Jackson, A.; Pozzo, D. C., SANS and SAXS Analysis of Charged Nanoparticle Adsorption at Oil-Water Interfaces. *Langmuir* **2012**, *28*, (5), 2493-2501.
107. Pickering, S. U., Emulsions. *Journal of the Chemical Society* **1907**, *91*, 2001-2021.
108. Binks, B. P.; Lumsdon, S. O., Pickering emulsions stabilized by monodisperse latex particles: Effects of particle size. *Langmuir* **2001**, *17*, (15), 4540-4547.
109. Aveyard, R.; Binks, B. P.; Clint, J. H., Emulsions stabilised solely by colloidal particles. *Advances in Colloid and Interface Science* **2003**, *100*, 503-546.
110. Hunter, T. N.; Pugh, R. J.; Franks, G. V.; Jameson, G. J., The role of particles in stabilising foams and emulsions. *Advances in Colloid and Interface Science* **2008**, *137*, (2), 57-81.
111. Whitby, C. P.; Djerdjev, A. M.; Beattie, J. K.; Warr, G. G., Nanoparticle adsorption and stabilisation of surfactant-free emulsions. *Journal of Colloid and Interface Science* **2006**, *301*, (1), 342-345.

112. Tambe, D. E.; Sharma, M. M., FACTORS CONTROLLING THE STABILITY OF COLLOID-STABILIZED EMULSIONS .1. AN EXPERIMENTAL INVESTIGATION. *Journal of Colloid and Interface Science* **1993**, 157, (1), 244-253.
113. Eric, D., *An Introduction to Food Colloids*. Oxford University Press: Oxford, 1992.
114. Nielloud, F.; Marti-Mestres, G., *Pharmaceutical Emulsions & Suspensions*. Marcel Dekker Inc.: New York, 2000; Vol. 105.
115. Pieranski, P., TWO-DIMENSIONAL INTERFACIAL COLLOIDAL CRYSTALS. *Physical Review Letters* **1980**, 45, (7), 569-572.
116. Binks, B. P.; Clint, J. H., Solid wettability from surface energy components: Relevance to pickering emulsions. *Langmuir* **2002**, 18, (4), 1270-1273.
117. Bresme, F.; Oettel, M., Nanoparticles at fluid interfaces. *Journal of Physics-Condensed Matter* **2007**, 19, (41).
118. Reincke, F.; Kegel, W. K.; Zhang, H.; Nolte, M.; Wang, D. Y.; Vanmaekelbergh, D.; Mohwald, H., Understanding the self-assembly of charged nanoparticles at the water/oil interface. *Physical Chemistry Chemical Physics* **2006**, 8, (33), 3828-3835.
119. Stachurski, J.; Michalek, M., The effect of the zeta potential on the stability of a non-polar oil-in-water emulsion. *Journal of Colloid and Interface Science* **1996**, 184, (2), 433-436.
120. Marinova, K. G.; Alargova, R. G.; Denkov, N. D.; Velev, O. D.; Petsev, D. N.; Ivanov, I. B.; Borwankar, R. P., Charging of oil-water interfaces due to spontaneous adsorption of hydroxyl ions. *Langmuir* **1996**, 12, (8), 2045-2051.
121. Tanford, C., *The hydrophobic effect: formation of micelles and biological membranes*. Wiley: New York, 1973.
122. Israelachvili, J. N., *Intermolecular and surface forces : with applications to colloidal and biological systems*. Academic Press: London, 1985.
123. Beattie, J. K.; Djerdjev, A. M., The pristine oil/water interface: Surfactant-free hydroxide-charged emulsions. *Angewandte Chemie-International Edition* **2004**, 43, (27), 3568-3571.
124. Stilling, Fh; Bennaim, A., LIQUID-VAPOR INTERFACE POTENTIAL FOR WATER. *Journal of Chemical Physics* **1967**, 47, (11), 4431-&.
125. Kuzmin, V. L., ORIENTATION OF MOLECULES IN SURFACE-LAYER OF POLAR LIQUID. *Colloid Journal of the Ussr* **1983**, 45, (2), 193-199.
126. Vacha, R.; Rick, S. W.; Jungwirth, P.; de Beer, A. G. F.; de Aguiar, H. B.; Samson, J. S.; Roke, S., The Orientation and Charge of Water at the Hydrophobic Oil Droplet-Water Interface. *Journal of the American Chemical Society* **2011**, 133, (26), 10204-10210.
127. Simovic, S.; Prestidge, C. A., Hydrophilic silica nanoparticles at the PDMS droplet-water interface. *Langmuir* **2003**, 19, (9), 3785-3792.
128. Prestidge, C. A.; Simovic, S., Nanoparticle encapsulation of emulsion droplets. *International Journal of Pharmaceutics* **2006**, 324, (1), 92-100.
129. Verruto, V. J.; Kilpatrick, P. K., Preferential solvent partitioning within asphaltenic aggregates dissolved in binary solvent mixtures. *Energy & Fuels* **2007**, 21, (3), 1217-1225.

130. Verruto, V. J.; Kilpatrick, P. K., Water-in-Model Oil Emulsions Studied by Small-Angle Neutron Scattering: Interfacial Film Thickness and Composition. *Langmuir* **2008**, 24, (22), 12807-12822.
131. Thiyagarajan, P.; Hunt, J. E.; Winans, R. E.; Anderson, K. B.; Miller, J. T., TEMPERATURE-DEPENDENT STRUCTURAL-CHANGES OF ASPHALTENES IN 1-METHYLNAPHTHALENE. *Energy & Fuels* **1995**, 9, (5), 829-833.
132. Sheu, E. Y.; Storm, D. A.; Detar, M. M., ASPHALTENES IN POLAR-SOLVENTS. *Journal of Non-Crystalline Solids* **1991**, 131, 341-347.
133. Sheu, E. Y.; Liang, K. S.; Sinha, S. K.; Overfield, R. E., POLYDISPERSITY ANALYSIS OF ASPHALTENE SOLUTIONS IN TOLUENE. *Journal of Colloid and Interface Science* **1992**, 153, (2), 399-410.
134. Roux, J. N.; Broseta, D.; Deme, B., SANS study of asphaltene aggregation: Concentration and solvent quality effects. *Langmuir* **2001**, 17, (16), 5085-5092.
135. Gawrys, K. L.; Kilpatrick, P. K., Asphaltenic aggregates are polydisperse oblate cylinders. *Journal of Colloid and Interface Science* **2005**, 288, (2), 325-334.
136. Fenistein, D.; Barre, L.; Broseta, D.; Espinat, D.; Livet, A.; Roux, J. N.; Scarsella, M., Viscosimetric and neutron scattering study of asphaltene aggregates in mixed toluene/heptane solvents. *Langmuir* **1998**, 14, (5), 1013-1020.
137. Gawrys, K. L.; Blankenship, G. A.; Kilpatrick, P. K., Solvent entrainment in and flocculation of asphaltenic aggregates probed by small-angle neutron scattering. *Langmuir* **2006**, 22, (10), 4487-4497.
138. Brust, M.; Walker, M.; Bethell, D.; Schiffrin, D. J.; Whyman, R., SYNTHESIS OF THIOL-DERIVATIZED GOLD NANOPARTICLES IN A 2-PHASE LIQUID-LIQUID SYSTEM. *Journal of the Chemical Society-Chemical Communications* **1994**, (7), 801-802.
139. Abràmoff, M. D., Magalhães, P.J. and Ram, S.J., *Image Processing with ImageJ*. *Biophotonics International* **2004**, 11, (7), 36-42.
140. Mangelsdorf, C. S.; White, L. R., EFFECTS OF STERN-LAYER CONDUCTANCE ON ELECTROKINETIC TRANSPORT-PROPERTIES OF COLLOIDAL PARTICLES. *Journal of the Chemical Society-Faraday Transactions* **1990**, 86, (16), 2859-2870.
141. Glinka, C. J.; Barker, J. G.; Hammouda, B.; Krueger, S.; Moyer, J. J.; Orts, W. J., The 30 m small-angle neutron scattering instruments at the National Institute of Standards and Technology. *Journal of Applied Crystallography* **1998**, 31, 430-445.
142. Seebergh, J. E.; Berg, J. C., EVIDENCE OF A HAIRY LAYER AT THE SURFACE OF POLYSTYRENE LATEX-PARTICLES. *Colloids and Surfaces a-Physicochemical and Engineering Aspects* **1995**, 100, 139-153.
143. Yang, F.; Niu, Q.; Lan, Q.; Sun, D. J., Effect of dispersion pH on the formation and stability of Pickering emulsions stabilized by layered double hydroxides particles. *Journal of Colloid and Interface Science* **2007**, 306, (2), 285-295.
144. Derjaguin, B. V., Landau, L., *Acta Physico-Chimica* **1941**, 14, 633.
145. Verwey, E. J. W., Overbeek, J.T.G., Theory of the Stability of Lyophobic Colloids. In Elsevier: Amsterdam, 1948.

146. Hamaker, H. C., The London - Van Der Waals attraction between spherical particles. *Physica* **1937**, 4, 1058-1072.
147. Hartley, P. G.; Grieser, F.; Mulvaney, P.; Stevens, G. W., Surface forces and deformation at the oil-water interface probed using AFM force measurement. *Langmuir* **1999**, 15, (21), 7282-7289.
148. Sunkel, J. M.; Berg, J. C., The stability behavior of sol-emulsion systems. *Journal of Colloid and Interface Science* **1996**, 179, (2), 618-624.
149. Gouy, L. G., *Journal of Physics* **1910**, 4, (9).
150. Chapman, D. L., A Contribution to the Theory of Electrocapillarity. *Philosophical Magazine* **1913**, 25, (148), 475-481.
151. Freiburger, N.; Glatter, O., Small-angle scattering from hexagonal liquid crystals. *Journal of Physical Chemistry B* **2006**, 110, (30), 14719-14727.
152. Tam, J. M.; Tam, J. O.; Murthy, A.; Ingram, D. R.; Ma, L. L.; Travis, K.; Johnston, K. P.; Sokolov, K. V., Controlled Assembly of Biodegradable Plasmonic Nanoclusters for Near-Infrared Imaging and Therapeutic Applications. *Acs Nano* **2010**, 4, (4), 2178-2184.
153. Loo, C.; Lowery, A.; Halas, N. J.; West, J.; Drezek, R., Immunotargeted nanoshells for integrated cancer imaging and therapy. *Nano Letters* **2005**, 5, (4), 709-711.
154. Lal, S.; Clare, S. E.; Halas, N. J., Nanoshell-Enabled Photothermal Cancer Therapy: Impending Clinical Impact. *Accounts of Chemical Research* **2008**, 41, (12), 1842-1851.
155. Hirsch, L. R.; Gobin, A. M.; Lowery, A. R.; Tam, F.; Drezek, R. A.; Halas, N. J.; West, J. L., Metal nanoshells. *Annals of Biomedical Engineering* **2006**, 34, (1), 15-22.
156. Wang, Y. W.; Xie, X. Y.; Wang, X. D.; Ku, G.; Gill, K. L.; O'Neal, D. P.; Stoica, G.; Wang, L. V., Photoacoustic tomography of a nanoshell contrast agent in the in vivo rat brain. *Nano Letters* **2004**, 4, (9), 1689-1692.
157. Jain, P. K.; Lee, K. S.; El-Sayed, I. H.; El-Sayed, M. A., Calculated absorption and scattering properties of gold nanoparticles of different size, shape, and composition: Applications in biological imaging and biomedicine. *Journal of Physical Chemistry B* **2006**, 110, (14), 7238-7248.
158. Lewinski, N.; Colvin, V.; Drezek, R., Cytotoxicity of nanoparticles. *Small* **2008**, 4, (1), 26-49.
159. Yoon, S. J.; Mallidi, S.; Tam, J. M.; Tam, J. O.; Murthy, A.; Johnston, K. P.; Sokolov, K. V.; Emelianov, S. Y., Utility of biodegradable plasmonic nanoclusters in photoacoustic imaging. *Optics Letters* **2010**, 35, (22), 3751-3753.
160. Vasir, J. K.; Labhasetwar, V., Biodegradable nanoparticles for cytosolic delivery of therapeutics. *Advanced Drug Delivery Reviews* **2007**, 59, (8), 718-728.
161. Zhou, J.; Wang, L. J.; Qiao, X. Y.; Binks, B. P.; Sun, K., Pickering emulsions stabilized by surface-modified Fe₃O₄ nanoparticles. *Journal of Colloid and Interface Science* **2012**, 367, 213-224.
162. Du, K.; Glogowski, E.; Emrick, T.; Russell, T. P.; Dinsmore, A. D., Adsorption Energy of Nano- and Microparticles at Liquid-Liquid Interfaces. *Langmuir* **2010**, 26, (15), 12518-12522.

163. Almusallam, A. S., Simulation of block copolymer stabilized nanoparticles in a two-solvent system. *Physical Chemistry Chemical Physics* **2008**, 10, (21), 3099-3107.
164. Saleh, N.; Phenrat, T.; Sirk, K.; Dufour, B.; Ok, J.; Sarbu, T.; Matyjaszewski, K.; Tilton, R. D.; Lowry, G. V., Adsorbed triblock copolymers deliver reactive iron nanoparticles to the oil/water interface. *Nano Letters* **2005**, 5, (12), 2489-2494.
165. Saigal, T.; Dong, H. C.; Matyjaszewski, K.; Tilton, R. D., Pickering Emulsions Stabilized by Nanoparticles with Thermally Responsive Grafted Polymer Brushes. *Langmuir* **2010**, 26, (19), 15200-15209.
166. Fall, S.; Pattier, B.; Benyayia, L.; Gibaud, A., Binary Phase Diagram of Water/Brij58 Studied by SAXS. In *Acta Physica Polonica A*, 2012; Vol. 121, pp 388-396.
167. Mie, G., Articles on the optical characteristics of turbid tubes, especially colloidal metal solutions. *Annalen Der Physik* **1908**, 25, (3), 377-445.
168. Hutter, E.; Fendler, J. H., Exploitation of localized surface plasmon resonance. *Advanced Materials* **2004**, 16, (19), 1685-1706.
169. Rechberger, W.; Hohenau, A.; Leitner, A.; Krenn, J. R.; Lamprecht, B.; Aussenegg, F. R., Optical properties of two interacting gold nanoparticles. *Optics Communications* **2003**, 220, (1-3), 137-141.
170. Lamprecht, B.; Schider, G.; Lechner, R. T.; Ditlbacher, H.; Krenn, J. R.; Leitner, A.; Aussenegg, F. R., Metal nanoparticle gratings: Influence of dipolar particle interaction on the plasmon resonance. *Physical Review Letters* **2000**, 84, (20), 4721-4724.
171. Wang, Y. Z.; Fan, D. Q.; He, J. P.; Yang, Y. L., Silica nanoparticle covered with mixed polymer brushes as Janus particles at water/oil interface. *Colloid and Polymer Science* **2011**, 289, (17-18), 1885-1894.
172. Price, L. C., AQUEOUS SOLUBILITY OF PETROLEUM AS APPLIED TO ITS ORIGIN AND PRIMARY MIGRATION. *Aapg Bulletin-American Association of Petroleum Geologists* **1976**, 60, (2), 213-244.
173. Tsai, W. T., Environmental hazards and health risk of common liquid perfluoro-n-alkanes, potent greenhouse gases. *Environment International* **2009**, 35, (2), 418-424.
174. Richards, J. J.; Weigandt, K. M.; Pozzo, D. C., Aqueous dispersions of colloidal poly(3-hexylthiophene) gel particles with high internal porosity. *Journal of Colloid and Interface Science* **2011**, 364, (2), 341-350.
175. Wu, J. L.; Chen, F. C.; Hsiao, Y. S.; Chien, F. C.; Chen, P. L.; Kuo, C. H.; Huang, M. H.; Hsu, C. S., Surface Plasmonic Effects of Metallic Nanoparticles on the Performance of Polymer Bulk Heterojunction Solar Cells. *Acs Nano* **2011**, 5, (2), 959-967.

Appendix A: Particle Synthesis and Functionalization

A.1 Materials

Gold tetrachloride trihydrate, silver nitrate, sodium citrate dibasic, sodium borohydride, tetraoctylammonium bromide, dithiothreitol, toluene, butane-thiol, octane-thiol, dodecane-thiol and potassium hydroxide are purchased from Sigma Aldrich (St. Louis, MO) and used as received. Thiol-terminated Poly(ethylene glycol) methyl ether (5 and 10 kDa) is obtained from Polymer Source (Dorval, Quebec Canada) and stored in a 4 °C refrigerator. Ultrapure deionized water is passed through a Milli-Q reagent water system to a purity of 18 M Ω ·cm resistivity.

A.2 Glassware Cleaning

All glassware involved in the synthesis of colloidal gold particles must be scrupulously clean and well rinsed. Any contamination acts as unwanted nucleation sites for particles. The standard cleaning procedure includes soaking glassware in a base bath overnight followed by a rinse with copious amounts of deionized water and drying in an oven. The base bath is mixed in a 1 liter volumetric flask by first dissolving 120 g potassium hydroxide (KOH) in 120 mL water. After all of the KOH is dissolved, 200 proof ethanol is slowly added to make a 1 L solution. The solution can be reused until it turns a dark brown color.

A.3 12nm Gold Particle Synthesis

Colloidal gold with 12 nm diameter particles are prepared by the citrate reduction method with a protocol that is described by Frens.⁸² This protocol produces relatively monodisperse gold particles at a concentration of 0.025 wt% in an aqueous buffer. The most efficient use of the $\text{HAuCl}_4 \cdot 3\text{H}_2\text{O}$ is to add 2.539 mL deionized water to a 1 g bottle in order to make a 1 M HAuCl_4 stock solution. The stock solution is used to make 500 mL of a 1 mM HAuCl_4 in water solution in a 1 L Erlenmeyer flask. The dry tare weight of the flask is noted for the final dispersion concentration calculation. The flask is covered with aluminum foil for the duration of the synthesis to prevent water evaporation. The solution is brought to a boil with vigorous stirring on a magnetic stirring hot plate. At one time, 50 mL of a 38.8 mM sodium citrate in water solution is added to the HAuCl_4 solution with vigorous stirring. Almost immediately, the yellow solution will turn clear as the citrate reduces the gold ions. The solution then turns dark blue as the gold forms long rods. The rods eventually fracture into individual particles which look deep red in color. Stirring and boiling is continued for 20 minutes after the color change to allow for Ostwald ripening. The solution is then removed from heat and kept stirring for 15 minutes. The final weight of the total dispersion in the Erlenmeyer flask is calculated. The weight of the gold is known from the initial amount of HAuCl_4 that is added to the original solution. A final weight concentration of gold nanoparticles is calculated by dividing the initial mass of gold by the final weight of the total dispersion. The total volume fraction of particles can be calculated from the densities of gold (19.3 g/mL) and water (1 g/mL). The final particle dispersion must be stored in a brown jar or a jar covered with aluminum foil to prevent degradation of the particles from exposure to light.

A.4 6 nm Gold Particle Synthesis

The Brust method is used to synthesize 6 nm colloidal gold in toluene.¹³⁸ A 10 mL aqueous solution of 0.025 M HAuCl_4 is vigorously mixed with 25 mL of a 0.05 M tetraoctylammonium bromide (TOAB) solution in a separation funnel. The TOAB phase-transfers the gold chloride ions into toluene. The gold chloride is then reduced in the toluene by adding 10 mL of aqueous 0.4 M sodium borohydride drop wise. After 6 hours of stirring the organic phase is again recovered with a separation funnel and the reaction is complete. The particles can be functionalized and redispersed in water or used directly in the organic phase. One major benefit to the Brust method is the ability to make extremely monodisperse particles in concentrated dispersions.

A.5 40nm Gold Particle Synthesis

Large 40 nm gold nanoparticles used to make the self-assembled raspberry particles are synthesized using the modified Frens method.⁸² Here, we use the same procedure that was used for synthesizing 12 nm gold. However, altering the ratio of citrate to gold chloride ions controls the size of the particle. To synthesize particles with a radius of 20 nm, 100 mL of a 0.3 mM HAuCl_4 solution in water is brought to a boil with rigorous stirring and the flask is covered with foil to prevent evaporation. Subsequently, 10 mL of a 1.8 mM sodium citrate solution is added so that the ratio of citrate to gold chloride ions is 0.6. The resulting dispersion appears turbid and brown in color. The particles are relatively monodisperse, but most of the particles are non-spherical.

A.6 18nm Silver Particle Synthesis

Colloidal silver particles in aqueous dispersion are synthesized using a modified Turkevich method.¹⁵ This protocol produces silver nanoparticles that are 18 nm in diameter with a fair amount of polydispersity. First, 100 mL of a 1 mM silver nitrate (AgNO_3) solution in water is mixed in a 125 mL Erlenmeyer flask. The flask is heated to 90 °C in an oil bath with vigorous stirring for more even heating. Once the silver nitrate solution reaches the desired temperature, 0.2 mL of a 0.35 M sodium citrate solution is added, followed by 0.1 mL of a 0.13 M sodium borohydride solution. This reduces the silver ions to silver atoms that nucleate and form particles. However, only a fraction of silver ions are reduced to metal, even when using an excess of reducing reagent. Due to the presence of silver ions in the medium, new nuclei will still be formed while the initially formed particles continue to grow. To prevent this from happening, 0.378 mL of 0.148 M aqueous ammonia is added 15 seconds after the addition of sodium citrate and sodium borohydride to sequester any remaining silver ions that might act as nucleation sites.¹⁴ Continue heating and stirring for 10 minutes until the reaction is finished. The Turkevich synthesis method alone produces extremely polydisperse particle sizes because new nucleation sites continue to form throughout the reaction and the difference in growth time causes a distribution of particle sizes. By adding ammonia, only the nucleation sites created at the beginning of the reaction continue to grow, so much more monodisperse particles are the result.

A.7 Particle functionalization

The nanoparticles are functionalized directly utilizing thiol-gold covalent bonding chemistry without the need for any intermediate treatment or purification.^{34, 83-85} A 150 mM dithiothreitol (DTT) in water stock solution is freshly made and set aside. A 5 mM PEG-thiol solution is made in freshly purified water with equimolar DTT added from the stock solution in order to reactivate the PEG-thiol. This solution must sit at least 12 hours to full dissolve and allow enough time for the DTT to cleave disulfide bonds. It is best to use the PEG solution within one week of preparation. The appropriate volume, V , of 5 mM PEG solution is added directly to the gold dispersion according to Equation A.1. Here Φ is the desired PEG loading in PEG chains/nm² Au, N_A is Avogadro's number, R is the particle radius, X is the mass of the gold dispersion to be functionalized and ρ_{Au} is the density of gold.

$$V_{5mMPEG} = \frac{\left(\frac{\Phi}{N_A}\right)\left(\frac{4\pi R^2}{4/3\pi R^3}\right)\left(\frac{X_{Dispersion} \text{ 0.02wt\% Au}}{\rho_{Au}}\right)}{5mMPEG} \quad (\text{A.1})$$

A.8 References

1. Frens, G., CONTROLLED NUCLEATION FOR REGULATION OF PARTICLE-SIZE IN MONODISPERSE GOLD SUSPENSIONS. *Nature-Physical Science* **1973**, 241, (105), 20-22.
2. Brust, M.; Walker, M.; Bethell, D.; Schiffrin, D. J.; Whyman, R., SYNTHESIS OF THIOL-DERIVATIZED GOLD NANOPARTICLES IN A 2-PHASE LIQUID-LIQUID SYSTEM. *Journal of the Chemical Society-Chemical Communications* **1994**, (7), 801-802.
3. Turkevich, J.; Stevenson, P. C.; Hillier, J., A STUDY OF THE NUCLEATION AND GROWTH PROCESSES IN THE SYNTHESIS OF COLLOIDAL GOLD. *Discussions of the Faraday Society* **1951**, (11), 55-&.
4. Gorup, L. F.; Longo, E.; Leite, E. R.; Camargo, E. R., Moderating effect of ammonia on particle growth and stability of quasi-monodisperse silver nanoparticles

- synthesized by the Turkevich method. *Journal of Colloid and Interface Science* **2011**, 360, (2), 355-358.
5. Love, J. C.; Estroff, L. A.; Kriebel, J. K.; Nuzzo, R. G.; Whitesides, G. M., Self-assembled monolayers of thiolates on metals as a form of nanotechnology. *Chemical Reviews* **2005**, 105, (4), 1103-1169.
 6. Shan, J.; Tenhu, H., Recent advances in polymer protected gold nanoparticles: synthesis, properties and applications. *Chemical Communications* **2007**, (44), 4580-4598.
 7. Nuzzo, R. G.; Allara, D. L., ADSORPTION OF BIFUNCTIONAL ORGANIC DISULFIDES ON GOLD SURFACES. *Journal of the American Chemical Society* **1983**, 105, (13), 4481-4483.
 8. Porter, M. D.; Bright, T. B.; Allara, D. L.; Chidsey, C. E. D., SPONTANEOUSLY ORGANIZED MOLECULAR ASSEMBLIES .4. STRUCTURAL CHARACTERIZATION OF NORMAL-ALKYL THIOL MONOLAYERS ON GOLD BY OPTICAL ELLIPSOMETRY, INFRARED-SPECTROSCOPY, AND ELECTROCHEMISTRY. *Journal of the American Chemical Society* **1987**, 109, (12), 3559-3568.

Appendix B: Photoacoustic and Ultrasound Imaging Experimental Set-Up

Vaporizable emulsions are evaluated for use as contrast agents in ultrasound and photoacoustic imaging. These experiments are performed in collaboration with Matt O'Donnell's group in UW Department of Bioengineering and Tom Matula from UW Center for Industrial and Medical Ultrasound.

The perfluorohexane emulsion is generated in the Pozzo lab and spun on a roller mixer for at least 24 hours to give the particles ample time to reach the oil-water interface. The samples are then loaded into a polytetrafluoroethylene (Teflon) optically transparent tube (ID=0.065±0.001 inch, wall thickness=0.0015±0.001 inch), which is immersed in a water tank. The radiation source is a variable wavelength pulsed laser operating at $\lambda=810$ nm, 4.5 mJ and 20 Hz pulses, resulting in an average power output of 90 mW spread over an area that is 3-5 mm in diameter. A transducer simultaneously acquires the photoacoustic signal and ultrasound pulse-echo imaging. Figure B.1 is a picture of the experimental set-up.

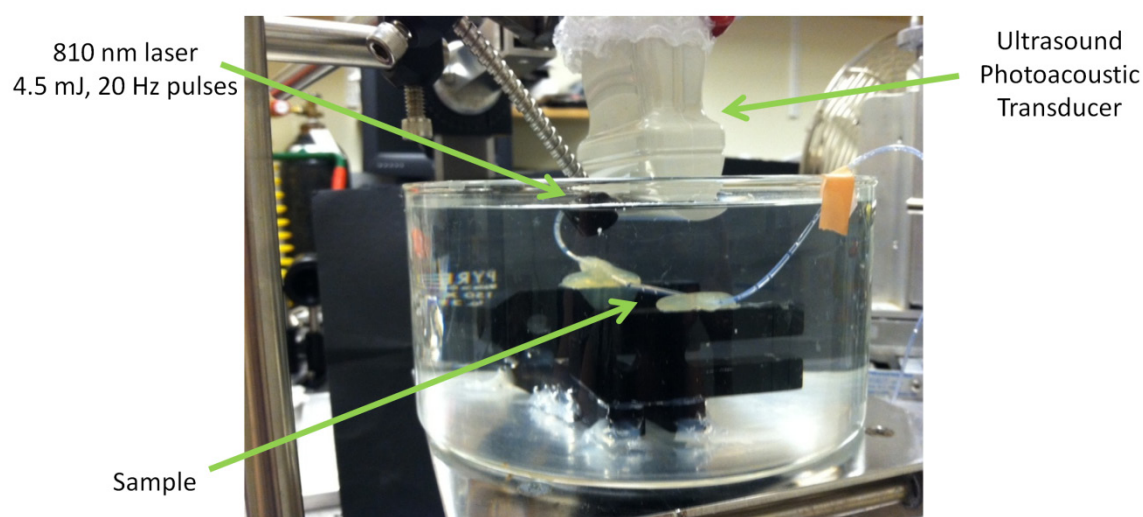


Figure B.1. Photoacoustic and ultrasound experimental set-up.

In photoacoustic imaging, near infrared (NIR) laser pulses are delivered to the gold nanostructure. The gold particles absorb this radiation and convert it into heat, resulting in thermal expansion of the material.¹⁷⁶ This causes the generation of ultrasonic acoustic waves that are measured by the transducer. For this reason, materials with the highest NIR absorbance will be most effective photoacoustic contrast agents. A schematic of this process is given in Figure B.2.

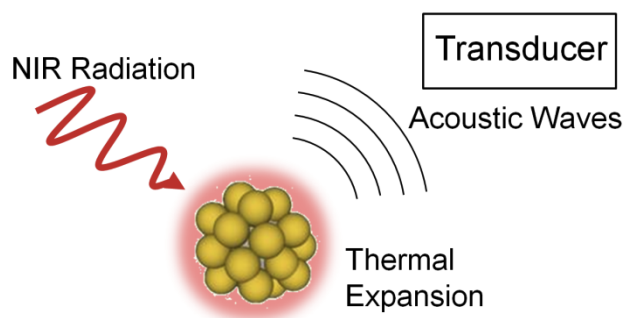


Figure B.2. Schematic of photoacoustic measurements.

In ultrasound imaging, the transducer generates an acoustic wave at the desired frequency (2-20 MHz). The sound wave is reflected when it contacts density differences in the sample. The wave that is reflected back, or the echo wave, is measured by the transducer.¹⁷⁷ The intensity of the echo wave (I_s) is a function of the incident intensity (I_i), the scattering cross section (σ) and the distance between the transducer and the scattering site (R) as shown in Equation B.1.

$$I_s = \frac{I_i \sigma}{4\pi R^2} \quad (\text{B.1})$$

The scattering cross section is dependent on the relative adiabatic compressibilities (κ) and densities (ρ) of the scatterer and surrounding medium.¹⁷⁸ Equation B.2 is the full equation for the scattering cross section where N is the concentration per unit volume, λ is the wavelength and r is the radius of the scatterer.

$$\sigma = \left[N \frac{4\pi}{9} \left(\frac{2\pi}{\lambda} \right)^4 r^6 \right] \left[\left(\frac{\kappa_s - \kappa}{\kappa} \right)^2 + \frac{1}{3} \left(\frac{3(\rho_s - \rho)}{2\rho_s + \rho} \right)^2 \right] \quad (\text{B.2})$$

Comparing the relative values of the second bracketed term, the scattering cross section of gases is much larger than solids and liquids ($\sigma_{\text{gas}} \sim 10^{14}$, $\sigma_{\text{solid}} \sim 1.75$ and $\sigma_{\text{liquid}} \sim 0$). This suggests the bubbles that are generated from our emulsions will have a large increase in ultrasound signal intensity. Furthermore, the scattering cross section is proportional to r^6 . Therefore, the increase in emulsion droplet size (100 nm to 1 μm) due to the transition from liquid to vapor further enhances the signal by 10^6 . Thus, large ultrasound signals are observed when emulsion droplets have been vaporized. A schematic of the ultrasound measurements is shown in Figure B.2.

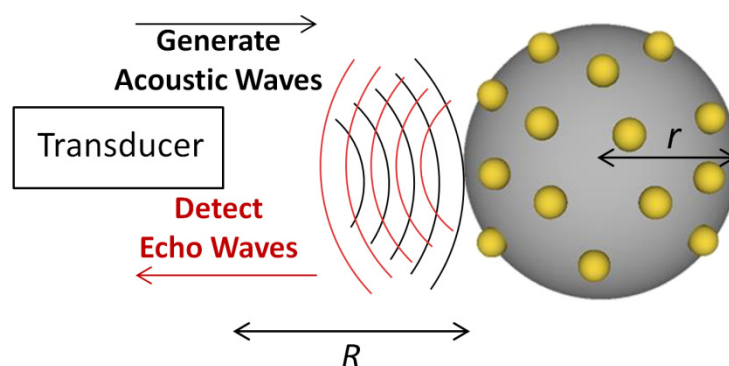


Figure B.2. Schematic of ultrasound measurements.

References

1. Xu, M. H.; Wang, L. H. V., Photoacoustic imaging in biomedicine. *Review of Scientific Instruments* **2006**, 77, (4), 22.
2. Goldberg, B. B.; Liu, J. B.; Forsberg, F., ULTRASOUND CONTRAST AGENTS - A REVIEW. *Ultrasound in Medicine and Biology* **1994**, 20, (4), 319-333.
3. Ophir, J.; Parker, K. J., CONTRAST AGENTS IN DIAGNOSTIC ULTRASOUND. *Ultrasound in Medicine and Biology* **1989**, 15, (4), 319-333.

Curriculum Vitae
Kjersta L. Larson-Smith, Ph.D.

SUMMARY OF QUALIFICATIONS

- More than 7 years research experience in industry and academic settings.
- Proven inventor with 1 US patent awarded and 4 other patent applications under review.
- Experienced in mentoring peers and undergraduate students.
- Effective in project planning, testing and data interpretation.
- Skilled written and verbal communicator; able to explain complex concepts at many levels.

EDUCATION

University of Washington , Ph.D., Chemical Engineering Thesis Title: Self-Assembly of Nanoparticles in Dispersion and at Fluid-Fluid Interfaces Advisor: Prof. Danilo C Pozzo	June 2012
University of Washington , M.S., Chemical Engineering	June 2010
Columbia University , B.S., Chemical Engineering, <i>magna cum laude</i>	May 2006
Pacific Lutheran University , B.A., Chemistry, <i>cum laude</i>	May 2006

Awards/Honors

Ford Motor Company Graduate Fellowship (Sept. 2010-Sept. 2011)
 McCarthy Outstanding Teaching Assistant (2010-2011)
 University of Washington Egvatz Fellowship (Sept. 2008-Sept. 2009)
 PLU Chemistry Department Honors at Graduation (May 2006)
 PLU Ramstad Chemistry Scholar (Sept. 2002-May 2003)
 PLU Presidential Scholar (Sept. 2001-May 2004)

RELEVANT EXPERIENCE

University of Washington, Department of Chemical Engineering , Seattle, WA <i>Graduate Research Assistant</i>	Sept. 2008-Present
<ul style="list-style-type: none"> • Studied the stability and interfacial structure of nanoparticle stabilized emulsions. • Created a small-angle scattering model for Pickering emulsions and raspberry particles. • Developed synthesis technique for amphiphilic self-assembling nanoparticles. • Mentored 8 undergraduates on independent research projects. 	

Teaching Assistant March 2010-Present

- Taught weekly recitation sessions for a class of 60 students.
- Designed and led laboratory experiments.
- Assisted in creating and grading class coursework and exams.

The Boeing Company, Boeing Research and Technology, Seattle, WA

Chemical Engineer June 2006-Sept. 2008

- Designed durable, transparent hard coatings with one awarded patent and four patent applications under review.
- Acted as transparency coatings focal for Boeing Research and Technology.
- Wrote company material specification document for transparent coatings.
- Worked with suppliers to transfer technology and qualify products.

Student Engineer Summer 2005

- Developed a test plan and evaluated advanced window coatings to determine durability, environmental resistance and optical properties.
- Created new sol-gel formulations containing oxide nanoparticles to increase abrasion resistance in coatings.

Columbia University, Department of Chemical Engineering, New York, NY

Undergraduate Research Assistant Sept. 2004-May 2006

- Studied the absorption of proteins on bio-incompatible surfaces. Constructed a Quartz Crystal Microbalance to determine total protein adsorption and how protein bonds to surfaces.

Pacific Lutheran University, Department of Chemistry, Tacoma, WA

Undergraduate Research Assistant Summer 2003 and 2004

- Analyzed use of various copolymers to compatibilize a blend of polystyrene and polybutadiene. Studied the kinetics of phase separation using wide angle light scattering and thermodynamics with cloud point instrumentation.
- Designed drug delivery capsules using molecular modeling to determine the most energetically favorable conformations.

Pacific Lutheran University, Academic Assistance Center, Tacoma, WA*Math and Physics Tutor*

Sept. 2003-May 2004

- Worked with students as a College Reading & Learning Association certified tutor.
- Facilitated weekly class review sessions.
- Conducted seminars on effective study and test taking skills.

LEADERSHIP POSITIONS

University Representative , AIChE Student Chapter	Sept. 2005-May 2006
Peer Mentor , Columbia Transfer Alliance	Sept. 2005-May 2006
President , American Chemical Society Student Chapter	Sept. 2003-May 2004
President , Resident Hall Council	Sept. 2002-May 2003

TECHNICAL SKILLS

Expert - Small-Angle X-ray Scattering, Small-Angle Neutron Scattering, Dynamic Light Scattering, Confocal Microscopy, Thermogravimetric Analysis

Proficient - Transmission Electron Microscopy, NanoIndentation, Static Light Scattering, Raman Spectroscopy, IR Spectroscopy, Rheology, Cloud Point Measurements

Familiar - Gas Chromatography-Mass Spectrometry, Inductively Coupled Plasma, Quartz Crystal Microbalance, Nuclear Magnetic Resonance Spectroscopy, Atomic Force Microscopy

PUBLICATIONS

-
1. **Larson-Smith, KL**; Pozzo, DC; "Competitive Adsorption of Thiolated Polyethylene Glycol and Alkane-thiols on Gold Nanoparticles." Submitted.
 2. **Larson-Smith, KL**; Pozzo, DC; "Pickering Emulsions Stabilized by Nanoparticle Surfactants." *Langmuir*. Submitted.
 3. **Larson-Smith, KL**; Jackson, A; Pozzo, DC; "SANS and SAXS analysis of charged nanoparticle adsorption at oil-water interfaces." *Langmuir*. **2012**, 28 (5), 2493-2501.
 4. **Larson-Smith, KL**; Pozzo, DC; "Scalable synthesis of self-assembling nanoparticle clusters based on controlled steric interactions." *Soft Matter*. **2011**, 7 (10), 5339-5347.
 5. **Larson-Smith, KL**; Jackson, A; Pozzo, DC; "Small angle scattering model for Pickering emulsions and raspberry particles." *Journal of Colloid and Interface Science*. **2010**, 343, (1), 36-41.
 6. Kamer, A; **Larson-Smith, KL**.; Pingree, LSC; Dauskardt, RH; "Adhesion and degradation of hard coatings on poly (methyl methacrylate) substrates." *Thin Solid Films*. **2010**, 519, (6), 1907-1913.

PATENTS & PATENT APPLICATIONS

1. **Larson, KL**; Pare, SM; Sundaram, VS; “Barrier coatings for polymeric substrates.” 2011-02-01: US 7878054. AWARDED
2. **Larson-Smith, KL**; Sundaram, VS; Sirkis, MR; “Wear-resistant coating for polymeric transparencies.” 2009-12-17: US 20090311539. Under Review.
3. **Larson-Smith, KL**; Blohowiak, KY; Seebergh, JE; Sirkis, MR; Sundaram, VS; “Hybrid coatings and associated methods of application.” 2010-08-05: US 20100196621. Under Review.
4. **Larson-Smith, KL**; Sundaram, VS; Bowen, DA; Pare, SM; Pingree, LSC; “Durable transparent intelligent coatings for polymeric transparencies.” 2010-09-23: US 20100239742. Under Review.
5. Bowen, DA; **Larson-Smith, KL**; Sundaram, VS; “Durable UV blocking transparent coating.” 2010-09-23: US 20100239870. Under Review.

PRESENTATIONS

1. **Larson-Smith, KL**, Pozzo, DC; “SANS and SAXS Analysis of Charged Nanoparticle Adsorption at Oil-Water Interfaces” UW Chemical Engineering Graduate Student Symposium, Sept. 2011, Poster.
2. **Larson-Smith, KL**, Pozzo, DC; “Scalable Synthesis of Self-Assembling Amphiphilic Nanoparticle Clusters Based on Steric Surface Stabilization” NanoTechnology at the UW, Sept. 2011, Poster.
3. **Larson-Smith, KL**, Pozzo, DC; “Scalable Synthesis of Self-Assembling Amphiphilic Nanoparticle Clusters Based on Steric Surface Stabilization” AIChE Annual Meeting, Nov. 2010. Presentation.
4. **Larson-Smith, KL**, Pozzo, DC; “Scalable Synthesis of Self-Assembling Amphiphilic Nanoparticle Clusters Based on Steric Surface Stabilization” UW Chemical Engineering Graduate Student Symposium, Sept. 2010. Presentation.
5. **Larson-Smith, KL**; Pozzo, DC; “Pickering Emulsion Stability and Interfacial Structure” Northwest Regional Meeting of the American Chemical Society, June 2009, Presentation.
6. **Larson-Smith, KL**; Pozzo, DC; “Pickering Emulsion Stability and Interfacial Structure” International Conference on Neutron Scattering, May 2009, Poster.
7. **Larson, KL**; Pare, SM; Sirkis, MR; Sundaram, VS; ASTM F07 Aerospace and Aircraft – Transparencies Meeting. Nov. 2007, Presentation.
8. **Larson, KL**; Sundaram, VS; “Plasma-based Chemical Vapor Deposition Based Transparent Coatings for Aircraft Passenger Windows” Material Science & Technology 2007 Conference, Sept. 2007, Presentation